UNIVERSIDAD DE CHILE
FACULTAD DE CIENCIAS FÍSICAS Y MATEMÁTICAS
DEPARTAMENTO DE ASTRONOMÍA

# RADIATIVE TRANSFER IN PROTOPLANETARY DISCS

TESIS PARA OPTAR AL GRADO DE MAGÍSTER EN CIENCIAS, MENCIÓN
ASTRONOMÍA

RAFAEL JOSÉ MARTINEZ BRUNNER

PROFESOR GUÍA:
Simón Casassus Montero

MIEMBROS DE LA COMISIÓN:
Cesar Fuentes González
Diego Mardones Pérez
Philipp Weber

SANTIAGO DE CHILE
2022

# TRANSFERENCIA RADIATIVA EN DISCOS PROTOPLANETARIOS

Gracias a los importantes avances tecnológicos, el estudio de los discos protoplanetarios se ha desarrollado rápidamente en las dos últimas décadas. Con instrumentos cada vez mejores, observatorios como ALMA y el VLT han revelado nuevos detalles sobre estas fuentes en alta resolución y a un ritmo sin precedentes. Junto con estas nuevas posibilidades de obtención de imágenes, se han desarrollado o perfeccionado códigos numéricos de modelización que permiten realizar estudios teóricos de vanguardia sobre la física de los discos. Combinando ambos campos, podemos crear elaborados modelos paramétricos y reproducir imágenes de alta resolución en múltiples longitudes de onda para obtener un modelo físico como contraparte de los datos reales. Este enfoque adquiere especial relevancia cuando se estudian los complejos fenómenos de transferencia radiativa en geometrías muy complejas, como los discos con subestructuras.

Los dos proyectos desarrollados a lo largo de esta tesis tenían como objetivo proporcionar modelos 3D precisos que pudieran reproducir múltiples observaciones disponibles de dos notables discos protoplanetarios, cada uno de ellos con características únicas y curiosas. Para crear los modelos, utilizamos el código de transferencia radiativa RADMC3D y estudiamos cómo las estrellas que componen cada sistema calientan el polvo de su entorno y cómo éste irradia después a diferentes frecuencias. Si un modelo pudiera replicar los datos, tendríamos un esquema detallado de cada disco, lo que nos permitiría realizar una investigación más profunda.

Las dos fuentes seleccionadas fueron V4046 Sagtarrius e ISO-OPh 2, cada una de las cuales estudiamos por separado pero utilizando procesos de modelización muy similares. En cuanto al disco circumbinario de V4046Sgr, hemos sido capaces de recrear íntegramente los datos en múltiples longitudes de onda, incluyendo una observación de radio de ALMA de alta resolución, una imagen de luz polarizada captada con el instrumento SHERE/IRIDIS, junto con datos fotométricos y espectrales de los archivos. Encontramos que el disco tiene una estructura interna complicada con múltiples anillos y poblaciones de polvo. Los resultados finales de este proyecto se publicaron en Martinez-Brunner et al. (2022). En segundo lugar, para el disco circunestelar alrededor de la estrella primaria del sistema binario ISO-OPh 2, propusimos una explicación audaz para su estructura de doble anillo no axisimétrico, única en su género, observada con ALMA. Examinamos la posibilidad de que fuera el resultado de efectos ambientales, es decir, por una fuente de radiación externa, HD 147889, un sistema binario gigante cercano y el mayor emisor de rayos UV en la vecindad. Este proyecto mostró algunos resultados prometedores, ya que pudimos acercarnos a imitar la característica de radio observable con nuestros modelos. Estos resultados preliminares apoyan firmemente nuestra hipótesis.

# RADIATIVE TRANSFER IN PROTOPLANETARY DISCS

Thanks to significant technological advancements, protoplanetary disc studies have been under rapid development over the last two decades. With their ever-improving instruments, observatories like ALMA and the VLT have revealed new details about these sources at high-resolution and at an unprecedented pace. Along with these new imaging capabilities, new modelling numerical codes have been developed or enhanced, allowing state-of-the-art theoretical studies of disc physics. Combining both flanks, we can create elaborated parametric models and reproduce multi-wavelength high-resolution images to get a physical model as a counterpart of actual data. This approach becomes especially relevant when studying the complex phenomena of radiative transfer in intricate geometries, such as substructured discs.

The two projects developed throughout this thesis aimed to provide accurate 3D models that could reproduce multiple available observations of two remarkable protoplanetary discs, each exhibiting unique and puzzling features. To create the models, we used the radiative transfer code RADMC3D and studied how the stars that compose each system heat the surrounding dust and how it radiates at different frequencies. If a model could replicate the data, we would have a detailed schematic of each disc, enabling us to conduct more in-depth research.

The two selected sources were V4046 Sagittarius and ISO-Oph 2, each of which we studied separately but using very similar modelling processes. First, we were capable of completely recreating the multi-wavelength data of the circumbinary disc of V4046Sgr, including a high-resolution ALMA radio observation, a polarised light image captured with the SPHERE/IRDIS instrument, together with photometry and spectral data from the archives. We found that the disc has a complicated internal structure with multiple rings and dust populations. The final results of this project were published in Martinez-Brunner et al. (2022). Secondly, for the circumstellar disc around the primary star of the binary system ISO-OPh 2, we proposed a bold explication for its one-of-a-kind non-axisymmetric double-ring structure observable with ALMA. We examined the possibility of it being the result of environmental effects, namely by an external radiation source, HD 147889, a close giant binary system and the highest UV emitters in the vicinity. This project showed some promising results, as we were able to get close to mimicking the observable radio feature with our models. These preliminary results strongly support our hypothesis.

*Y equivocarse es bonito,*
*Los errore' son placere'*

**Benito Antonio Martínez Ocasio**

# Acknowledgements

# Table of Content

# Index of Tables

# Index of Illustrations

# Capítulo 1

# Introduction

It has been said that astronomy studies time as it flows. As the light takes so long to reach us from different points of the universe, we can literally observe the passing of time. This thought can be applied across all fields in astronomy, but it is undoubtedly even more meaningful thinking like so when we use it to study the origin of our home planet. Looking at star-forming regions, where we can find thousands of young stars, we can travel back in time to the moment when no planets were orbiting the Sun, some four billion years ago, and study the Solar system as it was in the earliest stages. To understand what was happening then, we will have to study the relationship between our young Sun and its chaotic surroundings.

After the collapse of a dense core in a massive molecular cloud of dust and gas, our Sun was born, but not alone. As this core was not at rest but had some rotation due to turbulent motions in the parental cloud, the conservation of angular momentum plays an important role. The material rotates, and some of it will do it so fast that it never reaches the star and ends up in orbit around it. This leftover will collapse into a disc, forming a circumstellar disc. The system will continue to evolve and disperse much of the surrounding cloud. However, the denser disc will remain orbiting long after the cloud has dispersed, creating what we define as a **protoplanetary disc**, or PPD for short (Fig. 1.1).

When we look at our Solar system, as it is right now, it is clear that gravity plays a leading role in what looks almost like a one-man show. Planets and asteroids orbit the Sun, and moons orbit the planets. However, this has not always been like that. During its formation, as the protoplanetary disc was made mainly of gas and tiny grains of dust, the radiation of the Sun was one of the protagonists. Photons ejected from the star's surface traverse the gas and dust-rich disc as they exchange enormous amounts of energy with everything they encounter. This complex association between light, gas and dust is often challenging to grasp, but it is crucial for unravelling what happens during planet formation. Fortunately, these radiative processes are well studied at the fundamental level, and now we can use what we know about them to help us figure out some underlying processes in planet formation.

This chapter will briefly overview the physics of Radiative Transfer and protoplanetary discs. I will then review how, using what we know about the first, to understand the latter better and how to solve this problem with simulation tools. I will then discuss, in some detail, different observational techniques commonly used in the field.
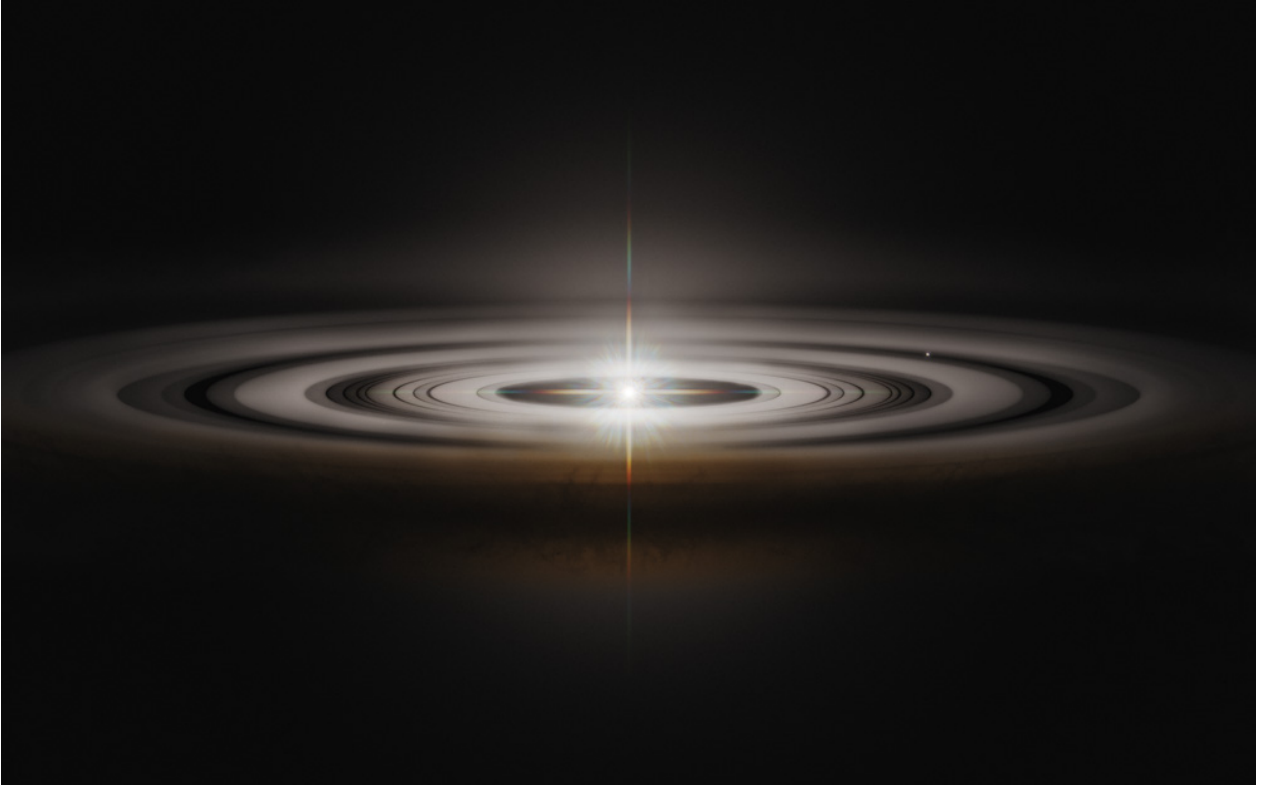
Figure 1.1: Artist's impression of a protoplanetary disc. It illustrates a bright central star with a large protoplanetary disc surrounding it, within which an orbiting planet is seated. ©Judy Schmidt, digital painting.

## 1.1. Fundamentals of Radiative Transfer

[1]To describe radiation is, in a sense, a detailed description of the energy flowing from one point to another as carried along by sets of light rays. Given a ray, we can imagine a region $dA$ normal to its direction and consider all rays that pass through it with directions within a solid angle $d\Omega$ of the given ray. Then, we can define the energy $dE$ that crosses an area $dA$ in time $dt$ and in frequency range $d\nu$ by the relation:

$$dE = I_\nu \, dA \, dt \, d\Omega \, d\nu \; , \tag{1.1}$$

where $I_\nu$ is the *specific intensity*. If we take any two points along a ray and use the fact that energy is conserved, we get that any ray, no matter its origin, as it travels across empty space, its intensity will remain constant too. This sentence might also be expressed as follows:

$$\frac{dI_\nu}{ds} = 0 \, , \tag{1.2}$$

where $ds$ is a differential element of length along the ray. This interpretation, however, is insufficient since, for instance, an evolving star is not surrounded by a vacuum, which means there will always be interactions between the light and the nearby material. Therefore, a ray's intensity will typically change as it travels through matter since energy may be given to

---

[1] This chapter is a brief review of the first chapter of the first chapter of Rybicki and Lightman (1979).

or taken away from it through emission or absorption. We can rewrite (1.2) to include these effects into a single equation that gives the variation of specific intensity along a ray.

$$\frac{dI_\nu}{ds} = -\alpha_\nu I_\nu + j_\nu \, . \tag{1.3}$$

The first term on the right side represents the loss of intensity in a beam, with the *absorption coefficient* $\alpha_\nu$ positive by convention for energy taken out. The second term refers to the intensity added to the beam due to spontaneous emission, with $j_\nu$ as the *emission coefficient.* Both coefficients depend on the properties of the medium. This equation is called *The Radiative Transfer Equation.*

The intensity in an emitting and absorbing medium can be solved using this equation. If $\alpha_\nu$ and $j_\nu$ are known, the intensity can be solved without much difficulty. However, it is useful to revisit the transfer equation and choose another variable, $\tau_\nu$, known as the *optical depth*, in place of $s$, as defined by

$$d\tau_\nu = \alpha_\nu ds \, , \tag{1.4}$$

where $\tau$ is measured along the path of a travelling ray. With the help of this new parameter, we can reconsider our medium in terms of optical depth value. When $\tau_\nu$, integrated along a typical path through the medium, satisfies $\tau_\nu > 1$, the medium is said to be *optically thick*, and when $\tau_\nu < 1$, the medium is said to be *optically thin.* Essentially, a medium is said to be optically thin at a frequency $\nu$ if it allows the majority of photons of frequency $\nu$ to pass through it without being absorbed. An optically thick medium, on the other hand, is one in which the photons of frequency $\nu$ cannot pass entirely through the medium without being absorbed.

Under this new conception, the transfer equation can now be written as

$$\frac{dI_\nu}{d\tau_\nu} = -I_\nu + S_\nu \, , \tag{1.5}$$

where the *Source function $S_\nu$* is defined as the ratio of the emission coefficient to the absorption coefficient:

$$S_\nu \equiv \frac{j_\nu}{\alpha_\nu}. \tag{1.6}$$

The source function is usually a more reliable physical quantity than the emission coefficient. Moreover, this optical depth scale makes understanding the radiation-related steps along a beam more intuitive. Due to these factors, $\tau_\nu$ and $S_\nu$ are frequently used in place of $\alpha_\nu$ and $j_\nu$.

We already know how to examine what happens to the intensity of a beam of light as it travels through an emitting and absorbing medium. What we can ask now is what happens with the medium. Whenever the medium absorbs a photon, its total energy increases; with that, its thermal energy, and then a photon could be reemitted through thermal radiation. A medium is said to be in thermal equilibrium when the absorption/emission rate equals unity. The best way to explore thermal emission is to talk about blackbody radiation, which is thermal radiation emitted by matter in thermal equilibrium..

A blackbody is a body that emits thermal radiation in the form of the *Planck Spectrum,*

as defined by the following equation.

$$B_\nu = \frac{2h\nu^3/c^2}{\exp(h\nu/kT) - 1},\tag{1.7}$$

where $B_\nu$ is the spectral radiance of a body for frequency $\nu$, $T$ is the body's temperature, $k$ is the Boltzmann constant, $h$ is the Planck constant, and $c$ is the speed of light. This radiation $B$ is homogeneous and isotropic, and it solely relies on temperature.

Now, if a body is in thermal equilibrium, we have $S_\nu = B_\nu(T)$. Thus, we have the relation

$$j_\nu = \alpha_\nu B_\nu,\tag{1.8}$$

called the *Kirchhoff's law*, which is an expression between $\alpha_\nu$ and $j_\nu$ with the temperature $T$. With this new relation, we can write the transfer equation of eq.1.5 for thermal radiation as

$$\frac{dI_\nu}{ds} = -\alpha_\nu I_\nu + \alpha_\nu B_\nu(T),\tag{1.9}$$

or

$$\frac{dI_\nu}{d\tau_\nu} = -I_\nu + B_\nu(T).\tag{1.10}$$

Pure thermal radiation is the simplest radiative transfer scenario to handle. Reality, however, is almost always more complicated. This is because scattering, another common phenomenon, can remove light from a beam as it moves through a dense region or add rays to it as light from elsewhere makes its way into it. After we include this effect in the radiative transfer equation, the source function can no longer be $B_\nu(T)$; instead, it now relies on the solution in all directions over any given point. The equation also becomes integrodifferential when scattering is involved, posing a difficult mathematical challenge that must naturally be resolved using numerical methods.

The formality of the transfer equation helps us comprehend the intricate relationship between light and matter in any general scenario, where thermal radiation and scattering play a crucial role. However, we are figuring out how to handle this in the setting of a planet-forming disc around a young star. Therefore, it is necessary to consider the disc's shape, composition, and kinematics before getting there.

## 1.2. Physics of protoplanetary discs

Protoplanetary discs are, in a sense, by-products of star formation, as previously mentioned. In that way, as they form from a gravitationally collapsing gas cloud, their origins are pretty chaotic. As a result, there are several potential pathways for their evolutionary processes, which result in discs with a rich mixture of simple and complex molecules and displaying a variety of structures and substructures.

### 1.2.1. Disc composition

PPDs are made from the same raw material as the host star and are typically composed of $99\,\%$ gas and just $1\,\%$ dust (Hogerheijde, 2011). That gas is composed mainly of molecular hy-

drogen $H_2$, and the following most abundant molecules would be $^{12}CO$ and its isotopologues, $^{13}CO$ and $C^{18}O$ (France et al., 2014). After those, several other molecules swim alongside hydrogen, some of which are $N_2$, CN, HCN, $H_2O$, $H_3N$, SO, and $NH_3$ (Guilloteau et al., 2016, 2013; Hogerheijde et al., 2011; Thi et al., 2001; Koerner et al., 1993; Dutrey et al., 1997).

Although it is only $1\%$ of the total mass, dust plays a crucial role in determining the temperature structure of protoplanetary discs since it is primarily responsible for the opacity in these discs. The opacity measures the ability of photons to pass through a medium. Dust opacity depends strongly on its mineral composition and geometry, both in size and shape. To obtain the composition of such dust, we can examine the spectra of these distant sources and identify distinct sets of features that serve as tracers of dust mineralogy. For example, using Mid-infrared observations, it has been found that dust in protoplanetary discs has traces of amorphous silicates, crystalline silicates, water-ice, and a substantial fraction of carbonaceous material (Waelkens et al., 1996; Meeus et al., 2001; van Boekel et al., 2005; Draine, 2009). However, some types of dust lack noticeable features but still contribute significantly to the overall opacity, like dust grains with iron and carbon. They are found in Solar system meteorites and assuming that the same materials are in some measure in the dust of protoplanetary discs, they should be present there too (Urey and Craig, 1953).

Apart from the chemical composition, grain size is equally influential in determining the dust's opacity. While molecular clouds and the interstellar medium (ISM) have low densities, inhibiting the growth of the dust particles, protoplanetary discs have high densities, which are favourable for dust growth. There, grains collide frequently and grow through coagulation (Weidenschilling, 1980). It is beyond the scope of this thesis to explore the ongoing poor understanding of dust growth. However, in any case, this results in a particle size distribution typically approximated by a power law in size (Mathis et al., 1977). It has been observed that the grain size distribution in PPD follows the same power law as that in the ISM, with a greater upper limit extending to grains with millimetres sizes (e.g. Rosenfeld et al., 2013; Casassus et al., 2018). The microphysics of the dust and the general characteristics and age of the disc will determine the details of the size distribution.

It is possible to determine the absorption and scattering opacities for any particular grain size and dust composition. First, we choose a grain size and then composition. For that, grain optical properties for a variety of molecular compositions can be found in the databases[2] or the literature (Draine, 2003; Li and Greenberg, 1997) and can be mixed using the Bruggeman formula to form more diverse dust compositions. Dust grains are usually amorphous, however, it is common to approximate dust grain geometry to a compact spherical particle so that Mie Theory can apply (Mie, 1908). Mie Theory is a collection of solutions for light scattering by a homogeneous sphere, and standard packages are available to compute the radiative transfer parameters using it. In what follows, we show the results of the Python transcription of **bhmie.f**[3] code, available as part of the RADMC3D Monte-Carlo radiative transfer package (more on this package in sec. 1.4). Following this method, we calculated the opacities for a grain of one micron and one of hundred microns as if they were composed of $70\%$ Astrosilicates and $30\%$ amorphous carbon (ISM mix), and for a one-micron grain made up of $70\%$ silicates and $30\%$ ice (icy mix). The opacities of such grains are shown in

---

[2] One of the most complete is https://www.astro.uni-jena.de/Laboratory/OCDB/index.html.

[3] Available here: https://en.wikipedia.org/wiki/Codes_for_electromagnetic_scattering_by_spheres

Fig. 1.2, where it is clear that the values are indeed strongly dependent on composition and grain size.
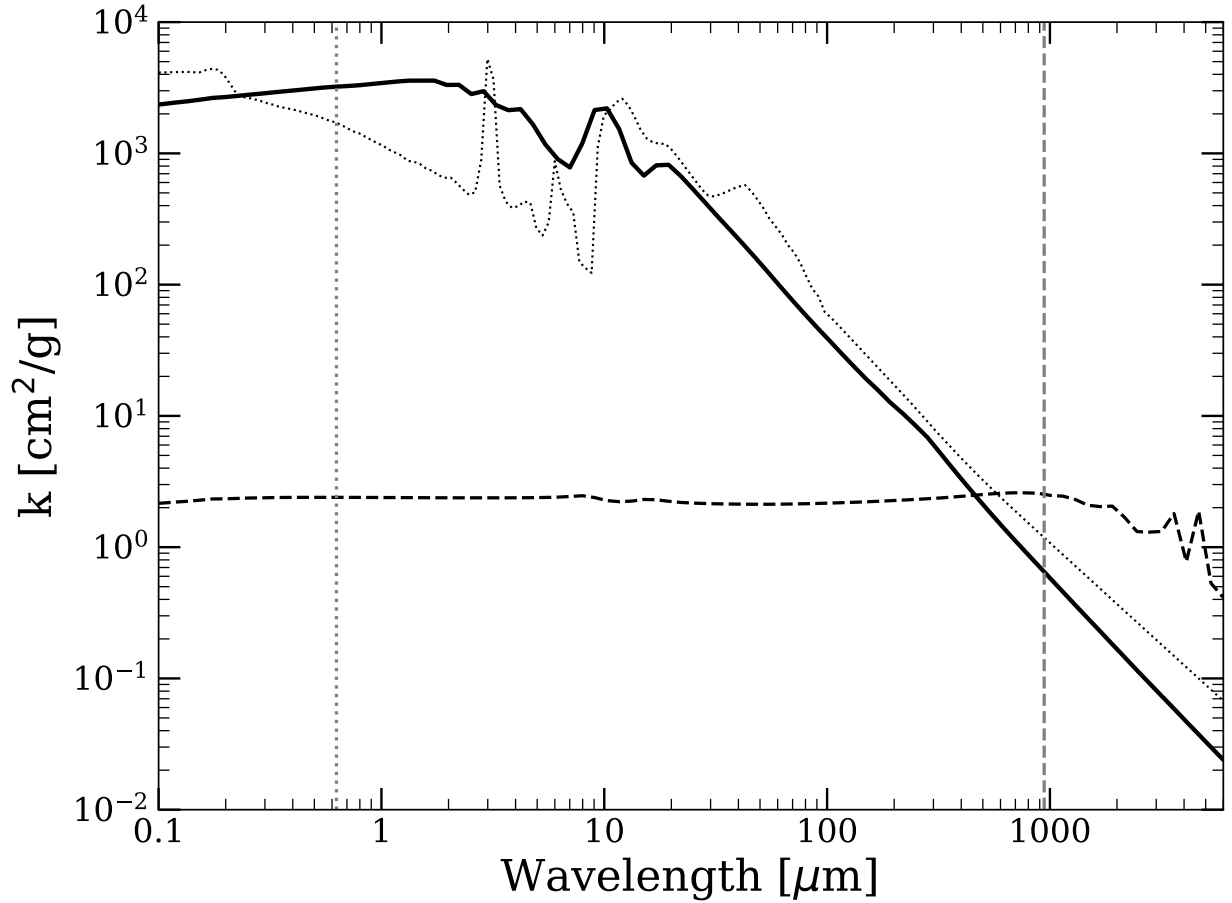


Figure 1.2: Dust opacities of spherical small and large grains. The solid line depicts a grain with a diameter of one micron made up of 70 % Astro-silicates and 30 % amorphous carbon, while the dotted line depicts a same-sized particle made up of 70 % Astro-silicates and 30 % ice. Depicted by the dashed line, a 100 μm particle made up of 70 % Astro-silicates and 30 % amorphous carbon. The approximate wavelengths at which small (0.1 μm) and large (150 μm) dust particles are observed, respectively, are shown by the grey dotted and dashed lines.

In addition, Mie's Theory also gives the scattering phase function, which gives the phase matrix $Z$ that describes the transformation of the Stokes vector of the incident wave into that of the scattered wave. Then, the element $Z_{11}$ determines the angular distribution of the scattered intensity, shown in Fig.1.3, where $\theta = 0 \deg$ represents forward scattering and $\theta = 180 \deg$ backward scattering, so that a straight line would correspond to isotropic scattering. This figure shows how the phase function of a spherical particle can change depending on its optical properties and the opacity's dependency on the scattering angle. The comparison is between two 1 μm dust particles with the same properties as the ones described above, with another made of 60 % Astrosilicates, 20 % amorphous carbon, and 20 % ice (icyISM mix).
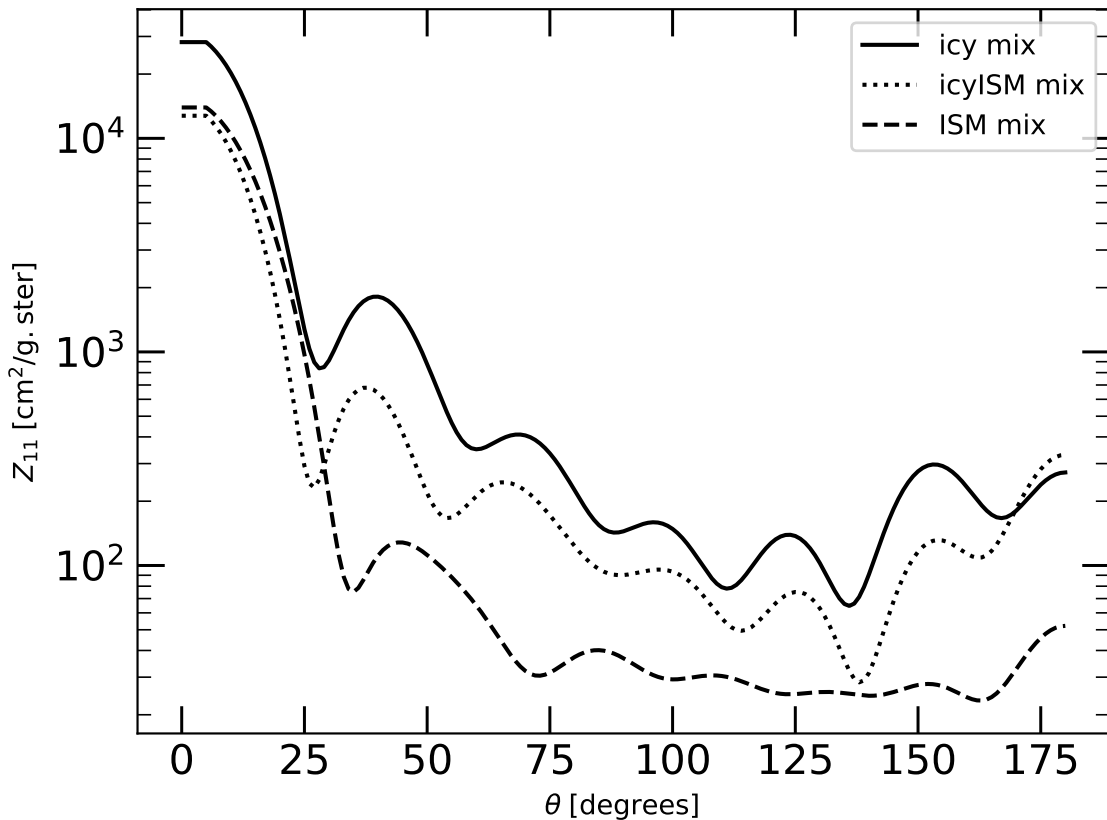
Figure 1.3: The image shows the angular distribution of the scattered intensity from a spherical dust particle of different compositions calculated using Mie theory.

### 1.2.2.  Disc structure

Although discs are three-dimensional objects, they are mathematically thin because their radial dimension is far greater than their height (as illustrated in Fig. 1.1). As a result, we can use a convenient simplification and explain their geometry solely in terms of surface density $\Sigma$, and the equations describing the radial structure and those explaining the vertical structure can be decoupled from one another. When picturing a PPD, the most simple disc would be a flat, axisymmetric one with a power-law gas density distribution that gradually decreased with increasing radii. The star's accretion and photoevaporation truncate its inner radius while its outer radius may extend beyond 500 au (Najita and Bergin, 2018). However, most discs differ from this basic structure and present arrangements of multiple rings, gaps, cavities, spirals, or asymmetries (e.g. see Avenhaus et al., 2018; Andrews, 2020, and references inside). Either way, we can follow a few rules and assumptions that allow us to create a framework from which we can work.

First, the geometry of a disc will mostly be determined by the gas component, which accounts for most of the mass of the disc. Typically, it is safe to assume that the total mass of the disc is much smaller than the mass of the star hosting it ($M_{\mathrm{disc}} << M_*$), which allows

us to neglect the disc's own gravitational potential and rely just on stellar gravity when studying the motion of the gas. Thus, we can assume that the gas follows Keplerian orbits, with $\Omega(r) = \sqrt{GM_*/r^3}$ its Keplerian angular velocity. Then, let us consider a disc in hydrostatic equilibrium, meaning that all the relevant forces should be balanced. This assumption implies that the acceleration caused by the vertical pressure gradient of the gas balances out the gravitational acceleration in the z-direction of the star. Finally, for simplicity, we assume a vertically-isothermal disc so that we can adopt an isothermal equation of state ($P = \rho c_s^2$).

The vertical density profile in this limit has the following basic structure:

$$\rho = \rho_0 e^{-z^2/2h^2} \tag{1.11}$$

where $\rho_0$, the mid-plane density, can be derived directly from the surface density $\Sigma$ as

$$\rho_0 = \frac{1}{\sqrt{2\pi}} \frac{\Sigma}{h}, \tag{1.12}$$

and $h$, the vertical disc pressure scale height, is given by, $h(r) = c_s/\Omega$, with $c_s$ the corresponding isothermal sound speed. Moreover, following these assumptions, the vertical structure will not be flat but flared, meaning that the upward curvature of the disc surface increases with distance from the star. Then the aspect ratio changes as follows:

$$\frac{h}{r} \propto r^{1+\beta}, \tag{1.13}$$

where $\beta$ is referred to as the flaring index. In calculating this index, one must proceed with caution, as the main source of uncertainty comes from the radial dependence of the temperature. The flaring index will change significantly depending on the selected radial temperature dependence, running between 0.1 and 0.7 (see Kenyon and Hartmann, 1987; Chiang and Goldreich, 1997, for different approaches).

What about dust? The dust particles are carried along in this gas disc's orbit but only to a certain degree, depending on the Stokes number. The *Stokes number* determines the coupling of the dust and gas. It is expressed as

$$\mathrm{St} = \frac{1}{2} \frac{\pi a_{\mathrm{gr}} \rho_{\mathrm{d}}}{\Sigma_{\mathrm{g}}}, \tag{1.14}$$

where $a_{\mathrm{gr}}$ is the grain size, $\rho_{\mathrm{d}}$ is the density of a dust grain, and $\Sigma_{\mathrm{g}}$ is the local gas surface density. So dust particles can behave in one of three ways: dynamically coupled to the gas, completely independent, or in a state in between. The first group includes micron-sized grains, which follow the flow of the gas. In the second group, boulders with diameters greater than one metre belong due to their being too large to be disturbed by the surrounding gas. The third set of grains, which includes the millimetre- and centimetre-sized ones, will only partially follow the gas, where depending on the gas densities of their surroundings, the Stokes numbers of these grains will typically shift dramatically over brief times (compared to any other time-dependent dynamic of the system), coupling and decoupling. The vertical structure of the dust disc is significantly impacted by this dynamic decoupling-coupling of the dust and gas, a process known as dust settling (Dullemond and Dominik, 2004).

Following Armitage (2010), imagine a dust particle the size of a fraction of a micron growing in the disc at a distance $r$ from the star and a height $z$ above the midplane of the disc. As we know, we begin by assuming that the gas is in vertical hydrostatic equilibrium, meaning no acceleration in the z-direction, so if the grain is completely coupled to the static gas, it stays at its current height. Now, as the grain grows, and so does its Stokes number, it partially decouples from the gas dynamics. As a result, the dust will move toward the midplane, where gas densities are higher, bringing the Stokes number back down until the grain is coupled again. Still, even at the midplane, the grain might not be coupled, but it will stay there because it is the vertical centre of gravity. Because of this motion, the grain sizes stratify, with the larger grains settling close around the midplane and the smaller ones with a density maximum at the midplane but distributed further up. Of course, the gas turbulence also provides random velocities to the dust particles, which diffuses the dust and makes this stratification not so rigid. Still, this phenomenon makes the dust disc typically thinner than the gas disc (D'Alessio et al., 1999). This is well illustrated in Fig. 1.4, where the larger grains are represented in darker grey, and their height is only a portion of the total.

The building of the radial structure involves yet another dust grow-related process. A radial pressure gradient partially supports the gaseous component that orbits at slightly sub-Keplerian velocities, dragging small dust grains. However, as the grains grow and decouple from the gas, they lose the pressure support and orbit faster than the gas, making them feel a headwind that slows them down, and in case of gas radial pressure smoothly decreasing outward, particles drift inward. This aerodynamic effect is the *Weidenschilling drift*, which occurs as the particle collides with individual gas molecules. The change in velocity will increase with size and, depending on the composition of the dust, peak at roughly meter size and decrease at larger sizes. This effect could result in the rapid depletion of the disc's solids needed for planet formation, as all growing grains would fall toward the star (Weidenschilling, 1977). This problem is called the *radial-drift* or the *metre-size barrier* (see Andrews, 2020, for evidence of radial drift). Fortunately, some mechanisms can prevent large grains from drifting too far and getting lost in the star. The typical solution involves pressure bumps formed by still-forming planets within the disc, interrupting the migration by creating ripples, gaps, or rings in the radial dust distribution (Teague et al., 2019; Rosotti et al., 2020; Weber et al., 2018). Unfortunately, this and other solutions for dust-trapping mechanisms are not yet well understood. Ultimately, the wide range of morphologies in protoplanetary discs makes the problem of having a general equation for its radial structure highly degenerative. Regardless, it is common to see the use of step functions, power-laws or Gaussians to depict extended discs and rings.
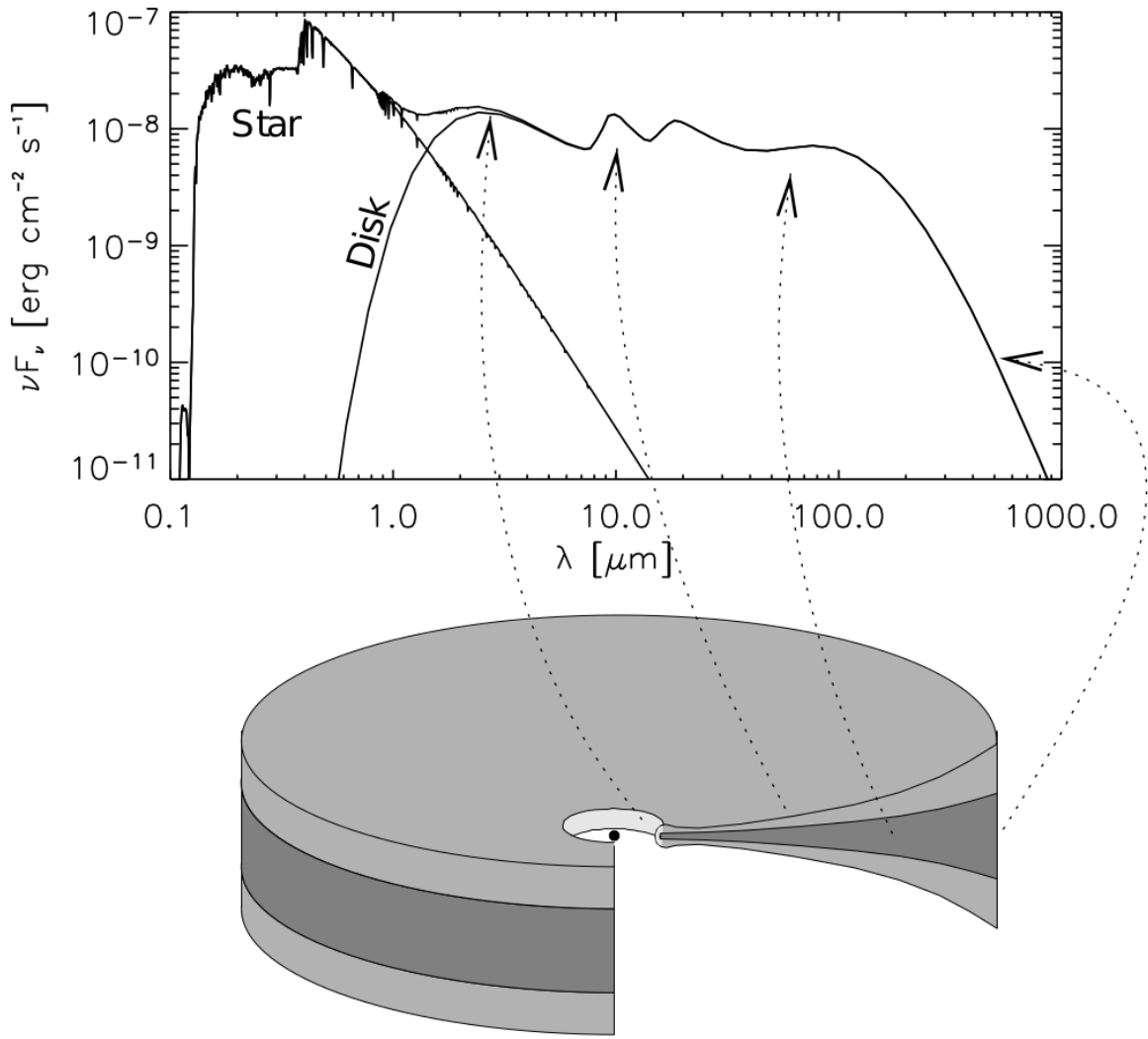
Figure 1.4: Simple geometrical illustration of an axisymmetric flared disc that is vertically stratified. The image also shows a corresponding Spectral Energy Distribution (read sec. 1.5.1). Indicated in light grey, the disc's surface layers emit near- to mid-infrared because they directly interact with star radiation. In contrast, the material in the disc's midplane, seen in a darker shade of grey, is well protected from star radiation and, as a result, is colder and radiates light at longer wavelengths. Figure taken from Dulle-mond et al. (2007).

## 1.3. Radiative Transfer in discs

We might wish to use the ideas we have covered to comprehend how the temperature changes in a protoplanetary disc. Unfortunately, we cannot do so because radiative transfer equations in arbitrary geometries, including that of a flared disc, lack complete analytical solutions. However, even without a perfect analytical description of the thermal structure of a PPD, there are still certain noteworthy characteristics which could be derived using simple assumptions and simplifications.

First, ignoring any effect from viscous heating, we can assume that the main heat source in protoplanetary discs is its central star, and we know that the vertical structure of the disc determines the amount of radiation it can absorb and reemit to a large extent. Assuming a thin disc geometry, we can approximate the vertical dust grain distribution due to dust settling by dividing the disc into an optically thick midplane and a radially thick but vertically thin surface layer. The top layer will get warmer as it absorbs direct radiation from the star. After that, on the assumption of thermal equilibrium, it radiates an equal amount of energy towards space and the optically thick interior. Naturally, the interior layer will be cooler than the surface layer as the latter protects it from direct stellar radiation, receiving heat only through the thermal emission of the above layer (see Fig. 1.4). This simple two-layer method shows discs are not vertically isothermal, so the actual vertical structure will deviate from the Gaussian distribution in equation 1.12.

Analogously, we must expect that the inner radius of the disc, as the radiation is hitting it more directly, will be the hottest section and will heat the disc radially, but only weakly. However, correctly calculating the radial temperature profile is a complicated challenge, and there are different models on how temperature varies with radius. The physics of this is described in papers by Adams et al. (1987), Kenyon and Hartmann (1987) and Chiang and Goldreich (1997).

Through approximations like the above, we can get a reasonable idea of the temperature field in discs, but we are subject to some restrictions. For example, we did not discuss scattering effects or how to handle shadows created by gaps, bumps, spirals, or non-trivial structures. Therefore, if we want to map the dust temperature of protoplanetary discs with elaborate geometries, numerical radiative transfer programmes are our best remaining alternative.

## 1.4.   Simulating Radiative transfer with MCMC

RADMC3D (Dullemond et al., 2012) is a very sophisticated yet simple code that is one of a select few that allows us to compute dust temperature fields, images and spectra for extremely complicated disc geometries and configurations. The code works as described in the manual[4], but in a nutshell, it is a two-step process: first, it computes the global dust temperature using a thermal Monte Carlo algorithm and then creates the specified images and spectra. Instead of attempting to solve the radiative transfer equation, this code directly deals with the problem by simulating single photons' interaction with the surrounding disc. This algorithm is accomplished using Bjorkman and Wood (2001) Monte Carlo approach while including numerous modifications of Lucy (1999).

The individual interactions of photons with the disc are computed with the following pipeline. First, the sources of energy (stars) are created, specifying their position, spectrum and luminosity. Second, we place the desired gas and dust density distributions on a grid, typically in spherical coordinates, around the star to generate the disc. The disc can be configured in any way we wish, with complete flexibility but no guidance; therefore, one must

---

[4]  The user manual is available at https://www.ita.uni-heidelberg.de/~dullemond/software/radmc-3d/manual_radmc3d/index.html

proceed cautiously. The total brightness is then divided into photon packages, each released by the sources one at a time. As a photon package travels across the grid, the 'energy' of each grid cell it enters increases, raising the temperature of the dust inside that cell. As this happens, the photon has a likelihood of being absorbed, scattered, or not reacting for each grid cell it comes through. In the event that the photon package is absorbed by the dust, it is immediately reemitted in a new direction and with a different wavelength. The new wavelength is selected using Bjorkman and Wood (2001) recipe; however, the luminosity fraction that each photon package represents remains the same. If the package is scattered, it changes the direction of propagation, and in case polarisation is included, its Stokes parameters too, but no change in its wavelength. Following this formula, every photon package will ping-pong across the model and never be lost until it leaves the model through the outside boundary of the grid. Figure 1.5 illustrates the path of a photon package as it travels through a polar grid, being absorbed and reemitted or scattered until it leaves the grid. As the photon package passes through the cells, the temperature of the cells increases, as illustrated by the yellow arrows. After it escapes, the following photon package is emitted, and so forth. The dust temperature that remains present after all photon packages have been emitted and escaped is the final solution to the dust temperature.

It is important to keep in mind two things. First, the calculated temperature is an equilibrium dust temperature. Therefore, it is assumed that all dust grains absorb the same amount of energy they emit. Fortunately, given that the heating and cooling times for dust grains are often relatively short compared to any time-dependent dynamics of the system, this approximation is likely very accurate in most cases. Secondly, that RADMC3D is, in a way, *"just a dumb computational engine"* (their words, not mine), as it does not know what discs mean or anything about dust's physical properties; it depends entirely on input files. Therefore, crucial parameters such as the opacities or the scattering efficiencies for the dust populations must be computed beforehand. It is up to the user to decide how to create these input files. Regardless, RADMC3D does provide a python script that can be used to obtain the scattering matrix, where we can use the optical constants from the databases (see section 1.2.1) to generate the necessary files.
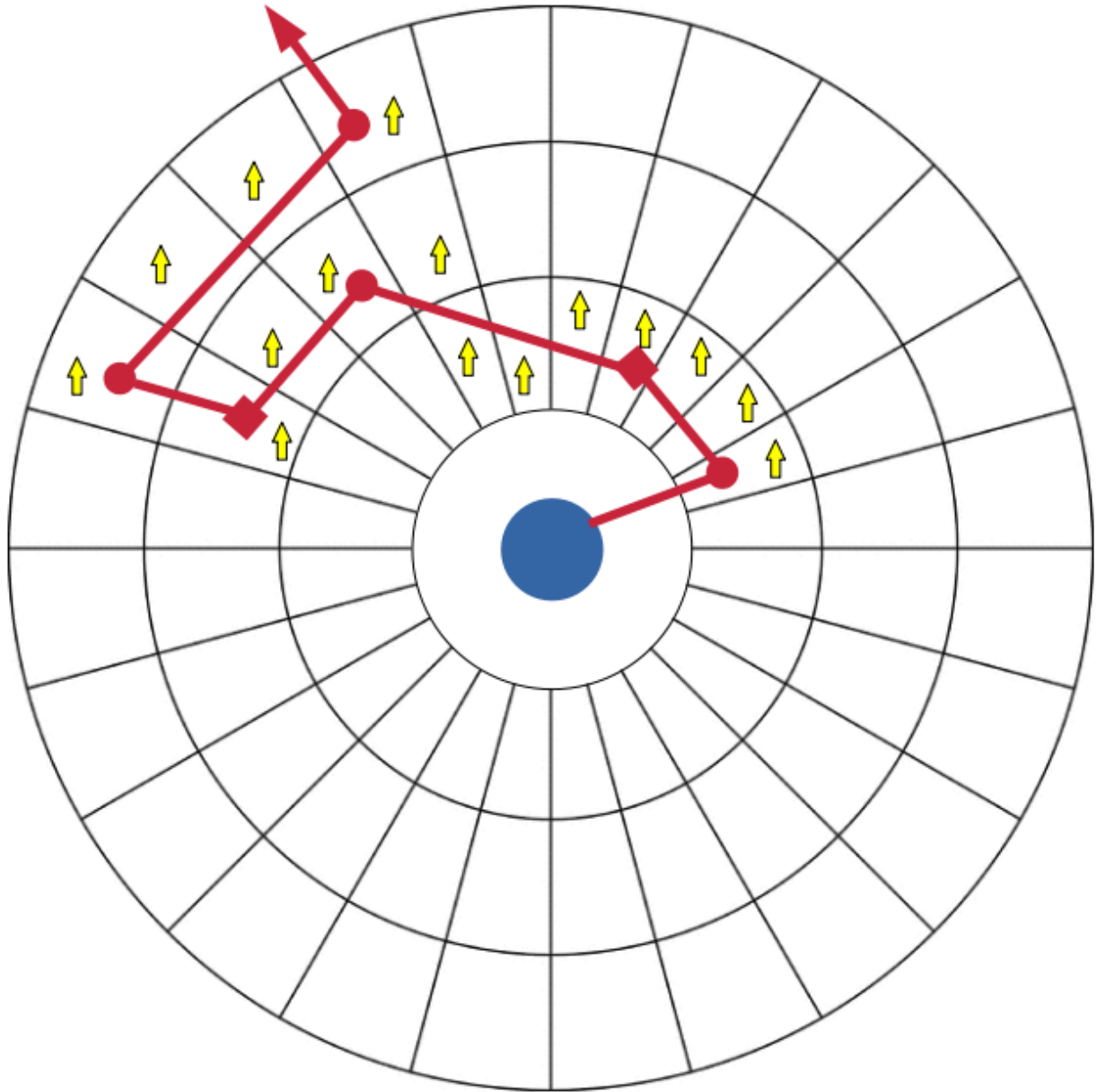
Figure 1.5: Journey of a photon package through a polar grid. The photon package (solid red line) is emitted by the star (blue circle), and changes direction and frequency after each absorption/re-emission event (red circles) or just direction after each scattering event (red squares) until it eventually escapes the disc. The yellow arrows show the increase in temperature on each cell the photon crossed.

## 1.5.   Observing dusty discs

We now understand that as the disc is lighted by its host star, the dust absorbs part of the light and scatters others. This process causes the dust to heat up and radiate outward at various wavelengths depending on its intrinsic characteristics. Using ground and space-based telescopes, we can observe these effects and, depending on the method, extract specific insights about the structure of a disc. Accordingly, as a result of significant improvements in

this regard, the study of planet formation has been revolutionised by recent observations of protoplanetary discs.

## 1.5.1.   Spectral Data

The Spectral Energy Distribution (SED) measures the energy released at different wavelengths and offers important details on the mass, temperature, and distribution of dust populations. It is also practical for classifying discs at different stages of evolution (Lada, 1987; Adams et al., 1987). A SED may typically be constructed using photometry and spectroscopic data found in archives[5] or the literature, and it should include enough data points to distinguish between the emission coming from the star and that coming from the disc.

When looking at a star that hosts a disc, the emission from the star dominates the SED at short wavelengths like the optical, but as one moves to longer wavelengths and reaches the near-infrared and radio, the radiation coming from the disc begins to take protagonism. Hence, we can deduce its radial structure based on how much the disc emission will outweigh the star emission at each wavelength range. For example, a disc with a deep valley in the infrared spectrum may indicate an inner gap with little to no dust in the inner regions. Alternatively, a lack of millimetre emission may indicate an unextended dust disc or a relatively small population of larger dust particles. Following these interpretations, the overall intensity of the disc emission will serve as an excellent proxy for the total dust mass and, consequently, the total mass of the disc. These effects are illustrated in Fig. 1.6, where these exact behaviours become apparent when altering the inner or outer radius or the mass of a given model.

Lastly, the SED also shows other notable characteristics for studying dust chemical composition in PPD. For instance, the heated micron-sized dust at the disc surface will produce a strong emission feature at $10\,\mu\mathrm{m}$, and its amplitude and width give hints of changes in the composition and grain growth (Cohen and Witteborn, 1985; van Boekel, R. et al., 2003).

## 1.5.2.   Radio continuum and Infrared Polarised imaging

We can also measure how the intensity of a single wavelength fluctuates over the source's spatial coordinates rather than measuring the total intensity across all wavelengths. With this, due to the dependence of this emission on dust opacity, we can directly map the density distributions of different grain size populations just by observing at distinct wavelengths. For instance, the small grains dominate the optical and near-infrared emission, whereas the larger grains are visible at (sub) millimetre wavelengths. The typical approximation is that the observed size grain will be $a_{\mathrm{grain}} = \lambda/2\pi$.

---

[5]   For example, the Spitzer infrared spectroscopic data archive https://irsa.ipac.caltech.edu/data/SPITZER /docs/spitzerdataarchives/
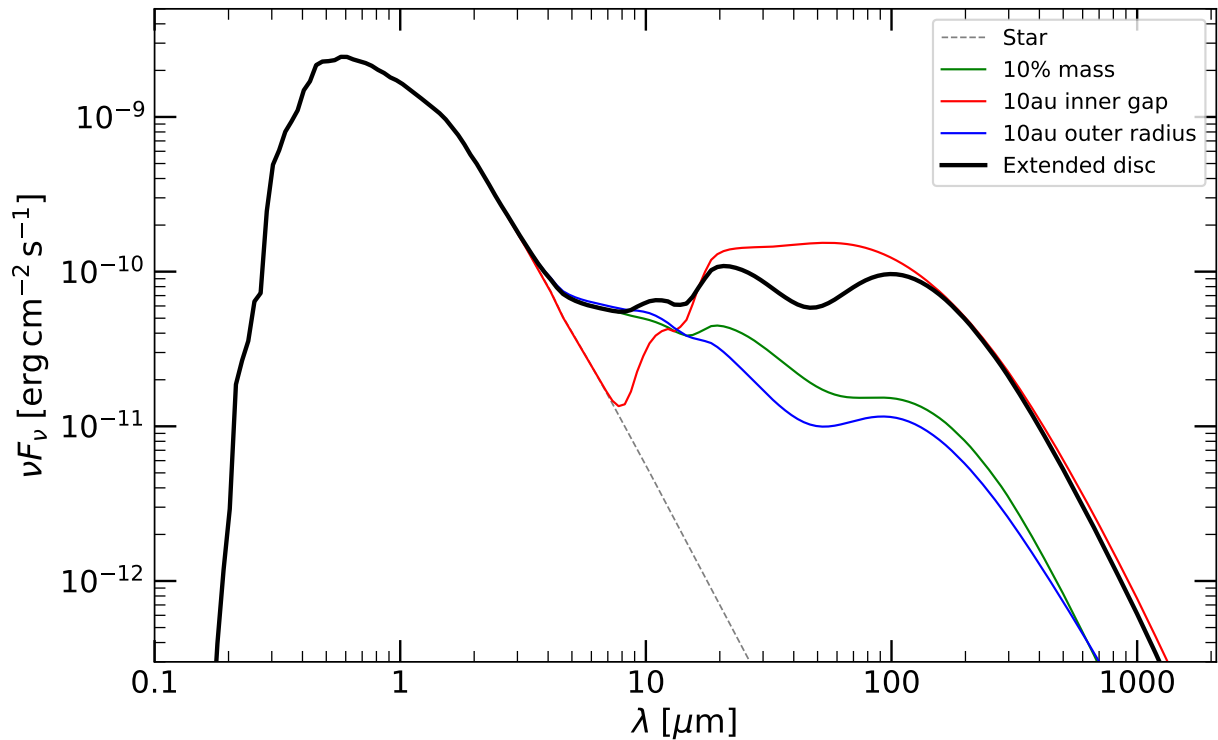
Figure 1.6: A comparison between several SEDs corresponding to different model discs with different properties. In black, an extended disc serves as a reference point for contrasting. The SED in blue comes from an equally massive but radially narrower disc that is only 10 au across, while a disc with the same mass and a 10 au inner cavity produce the one in red. The green SED comes from a model with the same disc geometry as the black but only 10 % of the mass.

However, if we consider that the light emitted by stars is unpolarised but becomes partially polarised when reflected by a surface (such as a dust particle), more information can be obtained from the observations. Due to the anisotropic light scattering of actual grains, the scattering efficiency can therefore be used to determine the level of dust present in discs (e.g. Pantin et al., 2000). Moreover, because scattering is more effective in particles with diameters roughly equal to the wavelength of the incident ray, the micron-sized dust particles on the flared surface will be the most effective scatterers of near-infrared emission.

Consequently, the disc structure can be explored by means of comparing the mm continuum and scattered light images. While the mm continuum traces the distribution of large grains settled in the midplane, scattered infrared light accounts for photons reflected off small dust at the disc surface layer. This means that whether scattered light asymmetries correspond to surface ripples or deep structures intrinsic to the underlying density distribution can be determined by searching for the millimetre counterparts of these asymmetries. For doing so, we utilise radio interferometers such as the Atacama Large Millimeter Array (ALMA) to observe the radio continuum and instruments such as the Spectro-Polarimetric High-contrast Exoplanet REsearch (SPHERE) and the InfraRed Dual-band Imager and Spectrograph (IR-DIS) in the Very Large Telescope (VLT) to look at near-infrared polarised light.

ALMA works as an interferometer, an array of 66 radio telescopes that cooperate to achieve greater sensitivity and resolution than they could achieve on their own. If we took only two antennas, it is possible to show that the angular resolution is

$$\Theta(\text{arcsec}) = 2\lambda_{\text{cm}}/D_{\text{km}}, \tag{1.15}$$

where $D$ is the baseline, i.e. the projected distance of the antennas. Going beyond a two-element interferometer, with the whole array with baselines as large as $13\,\text{km}$, ALMA angular resolution for millimetre and submillimetre radio wavelengths is astonishing and unprecedented.

It is important to note that these telescopes do not capture images; rather, they measure the Fourier transform of the sky brightness $B$,

$$V(u,v) = Ae^{-i\phi} = \int \hat{A}(x,y)B(x,y)e^{-i2\pi(ux+vy)}dxdy, \tag{1.16}$$

where $A$ is the amplitude, and $\phi$ is the phase of the complex visibility, $(u,v)$ are the coordinates of the baseline in units of wavelength $\lambda$, $(x,y)$ are the relative distance from a reference point, $\hat{A}$ is the primary beam correction. Each pair will give two points in the $V(u,v)$ space that, via a Fourier transform, reconstruct the sky brightness.

$$B'(x,y) = \hat{A}(x,y)B(x,y)Ae^{-i\phi} = \int V(u,v)e^{i2\pi(ux+vy)}dudv, \tag{1.17}$$

We will want to fill the $V(u,v)$ space as much as possible, as the more coverage we have, the better the reconstruction will be. Going beyond a two-element interferometer, using multiple antennas, we can mix larger and shorter baselines, increasing the coverage significantly. Then, the resolution is given by the longest distance between antennas (called the synthesised beam), and the shortest distance between antennas gives the largest angular scale that can be imaged. This Fourier relation is the van Cittert-Zernike theorem, on which aperture synthesis interferometry is based.

The VLT, on the other hand, consist of four Unit Telescopes with primary mirrors of $8.2\,\text{m}$ diameter, making it the world's most advanced visible-light astronomical observatory, incorporating instruments such as SPHERE/IRDIS to obtain images in polarised near-infrared light. This method is challenging because stars continue to shine brightly in this range of wavelengths, masking the emission from the disc. As a result, it needs to use coronagraphs, an attachment that obscures the star's direct light so that the emission from the disc may be seen distinctly. The unpolarised starlight is then removed from an image via polarimetry, which enables SPHERE/IRDIS to observe protoplanetary discs much more clearly. This process is driven by a filter that only permits light with a specific polarisation direction to pass through. SPHERE/IRDIS uses one vertical and one horizontal polariser to measure polarisation. A light beam is split into two channels, one with a vertical polariser and one with a horizontal polariser, and the images produced by each are recorded. When one image is subtracted from the other, all unpolarised light is subtracted altogether, leaving only the polarised light behind.

## 1.6. Summary: thesis outline

In this thesis, we use the radiative transfer code RADMC3D to connect the physics of protoplanetary discs to observations.

In chapter 2, we examine the system of V4046 Sgr. First, using multi-wavelength data, we study the geometry of the protoplanetary disc. Then, we developed a multi-parameter model using radiative transfer simulations to constrain the vertical and radial structure. The resulting model, as it shows an excellent fit to the data, also gives reasonable approximations of the dust populations in the disc. This chapter is the culmination of a long project that led to a publication in Martinez-Brunner et al. (2022)

In chapter 3, we implemented a similar methodology, i.e. developed a parametric model to reproduce multi-wavelength data, but for a different source, the protoplanetary disc of ISO-Oph 2 A. Only this time, we searched for possible environmental effects on the thermal structure of the disc. This project is still under development and is framed in the context of a resurgence of interest in environmental effects on circumstellar discs.

Finally, this manuscript ends with general conclusions about the field, the results from each project, the methodology and the impact of this research.

# Capítulo 2

# V4046 Sgr: a disc with a thin ring

## 2.1. Abstract

The nearby V4046 Sgr spectroscopic binary hosts a gas-rich disc known for its wide cavity and dusty ring. We present high resolution ($\sim$20 mas or 1.4 au) ALMA observations of the 1.3 mm continuum of V4046 Sgr which, combined with SPHERE–IRDIS polarised images and a well-sampled spectral energy distribution (SED), allow us to propose a physical model using radiative transfer (RT) predictions. The ALMA data reveal a thin ring at a radius of 13.15$\pm$0.42 au (Ring13), with a radial width of 2.46$\pm$0.56 au. Ring13 is surrounded by a $\sim$10 au-wide gap, and it is flanked by a mm-bright outer ring (Ring24) with a sharp inner edge at 24 au. Between 25 and $\sim$35 au the brightness of Ring24 is relatively flat and then breaks into a steep tail that reaches out to $\sim$60 au. In addition, central emission is detected close to the star which we interpret as a tight circumbinary ring made of dust grains with a lower size limit of 0.8 mm at 1.1 au. In order to reproduce the SED, the model also requires an inner ring at $\sim$5 au (Ring5) composed mainly of small dust grains, hiding under the IRDIS coronagraph, and surrounding the inner circumbinary disc. The surprisingly thin Ring13 is nonetheless roughly 10 times wider than its expected vertical extent. The strong near-far disc asymmetry at 1.65 $\mu$m points at a very forward-scattering phase function, and requires grain radii of no less than 0.4 $\mu$m.

## 2.2. Introduction

Recent observations of young circumstellar discs have transformed the current knowledge on planet formation. Among the main recent findings of resolved observations of discs is the discovery of substructures in the form of gaps, rings, cavities, and spirals, to name a few (see, Andrews, 2020, and references there in). However, the focus of resolved imaging with the Atacama Large Millimeter/submillimeter Array (ALMA) or with the current generation of high-contrast cameras has mainly been towards the brighter sources (e.g., Garufi et al., 2017). It is to address this bias that the "Discs Around T Tauri Stars with SPHERE" (DARTTS-S) programme collected differential polarisation imaging (DPI) data with the Spectro-Polarimeter High-contrast Exoplanet REsearch (Beuzit et al., 2019) for a total of 29 solar-type stars (Avenhaus et al., 2018; Garufi et al., 2020). The sample is not biased towards exceptionally bright and large discs. The DARTTS observations revealed diverse structures and morphologies in the scattering surface of these discs. This article on V4046 Sagittarii (Sgr) is the first instalment of a companion programme, the DARTTS survey with ALMA

(DARTTS-A), which will present millimetre observations of nine protoplanetary discs previously imaged in polarised scattered light in DARTTS-S.

V4046 Sgr is a double-lined spectroscopic binary of K-type stars (K5 and K7) with very similar masses of $0.90\pm0.05\,\mathrm{M_\odot}$ and $0.85\pm0.04\,\mathrm{M_\odot}$ (Rosenfeld et al., 2012), on a close ($a \approx 0.041\,\mathrm{au}$), circular ($e \leq 0.01$) orbit, with an orbital period of 2.42 days (Quast et al., 2000). It is a member of the $\beta$ Pictoris moving group (Zuckerman and Song, 2004), with an estimated age of $18.5^{+2.0}_{-2.4}\,\mathrm{Myr}$ (Miret-Roig et al., 2020), and its distance is $71.48\pm0.11\,\mathrm{pc}$ (Gaia Collaboration et al., 2021). V4046 Sgr hosts a massive ($\sim 0.1\,\mathrm{M_\odot}$) circumbinary disc extending to $\sim 300\,\mathrm{au}$ (Rosenfeld et al., 2013; Rodriguez et al., 2010), rich in diverse molecular lines (Kastner et al., 2018).

Previous analysis of radio observations taken with the Sub-Millimeter Array (SMA) (Rosenfeld et al., 2013) and later with ALMA (Guzmán et al., 2017; Huang et al., 2017; Bergner et al., 2018; Kastner et al., 2018), showed that the millimetre dust of the V4046 Sgr circumbinary disc features a large inner hole of $\sim 30\,\mathrm{au}$ and a narrow ring centred around 37 au that account for most of the dust mass. More recently, Francis and van der Marel (2020), with higher definition ALMA images, detected a structured outer disc with an inner disc in the millimetre continuum. On the other hand, by using SPHERE polarised light observations in the J- and H-band, Avenhaus et al. (2018) confirmed the double-ring morphology previously reported by Rapson et al. (2015) using GPI data. In these polarised light observations, the surface brightness presents a $\sim 10\,\mathrm{au}$-wide inner cavity, a narrow ring at $\sim 14\,\mathrm{au}$, and an outer ring centred at $\sim 27\,\mathrm{au}$. Later, Ruíz-Rodríguez et al. (2019) elaborated on the characterisation of the observed rings in the SPHERE images, more on that in Section 2.3.2.

A parametric model that simultaneously fits the NIR scattered light and millimetre continuum emission links the observations to the structures in the underlying dust and gas density distributions, and sheds light on the complex processes that shaped them. In this paper, we present new ALMA observations of the continuum emission at 1.3 mm of V4046 Sgr with unprecedented angular resolution in this source, which reveal an inner ring in the disc. We also reproduce these observations with a 3D parametric model that fits all available data, including the polarised scattered light SPHERE image, the spectral energy distribution (SED), as well as the new high definition 1.3 mm continuum map. Section 2.3 describes the available observations that we aim to model. Section 2.4 describes the structural parameters of our model. A description of our parameter space exploration can be found in Appendix A.1. The results of our modelling are presented in Section 2.5, including a discussion of the main findings. Finally, in Section 2.6 we present our conclusions.

## 2.3. Observations

### 2.3.1. ALMA

New ALMA observations of V4046 Sgr were obtained in 2017 as part of the Cycle 5 program 2017.1.01167.S (PI: S. Perez). The observations acquired simultaneously the 1.3 mm continuum and the J $= 2-1$ line of $^{12}$CO (i.e. with a band 6 211-275 GHz correlator setup). A log of the observations is shown in Table 2.1. The ALMA array was in its C43-8/9

configuration, with baselines ranging from 92 to 13894 m which translate into a synthesised beam of 0."062 × 0."055, in natural weights. Here we focus on the continuum observations only. Francis and van der Marel (2020) included a subset of this dataset, corresponding to the C43-8 configuration, as part of a large sample of transition discs, with a focus on the statistical properties of the inner discs.

Table 2.1: Summary of the new ALMA observations presented in this work. The table shows the total number of antennas, total time on source (ToS), target average elevation, mean precipitable water vapour column (PWV) in the atmosphere, minimum and maximum baseline lengths and maximum recoverable scale (MRS).

| Configuration | Execution Block (uid://A002/) | N Ant. | Date | ToS (sec) | Avg. Elev. (deg) | Mean PWV (mm) | Baseline (m) | MRS (") |
|---|---|---|---|---|---|---|---|---|
| C43-8/9 | Xc6b674/X44f | 48 | 2017-11-10 | 507 | 50.9 | 1.0 | 113.0 - 13894.4 | 0.571 |
| C43-8 | Xc72427/X34f2 | 43 | 2017-11-23 | 507 | 45.2 | 0.4 | 91.6-8547.6 | 0.8 |

Image synthesis of the ALMA continuum was performed with the **uvmem** package (Casassus et al., 2006; Cárcamo et al., 2018), which fits a non-parametric model image $I_j^m$ to the data by comparing the observed and model visibilities, $V_k^\circ$ and $V_k^m$, using a least-squares figure of merit $L$:

$$L = \sum_{k=1}^{N} \omega_k |V_k^\circ - V_k^m|^2 + \lambda S, \tag{2.1}$$

where $\omega_k$ are the visibility weights and $\lambda$ is a dimensionless parameter that controls the relative importance of the regularisation term $S$.

The chosen regularisation term $S$ for this case was the standard image entropy, or

$$S = \sum_{j=1}^{M} \frac{I_j^m}{M} \ln \left( \frac{I_j^m}{M} \right), \tag{2.2}$$

where $M$ is the default pixel intensity value and is set to $10^{-3}$ times the theoretical noise of the dirty map (as inferred from the visibility weights $\omega_k$). Here we set $\lambda = 0.01$. Similar applications of **uvmem** in the context of protoplanetary discs can be found, for example, in Casassus et al. (2013, 2018, 2019a); Pérez et al. (2019) and in Pérez et al. (2020) using long baseline data. An advantage of **uvmem** compared to more traditional imaging strategies, such as provided by the **tclean** task in CASA, is that the effective angular resolution of the model image is ∼3 times finer than the natural weights clean beam (Cárcamo et al., 2018), giving us a new approximate **uvmem** resolution of ∼0."021× ∼0."018. This angular resolution is comparable to uniform or super-uniform weights in **tclean**, but it preserves the natural-weights point-source sensitivity. The RMS noise of the **uvmem** image is 26 μmJy per resolution beam, at a frequency of 237 GHz.

The resulting **uvmem** image shown in the top right panel of Fig. 2.1 reveals new substructure of the disc, in the form of two rings of large dust grains with a broad gap between them, i.e. Ring13 at around ∼13 au and Ring24 starting at around ∼24 au (see below for a precise estimation). The wide and bright Ring24 reaches its peak intensity at ∼30 au, continues re-

latively flat and then breaks at ∼35 au into a steeper tail. While this is the first observation of Ring13, Ruíz-Rodríguez et al. (2019) anticipated its existence as their ALMA continuum image showed a distinct excess between ∼10 and 17 au.

Ring13 is surprisingly narrow and seems to be off-centred relative to the Gaia stellar position, at the origin of coordinates in Fig. 2.1. We determined the centre of the ring and its orientation using the `MPolarMaps` package described in Casassus et al. (2021), which minimises the dispersion of the intensity radial profiles between two given radii and returns the optimal values for the disc position angle (PA), inclination, and disc's centre. In an initial optimisation we focus on the orientation of Ring13, and choose a radial range from 6 to 18 au, which covers Ring13 but excludes Ring24. The resulting disc orientation is set at a PA of 257.31±0.03 deg (east of north), with an inclination of 147.04±0.02 deg, and the optimal ring centre is at $\Delta\alpha = -4 \pm 0.02$ mas $\Delta\delta = 13 \pm 0.05$ mas relative to the Gaia position of the stars. The offset of the centre of the cavity and the nominal stellar positions are coincident within the pointing accuracy of ALMA, which is ∼5 mas for the signal to noise ratio of our image (calculated using the ALMA Technical Handbook).

In a second optimisation of the disc orientation, but this time aiming for Ring24 with a radial domain from 20 au to 70 au (fully including Ring24 and excluding Ring13), we obtained a PA of 256.86±0.02 deg, with an inclination of 146.08±0.01 deg and a centre at $\Delta\alpha = 2 \pm 0.02$ mas $\Delta\delta = 12 \pm 0.02$ mas relative to the stars. We see that both Ring13 and Ring24 share a very similar orientation and centre, given the errors and the pointing accuracy. However, see that there are some hints for a somewhat different orientation in the azimuthal profiles for the ring radii, which may nonetheless be accounted for by the joint effect of all these small differences in disc orientation. This is summarised in Fig. 2.2a, which characterises the radial position and width of Ring13 as a function of azimuth by using radial Gaussian fits at each azimuth. The radial centroids for both disc orientation overlap within the errors, but there is a systematic trend for the difference between the two. It may be that this small difference reflects a finite intrinsic eccentricity of one or both rings. Deeper imaging is required to progress on this question.

On average, we obtained a radial FWHM for Ring13 of 2.83±0.50 au, and a stellocentric radius of 13.15±0.42 au (see Fig. 2.2b). As the `uvmem` model image has an approximate `uvmem` beam of ∼0.″021 × ∼0.″018 (or ∼1.4 au at 71.48 pc), we see that Ring13 is resolved. After subtraction of the `uvmem` beam, the ring width is ∼2.46±0.56 au.

Interestingly, the ALMA image also detects 1.3 mm continuum emission near the stellar positions (see the inset in Fig. 2.1). Since this central emission is larger than the angular resolution, it is probably stemming from thermal emission from large dust grains rather than directly from the stars. The peak intensity of this dust structure is at an estimated distance of only 0.″012 ± 0.″002, or ∼0.85±0.14 au from the binary system, and, estimating its form as a Gaussian ellipse, it has a mean FWHM of ∼1.43 au.
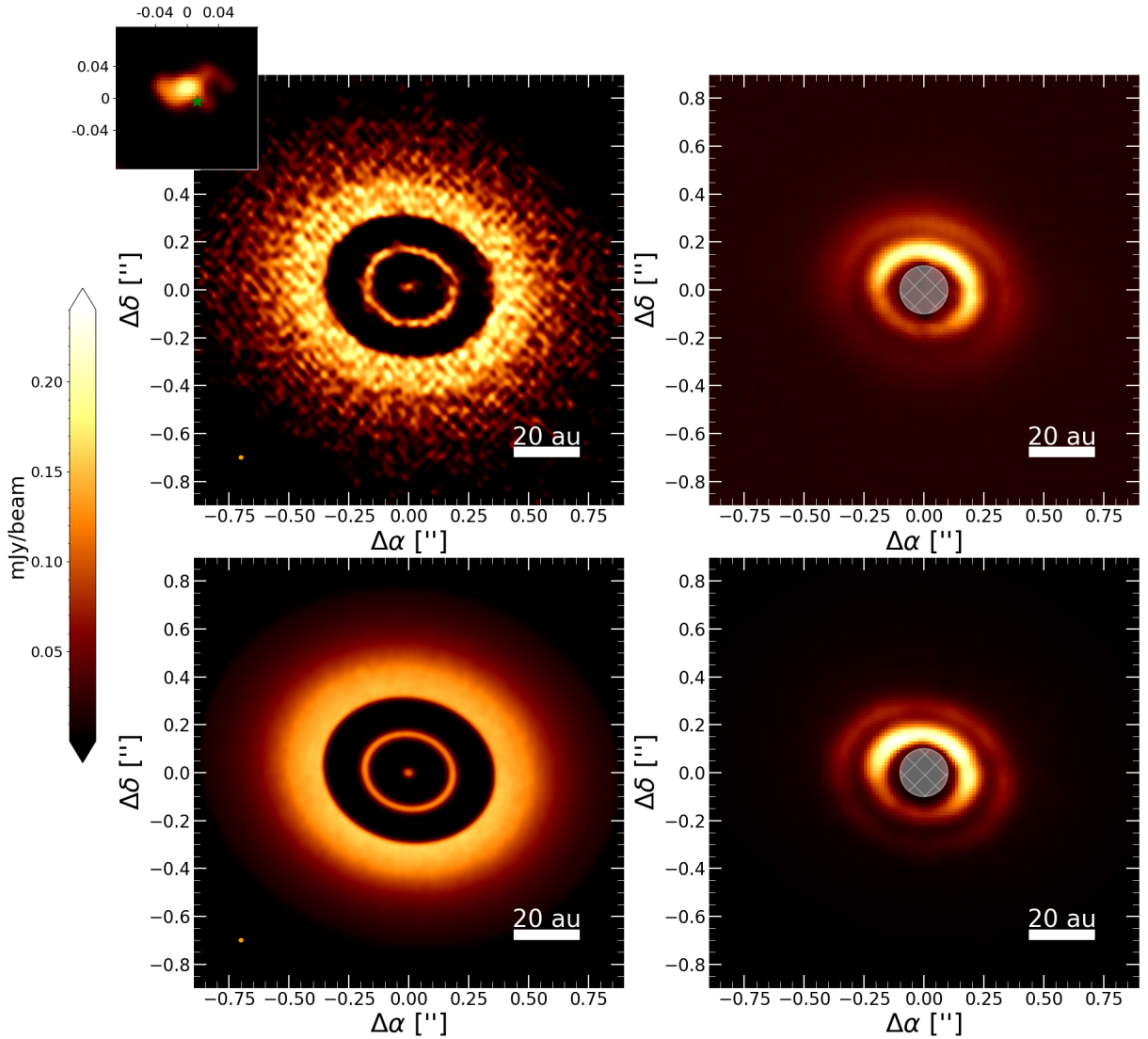
Figure 2.1: Comparison of observations (top) and simulated images (bottom) at 1.3 mm continuum (left) and 1.65 μm (right) of the circumbinary disc orbiting V4046 Sgr. *Top left panel:* 1.3 mm continuum uvmem model image. The small orange ellipse shows an estimated uvmem beam size ($\sim$0$\farcs$021 $\times$ $\sim$0$\farcs$018). The inset zooms into the central emission, and the green star marks the centre of the inner ring. *Top right panel:* SPHERE–IRDIS *H*-band image with a white filled circle that represents the N_ALC_YJH_S coronagraph with a radius of $\sim$0$\farcs$12, or $\sim$8.6 au at 71.48 pc. *Bottom left panel:* synthetic image at 1.3 mm convolved with the uvmem beam. *Bottom right panel:* synthetic image at 1.65 μm. For all the images in the figure the colour scale is linear, and the colour bar on the left applies only to the images on the left-hand panel.

## 2.3.2. VLT/SPHERE–IRDIS

V4046 Sgr was observed in DPI mode with SPHERE–IRDIS on March 13, 2016 (see Avenhaus et al., 2018, for details). Here we use a new reduction of the *H* band data produced with the IRDAP pipeline (van Holstein et al., 2020), which can separate stellar and instrumen-

tal polarisation. The polarised signal is consistent with the previous image in Avenhaus et al. (2018). The degree of linear polarisation of the central and unresolved signal in V4046 Sgr is only 0.13 %, with a systematic uncertainty of 0.05 % due to time-varying atmospheric conditions during the exposures. The angle of polarisation is aligned with the disc major axis, as expected given that the target has an extinction of Av=0.0 (McJunkin et al., 2016) and the entire polarisation is dominated by circumstellar rather than inter-stellar material.
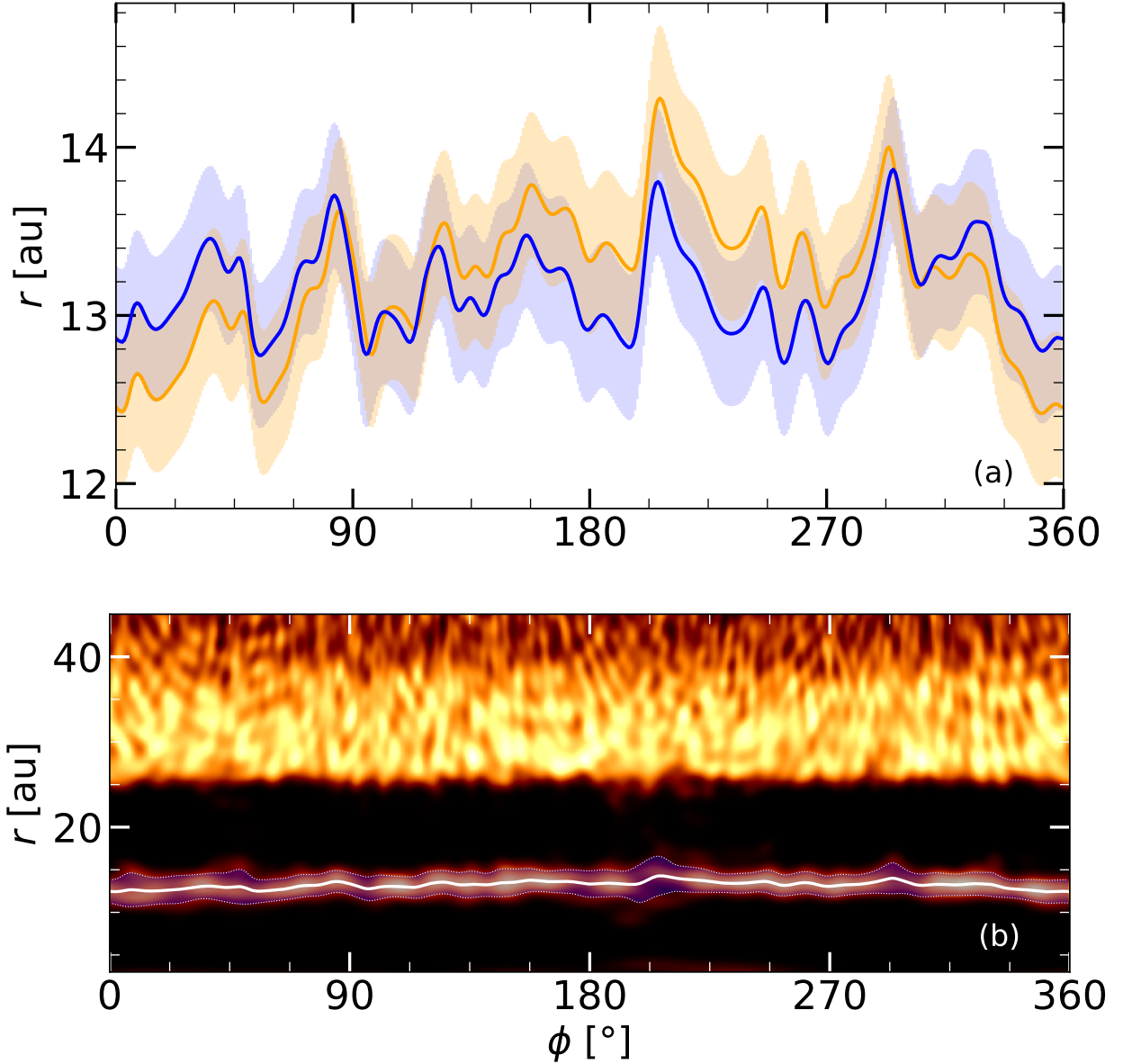


Figure 2.2: **(a)** Centroid of Ring13, for two disc orientations: the orange line corresponds to the same trace as in (b), while the blue line is obtained for the inner ring orientation. **(b)** Polar decomposition of the 1.3 mm continuum image, using the orientation of Ring24. We trace Ring13 using the centroids (solid line) and FWHM of radial Gaussian fits (blue region between the dotted lines).

The scattered light image in the top left panel of Fig. 2.1 also shows a double ring struc-

ture in the micron-sized dust distribution. The observed morphology presents an inner cavity of ∼10 au in radius and two rings located at 14.10±0.01 au, coincident with Ring13, and 24.62±0.08 au, coincident with the inner wall of Ring24, with a small gap between them at ∼20 au (Ruíz-Rodríguez et al., 2019). Two other important features that are present in the image are: the near-far brightness asymmetry, and the shadows projected on the disc by the close binary system as they eclipse each other, discovered by D'Orazi et al. (2019).

The binary phase reported by D'Orazi et al. (2019) in the scattered light observation is at a PA of 265 deg, east of north. Using this measurement, the binary phase was calculated at the time of the ALMA observation at a PA of ∼80 deg.
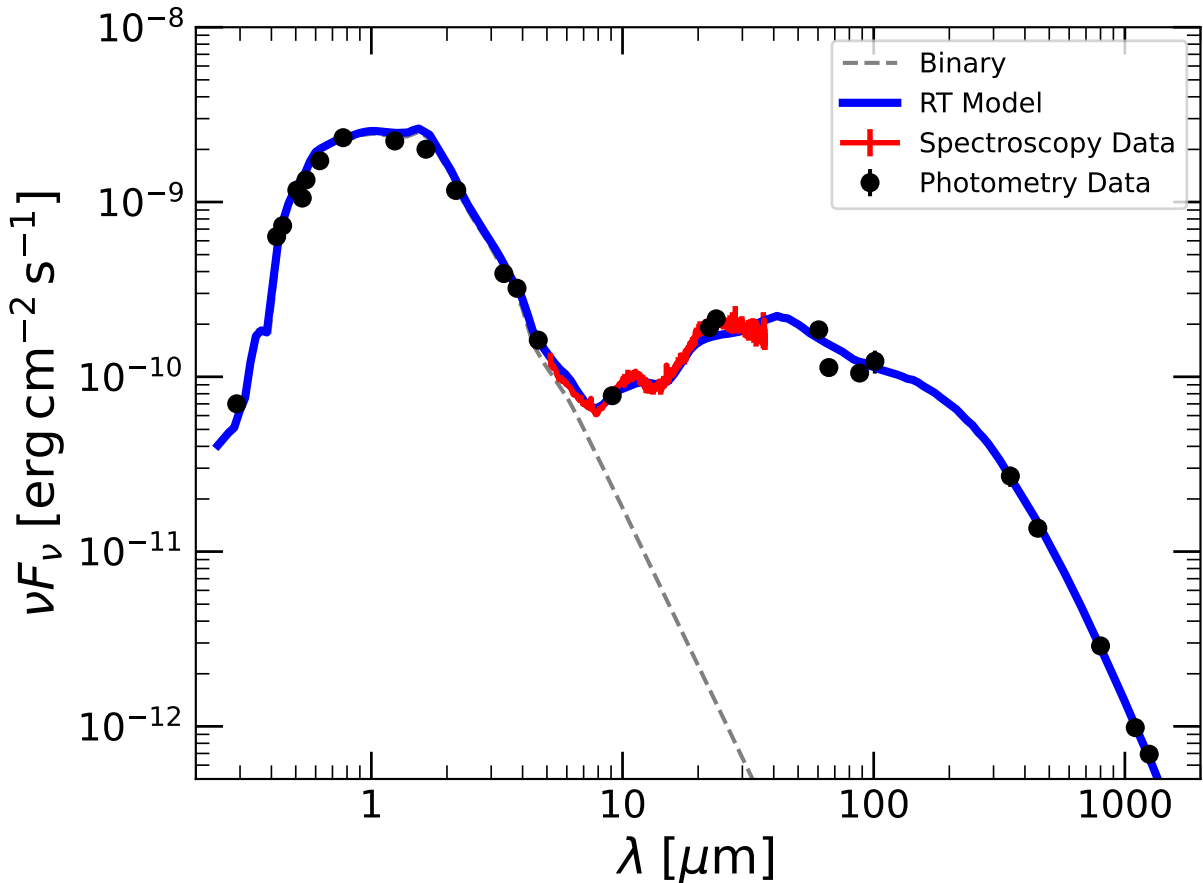


Figure 2.3: The observed SED of V4046 Sgr (black points and solid red curve) compared with the model SED resulting from the RT model (solid blue line). The black points represent the measured photometry and the red line shows an archival *Spitzer* IRS spectrum. The dashed silver curve shows the emission of the stellar photosphere model.

## 2.3.3. Spectral energy distribution

The observed SED was collected from data in the literature (Helou and Walker, 1988; Hutchinson et al., 1990; Jensen and Mathieu, 1997; Hog et al., 2000; Kharchenko, 2001; Cutri et al., 2003; Murakami et al., 2007; Ofek, 2008; Ishihara et al., 2010; Cutri and et

al., 2012), available online in VIZIER. We also used archival *Spitzer* IRS spectroscopic data available in the CASSIS database (Lebouteiller et al., 2015). The data is displayed in Fig. 2.3 along with the resulting SED of the radiative transfer model presented in the next section (more on the resulting SED in Sec. 2.5). The SED exhibits the dip near $10\,\mu$m characteristic of transition discs, as described by Rosenfeld et al. (2013). Jensen and Mathieu (1997) concluded that these data matched that of a extended circumbinary disc truncated at $\sim0.2$ au, as the interior would also be expected to be cleared by dynamical effects of the central binary (Artymowicz and Lubow, 1994).

## 2.4.  Parametric radiative transfer model

The multi-frequency data can be interpreted in terms of a physical structure using radiative transfer predictions, for which we used the RADMC3D package (version 2.0, Dullemond et al., 2012). The general framework of the parametric model that we developed is similar to that in Casassus et al. (2018) for DoAr 44, and the initial model values were inspired from those in Rosenfeld et al. (2013), Ruíz-Rodríguez et al. (2019) and Qi et al. (2019). A high-resolution radiative transfer model that reproduces multi-frequency imaging and the SED, is a solution to a highly degenerate problem, so a full parameter exploration requires a level of computation and time that exceeds our capabilities and the scope of this paper. Consequently, our approach was to find through trial and error a set of values for the parameters that closely fit the available data, and then, improve this fit by implementing one dimensional least squared optimisations for some key parameters (more on this in Sec. 2.5). The final structure of the parametric model is summarised in Fig. 2.4, where we show on the top panel the surface density profiles for gas and dust grains populations, and in the lower panel the respective aspect ratio profile.

### 2.4.1.  General setup

The stars were modelled using two Kurucz photosphere models (Kurucz, 1979; Castelli et al., 1997), with $T_{eff,1} = 4350$ K, $R_{*,1} = 1.064\,R_{\odot}$, $M_{*,1} = 0.90\,M_{\odot}$ and $T_{eff,2} = 4060$ K, $R_{*,2} = 1.033\,R_{\odot}$, $M_{*,2} = 0.85\,M_{\odot}$, respectively and with an accretion rate of $\log(\dot{M}/(M_{\odot}\,\mathrm{yr}^{-1})) = -9.3$ for both cases to include excess UV due to stellar accretion (Donati et al., 2011). The stars were placed at a mutual separation of 0.041 au, so that their centre of mass coincides with the origin. Their PA was set to 250 deg, so that the secondary lies to the NW from the primary, thus casting the same shadow as observed by D'Orazi et al. (2019).

Reproducing the radial and vertical structure of the V4046 Sgr disc turned out to be challenging. We built the model in terms of the gas distribution, and with two main dust populations: large grains with radii from $0.3\,\mu$m to 10 mm that are vertically settled and dominate the total dust mass, and a population of smaller grains with radii ranging from 0.3 to $1.5\,\mu$m that are uniformly mixed with the gas and reach higher regions above the mid-plane.

We take a three dimensional model in a cylindrical reference frame with coordinates ($r$, $\theta$, $z$). The inner radius of the model grid was set to 0.1 au, and the outer radius to 100 au, which is large enough for the dust disc to be undetectable. We set the values of the inclination and disc position angle to the same as obtained from the ALMA observation in Section 2.3, such

that the model has an inclination of i $= 147.04\,$deg and a P.A. $= 257.31\,$deg. The model was set at a distance of d $= 71.48\,$pc (Gaia Collaboration et al., 2021).

## 2.4.2. Radial structure: gas & small dust grains

Given the cylindrical coordinates $(r, \theta, z)$, the gas density $(\rho_{\mathrm{gas}})$ distribution follows

$$\rho_{\mathrm{gas}}(r, z) = \frac{\Sigma_{\mathrm{gas}}(r)}{\sqrt{2\pi}\, H(r)} \exp\left[-\frac{1}{2}\left(\frac{z}{H(r)}\right)^2\right], \tag{2.3}$$

where $H(r)$ is the scale height profile and $\Sigma_{\mathrm{gas}}(r)$ is the gas surface density profile.

Although both ALMA and SPHERE–IRDIS images display two-ringed morphologies, we propose a three-ringed structure plus an inner disc to reproduce the observations. This bold decision is due the major fit improvement in the SED and the polarize image (more on this in Sec. 2.5 and Appendix A.1.2). We separate the gas disc into four individual regions: an inner disc with a power-law profile and three rings named Ring5, Ring13, and Ring24, as they are located at 5, 13, and 24 au respectively. The combined gas surface density profile is then given by:

$$\Sigma_{\mathrm{gas}}(r) = \Sigma_{\mathrm{inner\,disc}}(r) + \Sigma_{\mathrm{R5}}(r) + \Sigma_{\mathrm{R13}}(r) + \Sigma_{\mathrm{R24}}(r). \tag{2.4}$$

First, the inner disc model follows a power-law function defined by

$$\Sigma_{\mathrm{inner\,disc}}(r) = \Sigma_{\mathrm{c}}\left(\frac{r}{R_{\mathrm{c}}}\right)^{-\gamma}\exp\left[-\left(\frac{r}{R_{\mathrm{c}}}\right)^{2-\gamma}\right], \tag{2.5}$$

where $R_c$ is a characteristic radius and $\gamma$ is the surface density power-law index. We used $R_c = 16\,$au, $\Sigma_{\mathrm{c}} = 1.3 \times 10^{-4}\,\mathrm{g\,cm}^{-3}$ and a fixed $\gamma = 1$ as it is a typical value for discs (Andrews et al., 2009, 2010). The gas in our model extends from $R_{\mathrm{in}} = 0.2\,$au outwards, consistent with the inner edge radius inferred from the SED data (see Appendix A.1.2).

Secondly, due to the thin nature of Ring5 and Ring13, we chose to use Gaussian profiles to parametrize them,

$$\Sigma_{\mathrm{ring}}(r) = \frac{\Sigma_{\mathrm{o}}}{\sqrt{2\pi}\sigma}\exp\left[-\frac{1}{2}\left(\frac{r-\mu}{\sigma}\right)^2\right], \tag{2.6}$$

where we define constants that correspond to the centroid radii $\{\mu_{\mathrm{R5}} = 5.2\,$au, $\mu_{\mathrm{R13}} = 14.9\,$au$\}$, ring widths $\{\sigma_{\mathrm{R5}} = 0.25\,$au, $\sigma_{\mathrm{R13}} = 2.26\,$au$\}$, and normalizations $\{\Sigma_{\mathrm{o,R5}} = 3.3\,\mathrm{g\,cm}^{-3}$, $\Sigma_{\mathrm{o,R13}} = 6.0 \times 10^{-1}\,\mathrm{g\,cm}^{-3}\}$ for both components separately.

Thirdly, for Ring24 we used the same power-law as for the inner disc but scaled by an empirically obtained factor, $\delta_{\mathrm{sd}}(r)$ and by $\epsilon(r)$, a parameter that allows us model a smoother inner edge of the outer ring:

$$\Sigma_{\mathrm{R24}}(r) = \Sigma_{\mathrm{inner\,disc}}(r)\,\delta_{\mathrm{sd}}(r)\,\epsilon(r), \tag{2.7}$$

with $\delta_{\mathrm{sd}}(r) = 1.0 \times 10^5$ for $r > 18\,\mathrm{au}$ and zero for lower radii, and

$$\epsilon(r) = \begin{cases} 1 & r < R_{\mathrm{in}} \text{ and } R_{\mathrm{peak}} < r \\ \left( \frac{r - R_{\mathrm{in}}}{R_{\mathrm{peak}} - R_{\mathrm{in}}} \right)^3 & R_{\mathrm{in}} < r < R_{\mathrm{peak}}, \end{cases} \tag{2.8}$$

where $R_{\mathrm{in}}$ and $R_{\mathrm{peak}}$ respectively mark the inner edge and the location of maximum density of the outer ring. We used $R_{\mathrm{in,gas}} = 18\,\mathrm{au}$ and $R_{\mathrm{peak,gas}} = 26.4\,\mathrm{au}$.

Finally, the total dust-to-gas mass ratio is taken to be $\zeta = 0.047$ (as in Rosenfeld et al., 2013). The small dust grains are assumed to only make up for a fraction of $f_{\mathrm{sd}} = 1\,\%$ of the total dust mass. As small dust is typically tightly coupled to the gas dynamics, its density profile is expected to follow the gas density. Then the density of small dust can be calculated as:

$$\rho_{\mathrm{smalldust}}(r, z) = \rho_{\mathrm{gas}}(r, z)\, f_{\mathrm{sd}}\, \zeta. \tag{2.9}$$

### 2.4.3. Radial structure: large dust grains

Since the large dust grains are less coupled to the gas, their distribution has some important differences that require a special parameterisation, such as a larger inner cavity, a larger gap between Ring13 and Ring24, and a break in the outer ring. We only included a low density of large grains within Ring5, just underneath the detection limit of the ALMA observation, as it does not show any visible signature. The surface density profile of the large dust grains is then defined by the sum of its three components

$$\Sigma_{\mathrm{ld}}(r) = \Sigma_{\mathrm{R5,ld}} + \Sigma_{\mathrm{R13,ld}} + \Sigma_{\mathrm{R24,ld}}. \tag{2.10}$$

For Ring5 and Ring13, we chose Gaussian profiles parameterized with centroid radii $\mu_{\mathrm{R5,ld}} = 5.2\,\mathrm{au}$ and $\mu_{\mathrm{R13,ld}} = 13.22\,\mathrm{au}$, ring widths of $\sigma_{\mathrm{R5,ld}} = 0.1\,\mathrm{au}$ and $\sigma_{\mathrm{R13,ld}} = 0.85\,\mathrm{au}$, and normalizations $\Sigma_{\mathrm{o,R5,ld}} = 1.3 \times 10^{-4}\,\mathrm{g\,cm^{-3}}$ and $\Sigma_{\mathrm{o,R13,ld}} = 2.3\,\mathrm{g\,cm^{-3}}$. For Ring24 we used a similar profile as for the gas (a power-law function). The surface density for large dust grains in the outer ring is thus given by

$$\Sigma_{\mathrm{R24,ld}}(r) = \Sigma_{\mathrm{c}} \left( \frac{r}{R_{\mathrm{c}}(r)} \right)^{-\gamma_{\mathrm{ld}}} \exp\left[ -\left( \frac{r}{R_{\mathrm{c}}(r)} \right)^{2-\gamma_{\mathrm{ld}}} \right] \delta_{\mathrm{ld}}(r)\, \epsilon(r), \tag{2.11}$$

where for the smoothing factor $\epsilon(r)$ we used $R_{\mathrm{in,ld}} = 24.2\,\mathrm{au}$ and $R_{\mathrm{peak,ld}} = R_{\mathrm{peak,gas}}$, resulting in an inner wall of Ring24 at larger radii for the large dust but a peak at the same location than that of the small dust. In an effort to recreate the break seen in the outer ring, we used

$$\delta_{\mathrm{ld}}(r) = \begin{cases} 0 & r < 24.6\,\mathrm{au} \\ 1.8 \times 10^5 & 24.6 < r < 27.9\,\mathrm{au} \\ 8.4 \times 10^4 & 27.9 < r < 35.3\,\mathrm{au} \\ 7.1 \times 10^5 & 35.3 < r < 64\,\mathrm{au}, \end{cases} \tag{2.12}$$

and

$$\gamma_{\mathrm{ld}}(r) = \begin{cases} -3.8 & 27.9\,\mathrm{au} < r < 35.3\,\mathrm{au} \\ 1 & \text{elsewhere.} \end{cases} \tag{2.13}$$

Then the final density of large dust can be calculated as

$$\rho_{\text{large dust}}(r, z) = \frac{\Sigma_{\text{ld}}(r)}{\sqrt{2\pi}\,H(r)}\exp\left[-\frac{1}{2}\left(\frac{z}{H(r)}\right)^2\right]f_{\text{ld}}\,\zeta. \tag{2.14}$$

Following the observation, this profile is truncated at $63\,\text{au}$.

### 2.4.3.1. Reproducing the central emission

For whole purpose of reproducing the central emission in the ALMA image, we introduce a third and special dust population of larger grains with a distribution tightly confined to the stellar vicinity. This dust is distributed only on a very close-in Gaussian ring parameterized by $\mu_{\text{central blob}} = 1.1\,\text{au}$, $\sigma_{\text{central blob}} = 0.4\,\text{au}$ and $\Sigma_{\text{o,central blob}} = 58.8\,\text{g cm}^{-3}$, and it is composed of grains with radii ranging from 0.8 to 10 mm, same upper limit as the large dust but is depleted of small grains. With this distinctive size range we avoid creating a NIR excess in the SED, and we can be consistent with previous mass estimates (see Appendix A.1.1 and Sec. 2.5).

## 2.4.4. Vertical structure

The parametric scale height profiles for the gas and for each dust population are

$$H(r) = \chi\,H_{\text{o}}\left(\frac{r}{r_{\text{o}}}\right)^{1+\psi(r)}, \tag{2.15}$$

where $H_{\text{o}}$ is the scale height at $r = r_{\text{o}}$, $\psi$ is the flaring index and $\chi$ is a scaling factor (in the range $0-1$) that mimics dust settling. In hydrostatical equilibrium, dust diffusion and settling are expected to balance each other, leading to a settling factor of $\chi = \sqrt{D_{\text{d}}/(D_{\text{d}} + St)}$ (Dubrulle et al., 1995). Here, $D_{\text{d}}$ is a dimensionless parameter that informs about the level of diffusivity (it is typically assumed to be similar to the level of turbulence for the particle sizes regarded here Youdin and Lithwick, 2007). The Stokes number,

$$St = \frac{1}{2}\frac{\pi a \rho_{\text{mat}}}{\Sigma_{\text{gas}}}, \tag{2.16}$$

summarises the dynamical behaviour of a particle in a given environment (where $\rho_{\text{mat}}$ represents a dust particle's material density). By definition, the gas has no settling, and the small dust grains settling is negligible, so that $\chi_{\text{gas}} = \chi_{\text{sd}} = 1$. As we do not know the level of diffusivity in the disc (this will be a topic of interest in Section 2.5), nor the exact value of $\Sigma_{\text{gas}}$, we infer the scaling factor for large dust, $\chi_{\text{ld}}$, from the width of Ring13. In the radial profile this ring is observed two to three times wider in the gas-tracing NIR than in the fluxes received from larger grains by ALMA. We assume that the same ratio holds in the vertical direction (due to the settling of larger grains towards the mid-plane of the disc), leading to $\chi_{\text{ld}} = 0.4$. This is analogous to assuming equal radial and vertical turbulent diffusions.

For the vertical structure, D'Orazi et al. (2019) found flaring angles (i.e. height of the ring over the disc midplane divided by the radius of the ring), of $\varphi = 6.2\pm0.6\,\text{deg}$ for the inner ring and $\varphi = 8.5\pm1.0\,\text{deg}$ for the outer one. Our model aims to reproduce those values by

using two different flaring indices, $\psi_1$ and $\psi_2$. The separation between the two values was set at $r = 18\,\mathrm{au}$ with $\psi_1 = 0.2$ for Ring5 and Ring13, and $\psi_2 = 0.5$ for Ring24. The scale height is set to $H_\circ = 0.89\,\mathrm{au}$ at $r_\circ = 18\,\mathrm{au}$. This vertical structure is consistent with the measurements made by D'Orazi et al. (2019), as the model flaring angles are $\varphi_{\mathrm{inner}} = 6.4\,\mathrm{deg}$ and $\varphi_{\mathrm{outer}} = 7.6\,\mathrm{deg}$. This is summarised in the bottom panel of Fig. 2.4 that shows the aspect ratio profile $h(r) = H(r)/r$.
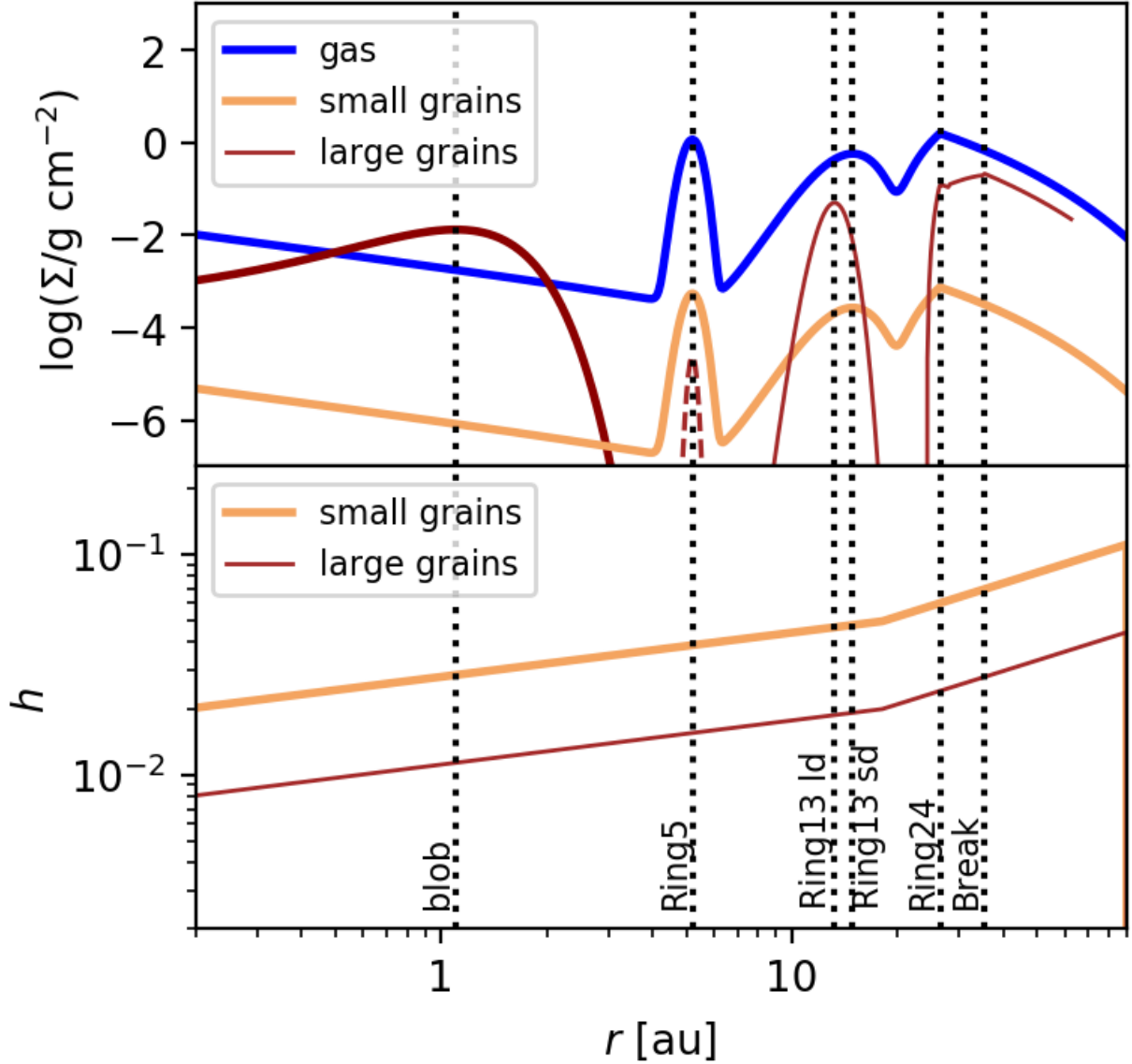


Figure 2.4: **Top:** surface density profiles for gas, large and small dust grains. **Bottom:** Aspect ratio profile $h(r) = H(r)/r$. The dashed brown line depicts an upper limit for large dust grains within Ring5, inferred from its non-detection in ALMA data. The dotted lines crossing both panels correspond to transition radii in the parametric model.

### 2.4.5. Image synthesis and SED computation

To take the simulated images we computed the dust opacities using the `bhmie` code provided in the RADMC3D package. The two main populations are taken to be composed by a mix of 60 % silicate, 20 % graphite and 20 % ice. Differently, for the special population of larger grains, as the ring is extremely proximate to the binary system, the dust will not have any traces of ice, so we used a composition mix of 70 % silicate and 30 % graphite.

For the reproduction of the ALMA observation, we create an image using ray-tracing preceded by a Monte Carlo run that gives the simulated image at 1250 μm, the rest wavelength of the real observation. This image is then convolved with Gaussian blur using the uvmem beam of $0''021 \times 0''018$ to synthesise the final image displayed in Fig. 2.1. The SED is computed in a similar manner by taking the spectra at 200 wavelengths between 0.1 and 2000 μm.

In order to reproduce the *H*-band image, we take a different approach. As the observed asymmetry between the near side and the far side of the disc in the DPI image is suggestive of a strongly forward-scattering phase function, we used much larger grains than typically used in the RT modelling of such NIR data (e.g., Casassus et al., 2018). For the computation of this particular image, we implemented a different grain size distribution, where we centred a Gaussian at a $= 0.4$ μm with $\sigma_a = 0.12$ μm (smeared out by 30 %), and distributed the dust over 20 bins within the range of $\pm\sigma$. This distribution applies only to generate the NIR $Q_\phi$ image and not the ALMA image or the SED. To produce this $Q_\phi$ image we performed a linear combination of the two orthogonal linear polarisation $U$ and $Q$, following Avenhaus et al. (2017), which gives a representation of an unbiased estimate of the polarised intensity image. The simulated DPI image at 1.65 μm in Fig. 2.1 was obtained with the scattering matrix calculated by the `makeopac.py`, script provided in the RADMC3D package.

Finally, as mentioned before, the model presented here gives a solution to a highly degenerative problem, and the RT calculation for each set of parameters is very intensive in computational power and time, so a MCMC optimisation or similar methods of parameter exploration are impossible to carry out. Nevertheless, as a way to improve the fit and obtain a rough measure of the accuracy of our model, we made one dimensional explorations of the parameter space and found uncertainties of some relevant parameters that will be useful for the discussion (see Appendix A.1.1). We can estimate uncertainties for the scale height at $r_\circ = 18$ au with $H_\circ = 0.89 \pm 0.01$ au and for the width of the gas in Ring13 with $w_g = 5.30 \pm 0.27$ au.

## 2.5. Model results and discussion

The observed SED reveals a small near-infrared (NIR) excess of 0.9±3.7 % (Francis and van der Marel, 2020), this low emission would be primarily emanating from micron-sized dust grains at the hot inner dust wall of a low-mass inner disc. On the other hand, the mm-bright central emission suggests a massive inner dust ring. The faint near-IR excess contrast with the bright mm emission, and could point to a lack of micron-sized dust in the central ring, that could be due to efficient dust growth or due to the ring having an inner radius well beyond the sublimation radius. In order to reproduce the low NIR and simultaneous bright central mm emission, we extended the radius of an inner cavity to significantly exceed both

the sublimation radius and the zone that is expected to be cleared by dynamical binary-disc interaction (see Appendix A.1.2). A possible explanation for this wider cavity is the presence of an additional effect of truncation, like an unseen companion planet in the very inner part of the disc (Francis and van der Marel, 2020). At the same time, the central emission is also well reproduced in the ALMA image with the inclusion of a Gaussian ring at 1.1 au. This inner ring produces a low near-IR excess only if it consists of dust grains larger than $\sim$0.3 mm (see Appendix. A.1.1). But we implement 0.8 mm instead as the lower limit for the dust population that composes this feature, given that this predicts a dust mass of 0.012 $M_{\oplus}$, which is close to that obtained by Francis and van der Marel (2020) (0.013±0.002,M$\oplus$). They converted mm-flux into mass using the standard opacity value of $\kappa_{\nu}$=10 cm$^2$g$^{-1}$ at 1000 GHz with an opacity power-law index of $\beta$=1.0, while our mass estimates are extracted from the RT model.
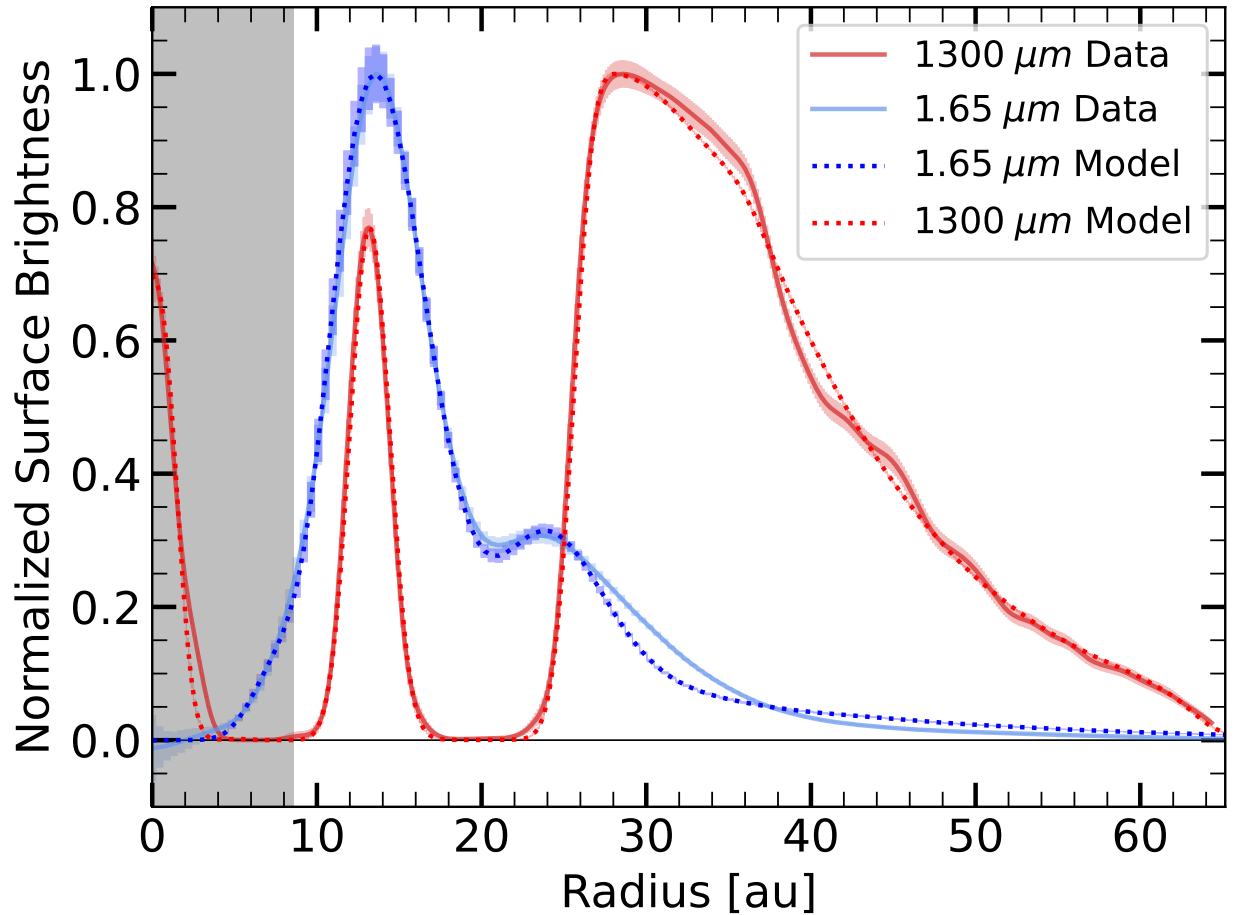


Figure 2.5: Comparison of the surface brightness profiles extracted from the deprojected synthetic images and observed $H$-band and 1.3 mm continuum images. The grey shaded area represents the radius of the artificial coronagraph used in the simulations (i.e., $\sim$0$\farcs$1, or $\sim$7.1 au at 71.48 pc).

The decision of including Ring5 to the observed structure relies on the fact that the SED needs a thin dust ring, made mainly of small dust grains, at a radius of $\sim$5 au to have a proper fit between 6 and 300 $\mu$m (see Appendix A.1.2). The introduced Ring5 is not visible in the simulated image at 1.65 $\mu$m, where it hides under the artificial coronagraph, neither in

the 1.3 mm continuum simulated image, as its predicted peak intensity is around two times the noise in the ALMA image ($\sim 1 \times 10^{-7}\,\mathrm{Jy\,beam}^{-1}$). This gives us an upper limit for the total millimetre–sized dust mass present in Ring5 of $\sim 2 \times 10^{-5}\,\mathrm{M}_{\oplus}$. The depletion of large dust grains in Ring5 is consistent with efficient dust trapping in Ring13. A zone of radially increasing gas pressure can entirely filter out large dust grains from the inner regions, while smaller grains can be able to overcome this barrier due to their strong frictional coupling to the gas accretion flow (studied in the context of planetary gaps, Rice et al., 2006; Zhu et al., 2012; Weber et al., 2018). Still, the strong depletion of large particles demands that within Ring5 dust growth is extremely inefficient or limited by fragmentation. Otherwise, the present small grains should coagulate to form detectable grain sizes in the ALMA observation in Fig. 2.1 (Drazkowska et al., 2019).

As the radial profiles obtained from the simulated images of the model closely resemble those deduced from the observations (Fig. 2.5), we can assume that the model provides a possible approximation of the disc structure, including the dimensions of Ring13. The FWHM of the gas and micron-sized dust in Ring13 in the RT model corresponds to $w_{\mathrm{g}} = 5.30 \pm 0.27\,\mathrm{au}$, as well as a radius of 14.9 au, and a scale height FWHM of 0.63 au. Meanwhile, the millimetre-sized dust in Ring13 has a FWHM of 2.00 au, a radius of 13.22 au, and a scale height FWHM of 0.25 au ($\sim 2.355 \times H(\mu_{\mathrm{R13,ld}})$). The total dust mass of Ring13 would be about $0.7\,\mathrm{M}_{\oplus}$. The model predictions for the millimetre-sized dust population in Ring13 are close to the measurements, with only a 1 % difference in the centroid location of the ring, and a 19 % difference in the width estimation. Given that the scale height FWHM of the large grains in Ring13 is 0.25 au, and that the width of Ring13 from the ALMA observations is $2.46 \pm 0.56$ au (see Sec. 2.3.1), we conclude that the large dust ring is $10.0 \pm 1.6$ times more extended radially than vertically. Looking at the rest of the disc, our model reproduces the observations of Ring24 with peak intensity at $\sim 30$ au, and the break at $\sim 36$ au. The whole disc contains a total dust mass of $\sim 48\,\mathrm{M}_{\oplus}$.

Even though the radial spread of large dust grains in Ring13 appears to be quite thin, the width in comparison to the sub-lying gas profile speaks for the presence of considerable turbulent diffusion. Following a similar ring analysis as in Dullemond et al. (2018), we find that the ratio between the dimensionless diffusion parameter, $D_{\mathrm{d}}$, and the dimensionless Stokes number, St, (which parameterise the dynamical behaviour of a grain) is roughly, $D_{\mathrm{d}}/\mathrm{St} \approx 0.1$. The observed signal is expected to be dominated by grains of size $a \approx 0.02$ cm. The RT model, together with the dust-to-gas ratio of 0.05, prescribe a gas density of $\Sigma_{\mathrm{g}} \approx 0.5\,\mathrm{g\,cm}^{-2}$ to the location of Ring13. With these values, the relevant Stokes number is approximated to be St$\approx 0.1$. This yields an estimate for the level of diffusivity of $D_{\mathrm{d}} \approx 0.01$. It further provides a value for the level of turbulent viscosity in Ring13, $\alpha_{\mathrm{turb}} \approx 0.01$, assuming the level of turbulence to be equal to the level of diffusion (Youdin and Lithwick, 2007). We note that an observation of molecular line broadening has found no evidence for turbulent contributions, suggesting $\alpha_{\mathrm{turb}} < 0.01$ (Flaherty et al., 2020). The value inferred from our model is just within this limit. By our definition of the gas surface density profile, the value inferred for the level of turbulence is linearly proportional to the local dust-to-gas ratio. Lower values than the chosen ratio of 0.05 would, therefore, lead to an equally lower level of turbulence in the assessment. While the exact value for $\alpha_{\mathrm{turb}}$ is not well constrained, a certain level of turbulence is required to explain the radial spread of the resolved Ring13.

The visible asymmetry in the SPHERE observations is reproduced using relatively large grains, $\sim$0.4 μm, as smaller grains did not result in such strong forward scattering. As Stolker, T. et al. (2016) state, the strong forward scattering that is present in the observation may indicate that the dust grains in the disc surface are relatively large, suggesting that the disc is depleted of very small grains. Alternatively, it may suggest that grains are not spherical as assumed in the calculations of opacities using Mie theory.

Another interesting feature of the simulated 1.65 μm image is that the model accurately shows the shadows described by D'Orazi et al. (2019) that are present in the SPHERE–IRDIS image. In contrast, there are no hints of radio decrements along Ring13 or in Ring24, in either the ALMA observations or in the simulated 1.3 mm continuum image, that would match the shadows. As noted by Casassus et al. (2019b), the diffusion of thermal radiation from the disc smooths out the decrements seen in scattered light, and in this case it is likely that the disc cooling time-scale is much slower than the that of the illumination pattern.

The general observed structure may point to the existence of planet-disc interactions within this system, where giant planets deplete their orbits of gas and dust material. A possible planetary constellation in this scenario is, therefore, the presence of two giant planets in the disc, one planet between the star and Ring13, and one planet between Ring13 and Ring24. As Ruíz-Rodríguez et al. (2019) suggest, the putative planet between Ring13 and Ring24 may be a giant planet with a mass within the range of $0.3-1.5\,\mathrm{M_{Jup}}$. This idea is supported by a dedicated study (Weber et al. submitted) which qualitatively reproduces the observations of this system with a hydrodynamical simulation including several giant planets.

The expected age of $>$20 Myr of V4046 Sgr suggests that its gas-rich disc is unconventionally old in comparison to typical circumstellar examples (e.g. Fedele et al., 2010; Williams and Cieza, 2011). The dispersal of such gas discs is typically assumed to be set by photo-evaporation (Alexander et al., 2006; Gorti and Hollenbach, 2009). While the dynamical origin of the disc's longevity is not the subject of the present study, we would like to mention that its occurrence around such a close binary might not be coincidental. Alexander (2012) predicted that disc lifetimes should show a sharp increase around binaries separated by $\lesssim 0.3-1.0$ au. It still has to be seen whether a trend towards longer disc lifetimes in compact multiple-star systems (as recently proposed by Ronco et al., 2021) turns out to be prevalent.

## 2.6. Conclusions

We present new ALMA 1.3 mm continuum imaging of V4046 Sgr, a well-known circumbinary disc, at an unprecedented definition ($\sim$0″021 × $\sim$0″018), where new features become visible. Together with the analysis of a SPHERE–IRDIS polarised image and a well-sampled SED, we aim to reproduce the observations with radiative transfer modelling, looking for a way to explain the data in terms of a physically model. The key conclusions of this analysis are as follows.

1. The central emission in the ALMA image suggests the existence of an inner ring of dust grains larger than 0.8 mm. Our interpretation agrees with the mass estimation of this feature made by Francis and van der Marel (2020), with a mass of $0.012\,\mathrm{M_{\oplus}}$.

2. Our parametric model, which accounts for the SED of the system, predicts the presence

of an inner ring at $\sim$5 au, mainly consisting of small dust grains. This additional ring lies under the coronagraph of the scattered light image and is too faint to be detected by the ALMA observation. The depletion of large dust in this ring is consistent with efficient dust trapping at larger radii, as can be expected in Ring13.

3. The narrow ring in the 1.3 mm continuum, has a radius of 13.15$\pm$0.42 au and an estimated width of 2.46$\pm$0.56 au. The location of this ring is coincident with the inner ring observed in the scattered light image. From our RT modelling we can predict that this ring includes around 0.7 M$_\oplus$ of millimetre-sized grains. Using the parametric model scale height FWHM value for the large grains ($H_{\mathrm{ld}} = 0.25$ au at 13.15 au) we find that the ring width is roughly 10 times its estimated height.

4. The 1.3 mm outer ring, that starts at $\sim$24 au and has its peak intensity at $\sim$30 au, presents a visible break in the surface brightness at $\sim$36 au.

5. While we can not get an exact value for $\alpha_{\mathrm{turb}}$, the resolved radial width of Ring13 speaks for the presence of a considerable level of turbulent viscosity.

6. We interpret the asymmetry observed with SPHERE–IRDIS at 1.65 μm as due to strong forward-scattering, which implies that the dust population is depleted of grains smaller than $\sim$0.4 μm.

# Acknowledgements

# Data Availability

The data used in this article are presented in Fig. 2.1. The final images can be found in FITS format in supplementary materials while the original raw data can be downloaded directly from the ALMA archive using project code 2017.1.01167.S. The SPHERE/IRDIS data can be downloaded from the ESO archive using project code 096.C-0523(A).

# Capítulo 3

# ISO-Oph 2: a case study for external radiation?

Evolved discs usually show beautiful arrangements of rings and gaps in the continuum, generally quite axisymmetric features, and it is common to attribute them to planet-disc interaction or, to a lesser extent, to other internal processes (e.g. radial drift, dust traps, warp discs; see Marino et al. (2015) for the study on warp discs). However, because most stars originate in star clusters (e.g. Lada and Lada, 2003; Krumholz et al., 2019), the environmental effects must be considered to understand young planetary systems adequately (Haworth, 2021). Accordingly, the two main ways the surroundings can impact a system are through dynamic effects and photoevaporation. The first refers to close encounters between neighbour stars, where the gravitational interaction affects the disc's dynamics. The latter refers to how the temperature field of a disc is influenced by the ambient radiation to which it is exposed, particularly to UV photons and X-rays, which induce photoevaporation. Unfortunately, the observations of such effects on protoplanetary discs are rare, and it is not easy to prove the direct influence only through observations. One reason is, for example, that the 3D distances to neighbouring stars in star-forming regions are generally not well constrained (see e.g. Haworth et al., 2017). Luckily, we can still study these environmental effects using numerical simulations. Here, we will focus on the potential of radiative transfer models for examining the impacts of external radiation on discs.

In this chapter, we will use radiative transfer models to explore a peculiar system, ISO-Oph 2, that shows an asymmetric structure in the continuum that could hint at environmental effects due to external radiation. Thus, in Sec. 3.1, we will explain what is known about the system, give details about previous observations of the source, introduce the puzzling problem, and formulate our hypothesis. Then, in Sec 3.2, we will describe the modelling process. It is relevant to mention that this research project is a work in progress, so in Sec. 3.3, we will discuss the preliminary results of such models and general thoughts on the subject. Then, we finish in Sec. 3.4 with comments on how the project should continue and possible pathways for future developments in this investigation.

## 3.1.   The system in question

ISO-Oph 2 is one of the most attractive sources of the constellation of Ophiuchus. At a distance of $134.25 \pm 7.55$ pc (Gaia Collaboration et al., 2021), it is a binary system with a

projected separation of 240 au and a flux ratio of 0.08 in the $K$-band (Ratzka et al., 2005). The primary star, a Classic T Tauri star with an M0 spectral type and an accretion rate of $10^{-8.7} M_\odot \mathrm{yr}^{-1}$ (Gatti et al., 2006), host a disc with a dust mass of $M_{\mathrm{dust}} \sim 40 M_\oplus$ (Cieza et al., 2019). The secondary star, with no spectral classification available but believed to be close to the brown-dwarf limit, hosts a much lighter disc of $M_{\mathrm{dust}} \sim 0.8 M_{Earth}$ and only $\sim 7$ au across (González-Ruilova et al., 2020).

The system has been observed as a part of the "Ophiuchus Disk Survey Employing ALMA" (ODISEA) project (Cieza et al., 2019), the largest of the disc demography surveys in nearby clouds. Observation of the system of the 1.3 mm continuum and the $^{12}$CO molecular line were taken with ALMA. The high-definition survey accomplished an angular resolution of $0\overset{''}{.}02$ (or $\sim 3$ au at 134.25 pc). Besides that, in the data archives is found an observation in the $K$-band with the now decommissioned VLT instrument Nasmyth Adaptive Optics System (NAOS) – Near-Infrared Imager and Spectrograph (CONICA), better known as NACO. Both images are displayed in 3.1. See González-Ruilova et al. (2020) and Ratzka et al. (2005) for further details on the reduction of the data and instrument information for each observation, respectively.
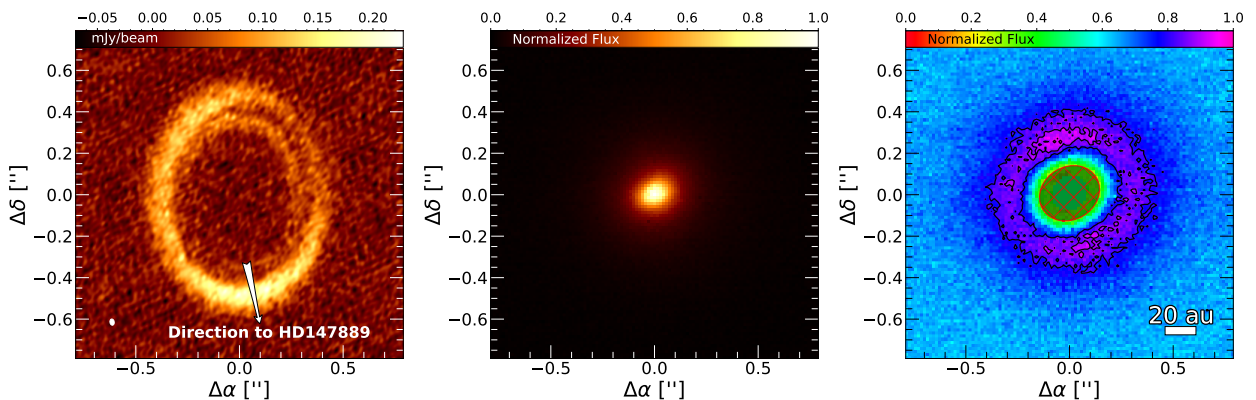


Figure 3.1: **Observations of the disc around ISO-Oph 2 A.** (left) 1.3 mm continuum ALMA observation. The small white ellipse in the bottom right corner shows the beam size ($\sim 0\overset{''}{.}030 \times \sim 0\overset{''}{.}021$). (centre) Archive NACO $K$-band image, 2.2 µm. (right) Altered NACO image. The green filled ellipse represents the subtracted Gaussian. For all the images in the figure the colour scale is linear

The peculiarity of this system resides in that the 1.3 mm continuum observation of the circumstellar disc around the primary star shows a large dust cavity followed by a two-ringed-like disc with spectacular azimuthal asymmetries. After the large inner cavity of $\sim 50$ au in radius, the first ring extends approximately from a radius of 40 to 60 au, while the second one does from a radius of 60 to 85 au. The inner ring peaks to the North-West and becomes practically invisible to the South-East, whereas the outer ring peaks to the South of the star and shows a noticeable decrement to the North-West (González-Ruilova et al., 2020). The disc has an inclination of $i = 36$ deg and PA $= 1$ deg (E of N) (González-Ruilova et al., 2020). In addition, using $^{12}$CO observations, González-Ruilova et al. (2020) found a bridge of gas connecting the primary disc with the disc of the secondary and suggested the possibility

of a recent fly-by that could have dynamically perturbed the disc and induced this strange geometry. However, that interpretation is highly unlikely, as the dynamic effects of fly-bys usually vanish quickly (Marzari and Picogna, 2013). Instead, this asymmetric feature becomes much more interesting once it is considered that the brightest UV source in the region is very close and located in the same direction as the asymmetry, suggesting the possibility of a much more fascinating phenomenon.

Close to ISO-Oph 2,at an angular distance of 0.1 deg and also in the Ophiuchus cloud, located at a distance of 136.35±0.46 pc from Earth (Gaia Collaboration et al., 2021), resides HD 147889, a binary system of two massive pre-main-sequence B2IV and B3IV stars (Houk and Smith-Moore, 1988; Casassus et al., 2008). The two stars are believed to have a $T_{\text{eff}}$ of 20000 and 23000 K and radii of 3.10 and 3.52 $R_\odot$, respectively (Casassus et al., 2008). These characteristics make them the main ionising source in the $\rho$ Oph region. So, as it is known that high external UV radiation causes a rise in dust temperatures in the outer regions of neighbouring discs (Haworth, 2021), it is not so far-fetched to hypothesise that the asymmetry in the continuum comes from exposure to the intense radiation of this source.

Besides the ALMA image, although the data is not exceptionally deep, we have the $K$-band image NACO observation (at 2.2 μm), which maps the distribution of small dust grains on the surface of the disc. Unfortunately, here we have the problem of the star shining too bright at this wavelength, so we must alter the image to dimmer the stellar radiation and allow the ring emission to be seen more clearly. To do this, we can approximate the stellar emission as an elliptic Gaussian and fit it to the image (although it is not the most accurate approximation, the outcomes are reliable.). Accordingly, with this method, we can get the image displayed in 3.1, where we can see an asymmetry that again points toward HD 147889. Hence, the image seems to support our initial suspicions.

To go beyond pure speculation, we can calculate the radiation from HD 147889 over the disc and compare that to the one from the central star. Although the distance between the two systems is not well constrained because of the great uncertainty in the distance measurement of ISO-OPh 2, it can be anywhere from 0.24 to 9.7 pc. Then, we can define three Kurucz photospheres (Kurucz, 1979; Castelli et al., 1997) to model the stars using the following stellar parameters.

| Star name | $T_{\text{eff}}$ [K] | $R_*$ [$R_\odot$] |
|---|---|---|
| ISO-Oph 2 A | 3750 | 0.6 |
| HD 17889 A | 23000 | 3.5 |
| HD 17889 B | 20000 | 3.1 |

Then, with the assumption of no extinction by the interstellar medium, we get Fig. 3.2. This figure displays the radiation over all wavelengths received at 70 au from the star, the same distance as the outer ring. It clearly illustrates how ISO-OPh 2 A dominates the infrared region of the spectrum and how HD 147889 acts as the main UV source of the disc, regardless of distance.
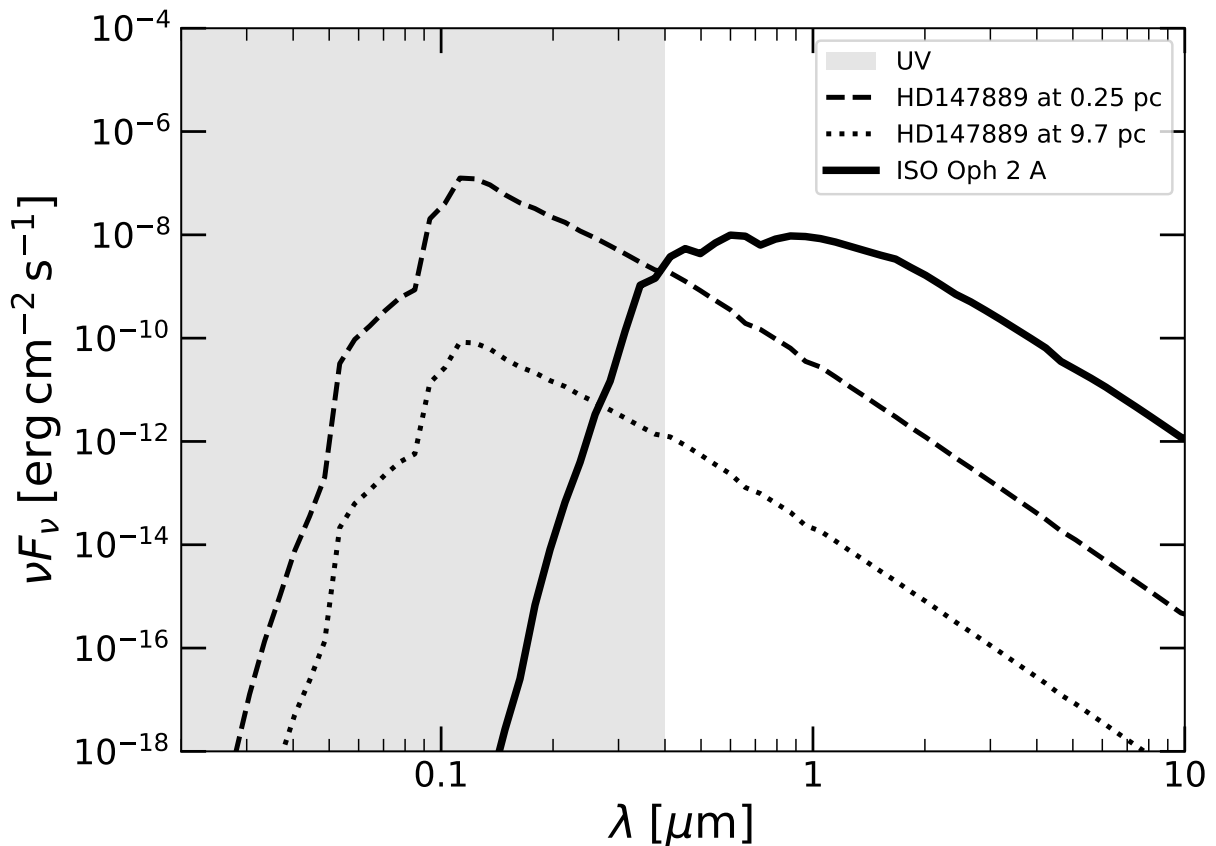
Figure 3.2: The SED from ISO-Oph 2 A as being measured at 70 au (same radius as the outer ring) versus HD 147889 at two different distances: 0.25 and 9.7 pc. And highlighted in grey, the UV part of the spectrum.

## 3.2. Radiative transfer modelling

The general framework of the parametric model we employed is similar to the one used for V4046 Sgr but more refined and efficient. The most significant difference in the methodology would be that now we are not searching for a single configuration that reproduces what we see in the observations exactly, rather than searching if any or multiple configurations could show signs of external radiation in the continuum. So instead of an elaborated model, we have a simpler one that allows better parameter space exploration.

### 3.2.1. General setup

We implemented three stars in the model using point-like black-bodies sources, the primary star at the centre of the grid and the two stars belonging to HD 147889 farther from the disc. It is good to mention that although ISO-Oph 2 B is only at 240 au, it is too cold and too small to affect the primary disc, so it is not even worth modelling it. For the host star, being an M0, we used $T_{\text{eff}} = 3750$ K and radius of $R_* = 0.6\,R_\odot$. For the distant stars, we used $T_{\text{eff}} = 20000$ K and $T_{\text{eff}} = 23000$ K with stellar radii of 3.1 and $3.5\,R_\odot$ respectively. The location of the distant stars is defined in spherical coordinates $(r, \phi, \theta)$ with the origin

at the centre of the disc. The azimuthal orientation $\phi$, the polar angle $\theta$, and the radius $r$ are left as free parameters for further exploration.

Similarly to the last model, it is constructed in terms of gas distribution with two dust populations: large grains with radii from $0.1\,\mu$m to $2\,$mm that are vertically settled and are $99\,\%$ of the total dust mass, and a population of smaller grains with radii ranging from $0.1$ to $1\,\mu$m that are uniformly mixed with the gas and reach higher altitudes above the midplane. The first grain population is composed of a mix of $60\,\%$ silicate, $20\,\%$ graphite and $20\,\%$ ice, whereas the second, as it would be warmer on the disc surface, is composed of a $70\,\%$ silicate and $30\,\%$ graphite mix, so no ice. Both populations have a size distribution $n(a) \propto a^{-3.5}$, where $a$ is the grain radius. Last, the total dust mass is fixed to be $45\,M_\oplus$ with a dust-to-gas mass ratio $\zeta = 0.01$, a standard value for a PPD. Therefore, the total gas mass would be $0.014\,M_\odot$, standing at the low end of the mass range for circumstellar discs around T-Tauri stars (Boss and Ciesla, 2014).

Again, we take a three-dimensional model in a cylindrical reference frame with coordinates $(r, \theta, z)$, where the inner radius of the grid was set to $0.2\,$au and the outer radius to $110\,$au. The structure is simple and follows the same basic equations as the last model. Therefore, the gas density ($\rho_{\mathrm{gas}}$) distribution is:

$$\rho_{\mathrm{gas}}(r, z) = \frac{\Sigma_{\mathrm{gas}}(r)}{\sqrt{2\pi}\, H(r)} \exp\left[-\frac{1}{2}\left(\frac{z}{H(r)}\right)^2\right], \tag{3.1}$$

where $H(r)$ is the scale height profile and $\Sigma_{\mathrm{gas}}(r)$ is the gas surface density profile. $\Sigma_{\mathrm{gas}}(r)$ comprises three elements: a power-law disc and two Gaussian rings,

$$\Sigma_{\mathrm{gas}}(r) = \Sigma_{\mathrm{disc}} + \Sigma_{\mathrm{ring1}} + \delta\,\Sigma_{\mathrm{ring2}}. \tag{3.2}$$

$\Sigma_{\mathrm{disc}}$ is defined as

$$\Sigma_{\mathrm{inner\,disc}}(r) = \left(\frac{r}{R_c}\right)^{-\gamma} \exp\left[-\left(\frac{r}{R_c}\right)^{2-\gamma}\right], \tag{3.3}$$

where $R_c$ is the characteristic radius, and $\gamma$ is the surface density power-law index. $R_c$ was set to $70\,$au and $\gamma = 1$, as this last is a typical value for discs (Andrews et al., 2009, 2010). And $\Sigma_{\mathrm{ring1}}$ and $\Sigma_{\mathrm{ring2}}$, the two Gaussian rings, are parameterised by:

$$\Sigma_{\mathrm{ring1,2}}(r) = \frac{1}{\sqrt{2\pi}\sigma} \exp\left[-\frac{1}{2}\left(\frac{r-\mu}{\sigma}\right)^2\right], \tag{3.4}$$

with $\mu_{\mathrm{ring1}} = 49\,$au and $\mu_{\mathrm{ring2}} = 70\,$au and $\sigma_{\mathrm{ring1}} = 1.5\,$au and $\sigma_{\mathrm{ring2}} = 4\,$au. Also, inferred from the observed continuum structure, the outer ring is set to be $\delta = 10$ times more massive. The small dust population will follow this exact structure. The large dust population, however, is constrained to the two rings only.

For the vertical structure, we adopted the same standard equation for the parametrisation of the scale height.

$$H(r) = \chi\, H_\circ \left(\frac{r}{r_\circ}\right)^{1+\psi}, \tag{3.5}$$

where $H_\circ$ is the scale height at $r = r_\circ$, $\psi$ is the flaring index and $\chi$ is a scaling factor (in the range $0 - 1$) that mimics dust settling. In addition, we divided the disc into inner and outer regions setting the boundary at a radius $R_{\text{lim}} = 53.5\text{au} = r_\circ$, where the limit between the rings is located. This separation allows using different scale heights ($H_{\text{in}}$ and $H_{\text{out}}$) and flaring index values ($\psi_{\text{in}}$ and $\psi_{\text{out}}$) for each region, giving us more freedom to explore.

Finally, with $f_{\text{sd}} = 0.01$ and $f_{\text{ld}} = 0.99$ representing the mass fraction of each specie, the density of the dust populations can be calculated as

$$\rho_{\text{smalldust}}(r, z) = \rho_{\text{gas}}(r, z)\, f_{\text{sd}}\, \zeta. \tag{3.6}$$

and

$$\rho_{\text{largedust}}(r, z) = \rho_{\text{gas}}(r, z)\, f_{\text{ld}}\, \zeta. \tag{3.7}$$
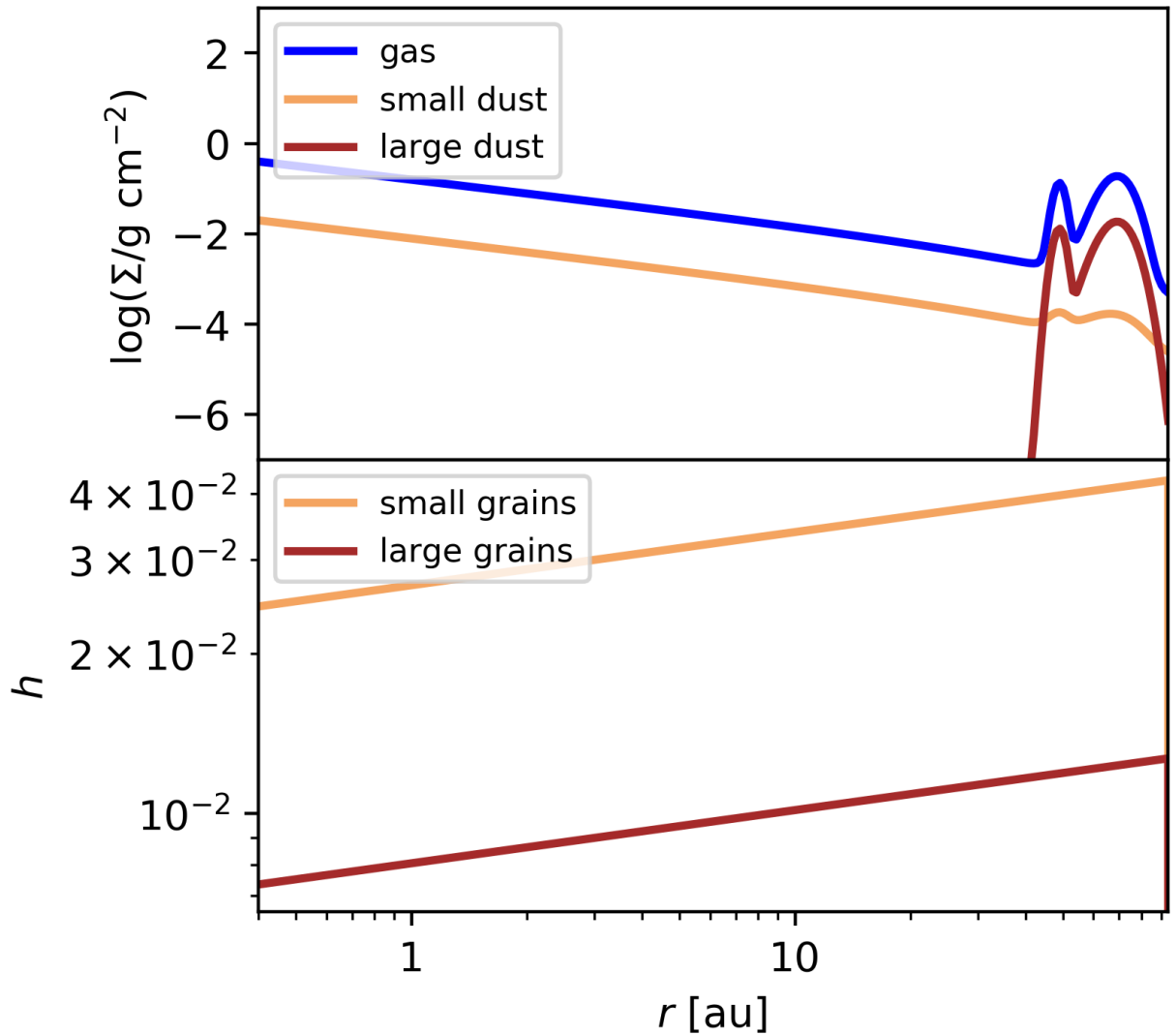


Figure 3.3: **Top:** surface density profiles for gas, large and small dust grains. **Bottom:** Aspect ratio profile $h(r) = H(r)/r$. This example model has $H_{\text{in}} = H_{\text{out}} = 0.04\,\text{au}$, $\psi_{\text{in}} = \psi_{\text{out}} = 0.1$, and $\chi = 0.3$.

The final structure goes like the profile shown in Fig. 3.3, where this model example is also imaged and shown in Fig. 3.5, the one in the centre. Using this model framework, we can explore different disc configurations and see if any reproduce the expected effect. To probe into this, we can take simulated images at 1290 and 2.2 μm to be analogous to the ALMA and the VLT images. For these, the inclination of the disc was set to 36 deg with a PA of 1 deg (same as González-Ruilova et al., 2020) and at a distance of 136.35 pc, identical to HD 147889. The 1290 μm image was later convolved with a Gaussian filter to simulate a beam size equal to the one in the ALMA observation ($\sim 0\overset{''}{.}030 \times \sim 0\overset{''}{.}021$).

## 3.2.2. Parameter space exploration

In the end, there were three free parameters for the location of the external stars and five for varying the vertical structure of the disc: $r$ and $\theta$; $H_{\mathrm{in}}$, $H_{\mathrm{out}}$, $\psi_{\mathrm{in}}$, $\psi_{\mathrm{out}}$ and $\chi$. Still, any other parameter can be modified if needed. To date, only partial exploration of those parameters has been carried out, but it has already demonstrated that many configurations exhibit the effects of external radiation.

With the exploration, we quickly found that our best chance at finding the asymmetry in the continuum simulated image is by letting the distant stars be as close as possible, setting the distance to HD 147889 at $r = 0.24$ pc. Also, we found that the polar angle $\theta$ should be between 2 and 8 deg, and the azimuthal angle $\phi$ goes between 10 and 15 deg. On the other hand, constraining the parameters of the vertical structure is a much more labours task. Still, as could be expected, we found that implementing low flaring indexes and low Chi values decreased the efficiency of the central star in heating the midplane while allowing the external radiation to penetrate deeper into the disc. Furthermore, although we created the model with a division at $R_{\mathrm{lim}}$, we have found that using the same value for the flaring indexes and the scale height throughout the whole disc works better (i.e. $H_{\mathrm{in}} = H_{\mathrm{out}}$ and $\psi_{\mathrm{in}} = \psi_{\mathrm{out}}$). Ultimately, we found that the asymmetry became more evident using flaring index values between 0.05 and 0.2, scale heights between 0.01 and 0.07 au, and Chi values between 0.1 and 0.3. These constraints suggest that ISO-OPH 2 is a relatively flat disc, illuminated at a shallow angle from a distance, with a large-dust population that is well settled into the midplane. Table 3.1 shows a summary of our results.

Table 3.1: Summary table for parameter values.

| Parameter | value range |
|---|---|
| $r$ | 0.24 au |
| $\phi$ | 10-15 deg |
| $\theta$ | 1-4 deg |
| $H_{\circ}$ | 0.01-0.07 au |
| $\psi$ | 0.05-0.2 |
| $\chi$ | 0.1-0.3 |

Fig. 3.4 and Fig. 3.5 are excellent examples of what we can get using the values we found. Each column is a value of $H_{\circ}$, from left to right goes 0.02, 0.04, 0.06 au; while the flaring angle for each row is 0.05, 0.1 and 0.2, respectively. The difference between the figures is that

for the first one, $\chi = 0.1$, and for the second one, $\chi = 0.3$. For every model, the distant stars were placed with $r = 0.24\,\mathrm{pc}$ and $\theta = 2\,\mathrm{deg}$. That said, it is easy to see that the asymmetry vanishes for flaring angles closer to 0.2. Also, that the $\chi$ value has an impact on the intensity and on how distinguishable the asymmetry appears. And finally, that the pattern changes with increasing scale height, where the peak moves from North to South.
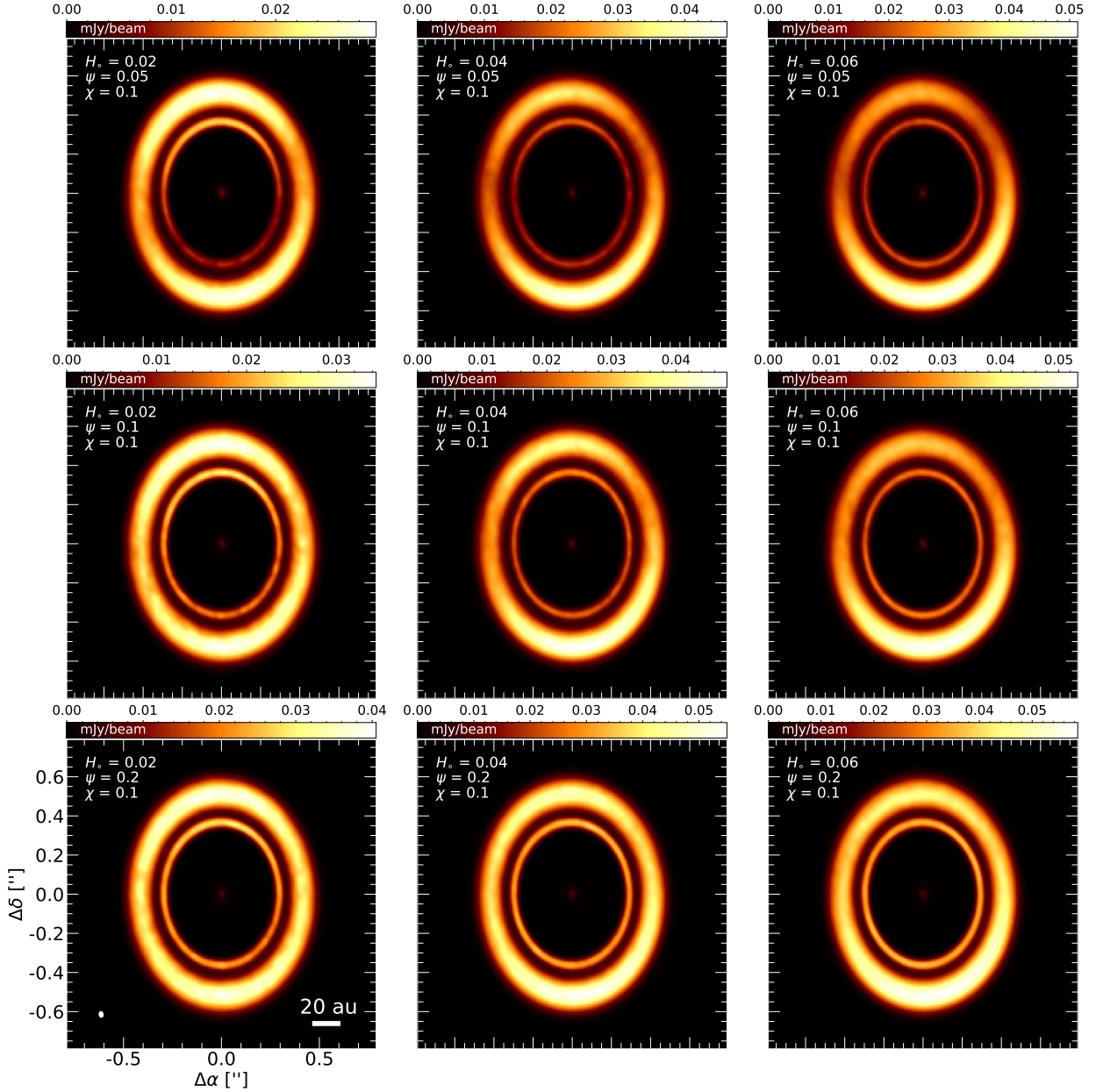


Figure 3.4: Synthetic images at $1.3\,\mathrm{mm}$ convolved with the ALMA beam. The figure shows simulated images of models with differences in their vertical structure. For all the images in the figure, the colour scale is linear. The small white ellipse in the bottom left corner shows the synthetic beam size ($\sim 0\!''\!.030 \times \sim 0\!''\!.021$).
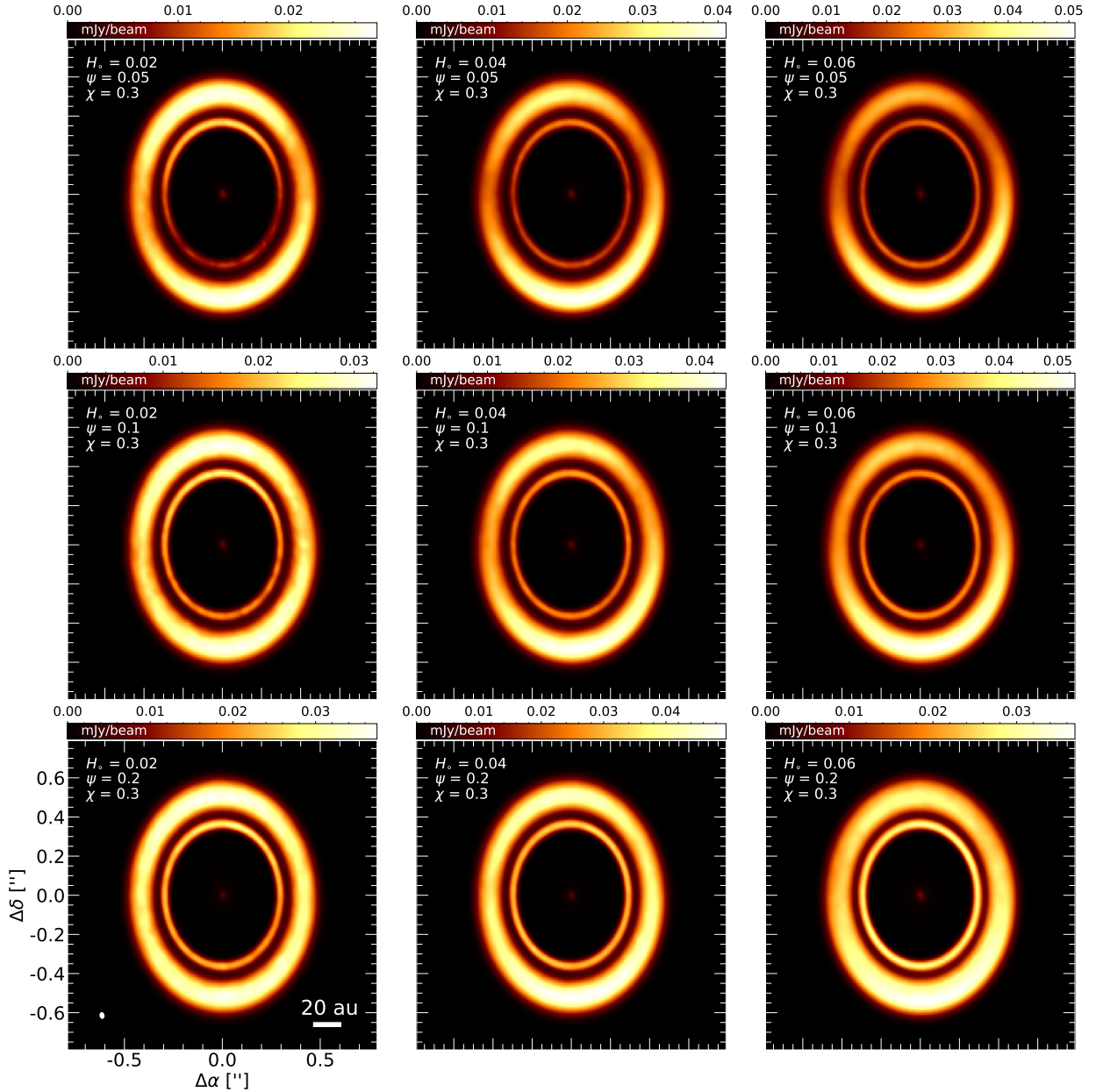
Figure 3.5: Synthetic images at 1.3 mm convolved with the ALMA beam. The figure shows simulated images of models with differences in their vertical structure. For all the images in the figure, the colour scale is linear. The small white ellipse in the bottom left corner shows the synthetic beam size ($\sim 0\overset{''}{.}030 \times \sim 0\overset{''}{.}021$).

In the images above, we can not differentiate which parts of the synthetic ALMA fluxes are due to external irradiation and which are due to the central star. However, we can take one model, let us take the centre top model in Fig. 3.6, and compare it as being illuminated only by the central star, external radiation only, or the three at once. This way, we can see and more accurately measure the impact of external radiation. However, it is easy to notice that if we added the first two images, we would not get the third one. This problem is likely because the code has to divide the photon packages between the light sources and because the temperature field simply works differently in the three scenarios, so the results are different

too. Also, the noisy look of the first one is a result of the high opacity region due to the high dust density in the midplane. Still, they illustrate perfectly how the external sources can more effectively heat the rings and give rise to the asymmetric pattern.
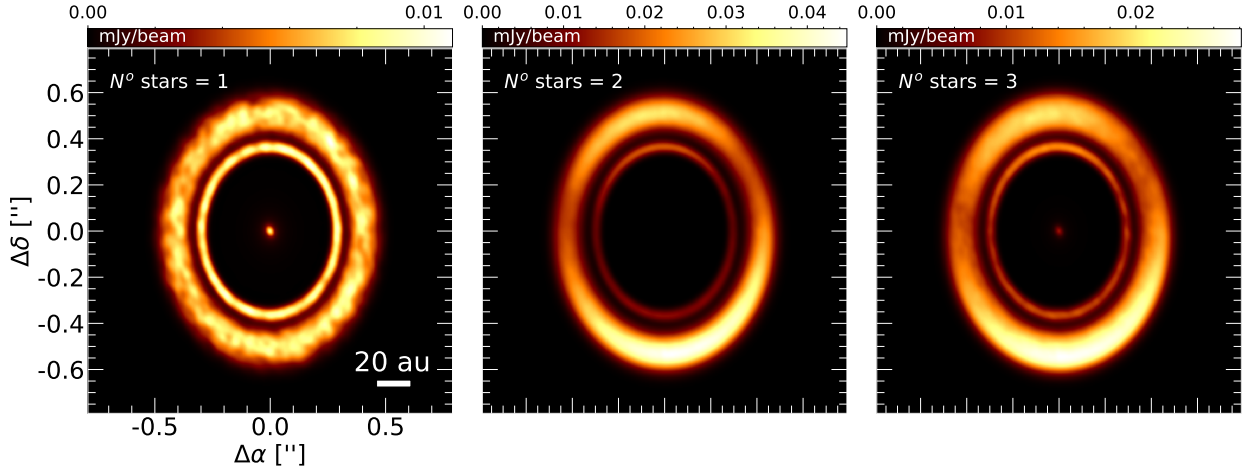


Figure 3.6: Synthetic images at 1.3 mm convolved with the ALMA beam. The figure shows simulated images of a single disc configuration under the radiation of the central star, the external radiation only, and by the three simultaneously.

On the other hand, our focus on reproducing the continuum image led us to neglect the reproduction of the 2.2 μm image. Although it is not very reliable, in Fig. 3.7 are *K*-band images of the models displayed on Fig. 3.4. The images have been altered with a subtraction of a Gaussian, similar to the NACO image, but the results are not quite the same. Still, the image shows a clear dependence on flaring angle, and to a lesser extent, on scale height. These images do not change with $\chi$, so it is fixed at 0.1. Altogether, none of the images resembles the NACO observation.
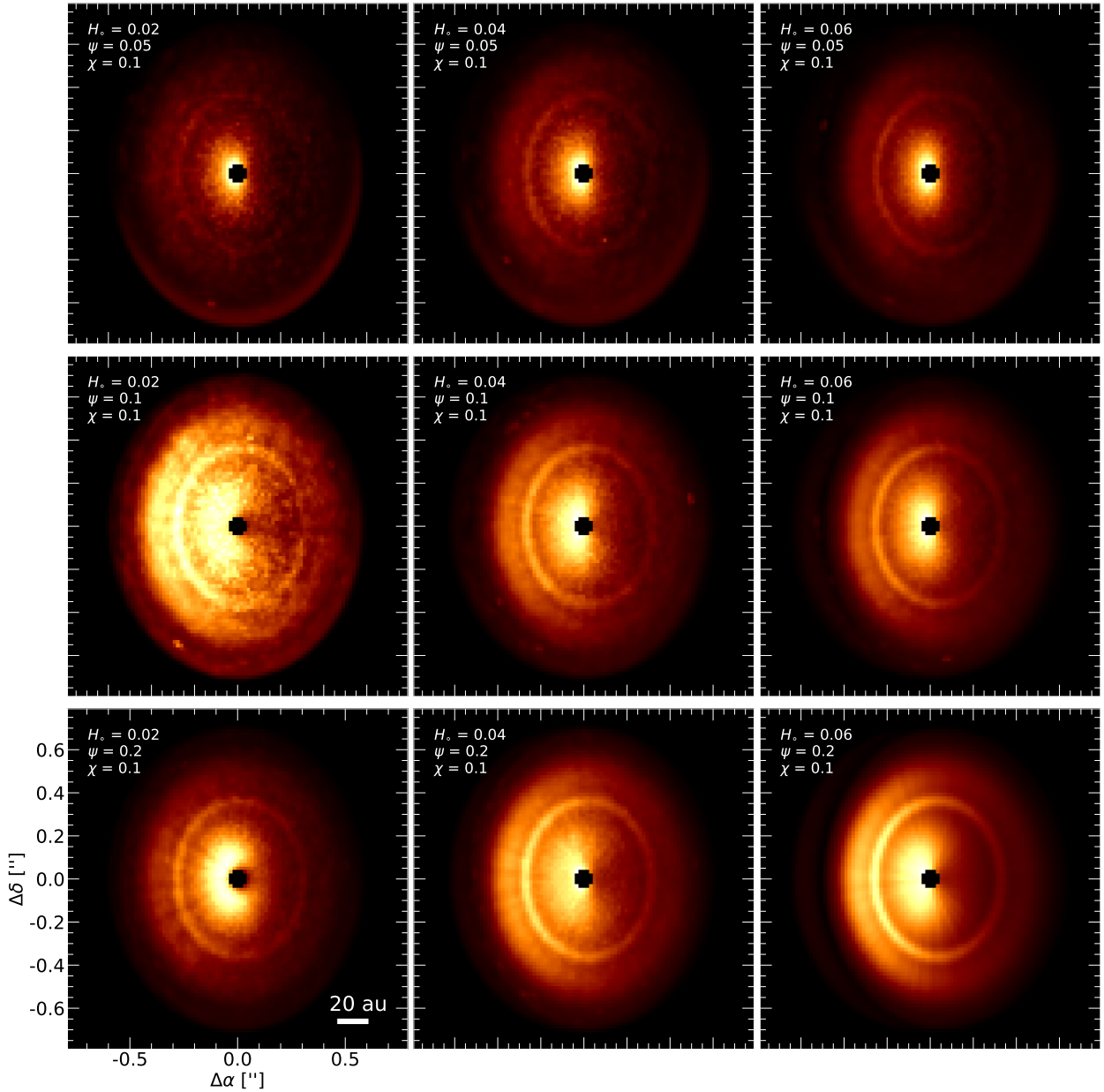
Figure 3.7: Synthetic images at 2.2 µm after a Gaussian subtraction of the stellar flux. The figure shows simulated *K*-band images of models with differences in their vertical structure.

## 3.3. Early Discussion

The preliminary results serve as an excellent proof of concept. Now we know that an ISO-Oph 2-analogous disc can, under particular circumstances, display external radiation influence from an HD 147889-analogous. However, the models still have issues that need to be addressed to get final and publishable results, as the simulated images still fail to reproduce the observations of ISO-Oph 2 accurately, but for now, they look promising.

The first known issue is that the final intensity in the 1.3 mm synthesised images is less

than the observed one. This issue is especially problematic since, from what we have found, one possible way to solve the problem is to increase the mass of the disc. However, Haworth (2021) discussed that millimetre dust mass estimates of protoplanetary exposed to intense external radiation fields are typically overestimated, as the temperatures would be higher than the usual $20\,\mathrm{K}$ value used for the calculation. Thus, the intensity of the model images should have exceeded the one from the observations, not the other way around. Another option is that the stars are wrongly modelled and have less luminosity than they should. If we could increase their luminosity, we could partially solve the issue, only that without proper justification. Furthermore, the intensity is highly dependent on the vertical structure, where models with high scale heights and flaring index values can give similar intensities but, simultaneously, are the ones with the most unfavourable structures to reproduce the feature.

One other problem is the central faint central emission created by the power law disc reaching close to the star. González-Ruilova et al. (2020) stated that the cavity observed in the ALMA image strongly constrains the mass of a putative inner disc, with an upper dust mass limit of $0.1\,M_{\oplus}$. The inner disc of our model is composed only of small dust grains and has a total mass of $\sim 0.18\,M_{\oplus}$, so currently, we are above this limit. By increasing the $R_{\mathrm{sub}}$ and creating a larger inner cavity, less mass will be in the inner disc, and the central emission will disappear. However, this would decrease the shadowing that provides the inner regions allowing more radiation to heat the midplane and could erase the asymmetric feature. The solution is non-trivial. One possibility is adding to the RADMC3D image a noise level similar to the one in the ALMA image and seeing if that makes the feature vanish.

Another problem is that the model uses point-like sources for the stars instead of finite spheres. There is an unknown problem that crushes the code when using finite spherical sources, and it came as a surprise, as in the V4046 Sgr project, it worked fine. Unfortunately, we do not know how to solve this issue. However, it should not be too concerning since $R_* << R_{\mathrm{sub}}$, meaning that the disc starts far enough from the star, so the *shining down onto the disc* phenomenon is unnecessary.

The last known issue, arguably the most obvious, is the lousy reproduction of the $2.2\,\mu\mathrm{m}$ image. Our $K$-band simulated images, like the few examples shown in Fig. 3.7, did not show quite the same features as the NACO observation. Instead, we see a strong forward scattering with a strange noisy pattern. The noise presumable comes from using too few photons to compute the image. We think the strong forward scattering problems could be improved by exploring other dust mineralogy and grain size distributions. We have not found real-life examples that showed the same thing, so we think it could be a problem related to the modelling process. Nonetheless, since our main focus was the $1.3\,\mathrm{mm}$ continuum image, we did not design the models to reproduce this additional image; what we got was within our expectations.

## 3.4.   Conclusions and Future work

The system continues to be intriguing, inviting us to go deeper into trying to get an explanation of its strange morphology. In so, our model appears to be aiming in the right direction, as the preliminary results show that our hypothesis of external radiation influence could be correct, at least partially. Of course, it is a work in progress, but we have successfully

constrained our parameter space and identified the main issues. Solving the abovementioned issues would be the main concern for continuing with the project. Then, the next step should comprehensively explore the parameters and their dependencies on each other, hopefully further constraining the space parameter and improving the reproduction of the images.

Successful results in this project could open new windows for future observing proposals to improve and upgrade the infrared images of the source, such as with the new Enhanced Resolution Imager and Spectrograph (ERIS) instrument at the VLT or even using the JWST. Whatsmore, we propose alternative paths and further developments on the project, like radiative transfer models to study how external radiation affects the locations of snow lines in ISO-Oph 2. Studying this topic could give room for new insights into the vertical structure and the possibility of planet formation events in the disc. Moreover, other scenarios cannot be ruled out, and this journey can follow many paths, where even hydrodynamic modelling could be beneficial. This was inspired by the idea from González-Ruilova et al. (2020) that suggested that dynamical effects between the binaries could somehow help shape the disc.

# Capítulo 4

# Conclusions

Throughout this thesis, we examine one fundamental aspect of planet formation: how the host star heats its surrounding disc. The constant transfer of thermal energy from the star to the protoplanetary disc will drive the evolution of such a disc and, by extension, of the future planetary system. Therefore, studying this interaction between light and matter is key to understanding the environment in which planets form. Although analytically solving the equations that describe this interaction in these conditions is impossible for practically every real case, incredible advances in computer simulation over the past years have given us exceptional tools to study these processes in unprecedented detail. In this regard, codes like RADMC3D have risen to the occasion because of their remarkable versatility and ability to be customised at will while still producing reliable results.

We implemented the RADMC3D radiative transfer code to study two extraordinary sources: V4046 Sgr and ISO-Oph 2. Both sources are protoplanetary discs that counted with high-definition radio and infrared observations, where they would stand out from the rest because of their uncommonness with their complex and intriguing morphologies. Following similar methods, each system was studied separately, V4046 Sgr in ch. 2 and ISO-Oph 2 in ch. 3. We developed 3D radiative transfer models for both cases and searched for configurations that could reproduce the observations and share light on their structures.

We implemented the RADMC3D code to study two extraordinary sources: V4046 Sgr and ISO-Oph 2. Both sources are protoplanetary discs that counted with radio and infrared observations, where they would stand out from the rest because of their uncommonness with their complex and intriguing morphologies. Each system was studied separately but following similar methods. We developed 3D radiative transfer models and searched for configurations that could reproduce and explain what is happening behind the observations.

V4046 Sgr ALMA radio and VLT infrared observations showed an arrangement of multiple rings, where a narrow ring in the continuum captured our special attention. This project led us to propose a complex radial structure with a total of four rings that can explain both images and the SED data simultaneously and with incredible accuracy. Furthermore, with our model, we were able to constrain the vertical structure of the disc, usually a complicated task for discs that are not too inclined or edge-on. The results of this research were published in Martinez-Brunner et al. (2022). Unfortunately, we do not provide an explanation for this intricate structure, but Weber et al. (2022) follow-up paper explored that subject with hy-

drodynamical simulations.

On the other hand, the radio observation of ISO-Oph 2 shows a puzzling non-axisymmetric feature that led us to propose the hypothesis that it results from exposure to external radiation from the near and high UV emitter binary system HD 147889. Consequently, we used radmc3d to build parametric models and searched for a structure that, when observed under similar conditions, could match what we observed. This project is still under development, but the preliminary results are encouraging, as the models so far display comparable features. The results show that our hypothesis seems to be pointing in the right direction, but more work must be carried out, several issues must be solved, and better results must be obtained before publishing anything.

Overall, radiative transfer simulations again demonstrated an excellent tool when exploring the thermal structure of unusual discs. In that manner, the modelling framework we developed with RADMC3D lets us construct any model, no matter the complexity and efficiently explore its parameter space. Still, regardless of how great it is, there is room for improvement. Our whole framework was constructed for the 0.41 version of RADMC3D back in 2018, and in 2020, we updated it when the 2.0 version came out. The models would run the same, and for any practical purposes, it worked fine. However, we did not explore all the new features of this newer version. Because along with general bug fixes and efficiency improvements, v2.0 came with the radmc3dPy package, a python package that integrates various modules for model construction, imaging, and post-processing of every possible output from RADMC3D. The modules are extremely powerful, easy to use, and have extended documentation and support. Thus, for any future project, I strongly recommend exploring the idea of using the radmc3dPy package. Furthermore, using software such as PARAVIEW could improve data visualisation, as it has tools to create complex but illustrative 3D plots. This should not be difficult to implement, given that RADMC3D already integrates the option to write the outputs in .vtk format.

With a final comment, I would like close this thesis. One key thing about science is that one can always try another thing; if it fails, one must try to understand why it failed. This way, one always has a way of learning from it; otherwise, a failed experiment is completely useless.

# Bibliography

Fred C. Adams, Charles J. Lada, and Frank H. Shu. Spectral Evolution of Young Stellar Objects. *ApJ*, 312:788, January 1987. doi: 10.1086/164924.

R. D. Alexander, C. J. Clarke, and J. E. Pringle. Photoevaporation of protoplanetary discs - II. Evolutionary models and observable properties. *MNRAS*, 369(1):229–239, June 2006. doi: 10.1111/j.1365-2966.2006.10294.x.

Richard Alexander. The Dispersal of Protoplanetary Disks around Binary Stars. *ApJ*, 757 (2):L29, October 2012. doi: 10.1088/2041-8205/757/2/L29.

Sean M. Andrews. Observations of Protoplanetary Disk Structures. *ARA&A*, 58:483–528, August 2020. doi: 10.1146/annurev-astro-031220-010302.

Sean M. Andrews, D. J. Wilner, A. M. Hughes, Chunhua Qi, and C. P. Dullemond. PROTO-PLANETARY DISK STRUCTURES IN OPHIUCHUS. *The Astrophysical Journal*, 700(2): 1502–1523, jul 2009. doi: 10.1088/0004-637x/700/2/1502. URL https://doi.org/10.1088%2F0004-637x%2F700%2F2%2F1502.

Sean M. Andrews, D. J. Wilner, A. M. Hughes, Chunhua Qi, and C. P. Dullemond. PROTO-PLANETARY DISK STRUCTURES IN OPHIUCHUS. II. EXTENSION TO FAINTER SOURCES. *The Astrophysical Journal*, 723(2):1241–1254, oct 2010. doi: 10.1088/0004-637x /723/2/1241. URL https://doi.org/10.1088%2F0004-637x%2F723%2F2%2F1241.

Philip J. Armitage. *Astrophysics of Planet Formation*. Cambridge University Press, 2010.

Pawel Artymowicz and Stephen H. Lubow. Dynamics of Binary-Disk Interaction. I. Resonances and Disk Gap Sizes. *ApJ*, 421:651, Feb 1994. doi: 10.1086/173679.

H. Avenhaus, S. P. Quanz, H. M. Schmid, C. Dominik, T. Stolker, C. Ginski, J. de Boer, J. Szulágyi, A. Garufi, A. Zurlo, J. Hagelberg, M. Benisty, T. Henning, F. Ménard, M. R. Meyer, A. Baruffolo, A. Bazzon, J. L. Beuzit, A. Costille, K. Dohlen, J. H. Girard, D. Gisler, M. Kasper, D. Mouillet, J. Pragt, R. Roelfsema, B. Salasnich, and J.-F. Sauvage. Exploring dust around HD 142527 down to 0.′025 (4 au) using SPHERE/ZIMPOL. *The Astronomical Journal*, 154(1):33, jun 2017. doi: 10.3847/1538-3881/aa7560. URL https://doi.org/10.3847%2F1538-3881%2Faa7560.

Henning Avenhaus, Sascha P. Quanz, Antonio Garufi, Sebastian Perez, Simon Casassus, Christophe Pinte, Gesa H.-M. Bertrang, Claudio Caceres, Myriam Benisty, and Carsten Dominik. Disks around t tauri stars with SPHERE (DARTTS-s). i. SPHERE/IRDIS polarimetric imaging of eight prominent t tauri disks. *The Astrophysical Journal*, 863(1):44, aug 2018. doi: 10.3847/1538-4357/aab846. URL https://doi.org/10.3847%2F1538-4357%2Faab846.

Jennifer B. Bergner, Viviana G. Guzmán, Karin I. Öberg, Ryan A. Loomis, and Jamila Pegues. A survey of CH3cn and HC3n in protoplanetary disks. *The Astrophysical Journal*, 857(1):69, apr 2018. doi: 10.3847/1538-4357/aab664. URL https://doi.org/10.3847/1538-4357/aab664.

J. L. Beuzit, A. Vigan, D. Mouillet, K. Dohlen, R. Gratton, A. Boccaletti, J. F. Sauvage, H. M. Schmid, M. Langlois, C. Petit, A. Baruffolo, M. Feldt, J. Milli, Z. Wahhaj, L. Abe, U. Anselmi, J. Antichi, R. Barette, J. Baudrand, P. Baudoz, A. Bazzon, P. Bernardi, P. Blanchard, R. Brast, P. Bruno, T. Buey, M. Carbillet, M. Carle, E. Cascone, F. Chapron, J. Charton, G. Chauvin, R. Claudi, A. Costille, V. De Caprio, J. de Boer, A. Delboulbé, S. Desidera, C. Dominik, M. Downing, O. Dupuis, C. Fabron, D. Fantinel, G. Farisato, P. Feautrier, E. Fedrigo, T. Fusco, P. Gigan, C. Ginski, J. Girard, E. Giro, D. Gisler, L. Gluck, C. Gry, T. Henning, N. Hubin, E. Hugot, S. Incorvaia, M. Jaquet, M. Kasper, E. Lagadec, A. M. Lagrange, H. Le Coroller, D. Le Mignant, B. Le Ruyet, G. Lessio, J. L. Lizon, M. Llored, L. Lundin, F. Madec, Y. Magnard, M. Marteaud, P. Martinez, D. Maurel, F. Ménard, D. Mesa, O. Möller-Nilsson, T. Moulin, C. Moutou, A. Origné, J. Parisot, A. Pavlov, D. Perret, J. Pragt, P. Puget, P. Rabou, J. Ramos, J. M. Reess, F. Rigal, S. Rochat, R. Roelfsema, G. Rousset, A. Roux, M. Saisse, B. Salasnich, E. Santambrogio, S. Scuderi, D. Segransan, A. Sevin, R. Siebenmorgen, C. Soenke, E. Stadler, M. Suarez, D. Tiphène, M. Turatto, S. Udry, F. Vakili, L. B. F. M. Waters, L. Weber, F. Wildi, G. Zins, and A. Zurlo. SPHERE: the exoplanet imager for the Very Large Telescope. *A&A*, 631: A155, November 2019. doi: 10.1051/0004-6361/201935251.

J. E. Bjorkman and Kenneth Wood. Radiative Equilibrium and Temperature Correction in Monte Carlo Radiation Transfer. *ApJ*, 554(1):615–623, June 2001. doi: 10.1086/321336.

A.P. Boss and F.J. Ciesla. 2.3 - the solar nebula. In Heinrich D. Holland and Karl K. Turekian, editors, *Treatise on Geochemistry (Second Edition)*, pages 37–53. Elsevier, Oxford, second edition edition, 2014. ISBN 978-0-08-098300-4. doi: https://doi.org/10.1016/B978-0-08-095975-7.00119-4. URL https://www.sciencedirect.com/science/article/pii/B9780080959757001194.

M. Cárcamo, P. E. Román, S. Casassus, V. Moral, and F. R. Rannou. Multi-GPU maximum entropy image synthesis for radio astronomy. *Astronomy and Computing*, 22:16–27, January 2018. doi: 10.1016/j.ascom.2017.11.003.

S. Casassus, G. F. Cabrera, F. Förster, T. J. Pearson, A. C. S. Readhead, and C. Dickinson. Morphological Analysis of the Centimeter-Wave Continuum in the Dark Cloud LDN 1622. *ApJ*, 639(2):951–964, March 2006. doi: 10.1086/499517.

S. Casassus, G. van der Plas, S. M. Perez, W. R. F. Dent, E. Fomalont, J. Hagelberg, A. Hales, A. Jordán, D. Mawet, F. Ménard, A. Wootten, D. Wilner, A. M. Hughes, M. R. Schreiber, J. H. Girard, B. Ercolano, H. Canovas, P. E. Román, and V. Salinas. Flows of gas through a protoplanetary gap. *Nature*, 493:191–194, January 2013. doi: 10.1038/nature11769.

S. Casassus, S. Marino, W. Lyra, C. Baruteau, M. Vidal, A. Wootten, S. Pérez, F. Alarcon, M. Barraza, M. Cárcamo, R. Dong, A. Sierra, Z. Zhu, L. Ricci, V. Christiaens, and L. Cieza. Cm-wavelength observations of MWC 758: resolved dust trapping in a vortex. *MNRAS*, 483:3278–3287, March 2019a. doi: 10.1093/mnras/sty3269.

Simon Casassus, Clive Dickinson, Kieran Cleary, Roberta Paladini, Mireya Etxaluze, Tanya Lim, Glenn J. White, Michael Burton, Balt Indermuehle, Otmar Stahl, and Patrick Roche. Centimetre-wave continuum radiation from the $\rho$ Ophiuchi molecular cloud. *MNRAS*, 391 (3):1075–1090, December 2008. doi: 10.1111/j.1365-2966.2008.13954.x.

Simon Casassus, Henning Avenhaus, Sebastián Pérez, Víctor Navarro, Miguel Cárcamo, Sebastián Marino, Lucas Cieza, Sascha P. Quanz, Felipe Alarcón, Alice Zurlo, Axel Osses, Fernando R. Rannou, Pablo E. Román, and Marcelo Barraza. An inner warp in the DoAr 44 T Tauri transition disc. *MNRAS*, 477(4):5104–5114, Jul 2018. doi: 10.1093/mnras/sty894.

Simon Casassus, Sebastián Pérez, Axel Osses, and Sebastián Marino. Cooling in the shade of warped transition discs. *MNRAS*, 486(1):L58–L62, June 2019b. doi: 10.1093/mnrasl/slz059.

Simon Casassus, Valentin Christiaens, Miguel Cárcamo, Sebastián Pérez, Philipp Weber, Barbara Ercolano, Nienke van der Marel, Christophe Pinte, Ruobing Dong, Clément Baruteau, Lucas Cieza, Ewine F van Dishoeck, Andrés Jordan, Daniel J Price, Olivier Absil, Carla Arce-Tord, Virginie Faramaz, Christian Flores, and Maddalena Reggiani. A dusty filament and turbulent CO spirals in HD 135344B - SAO 206462. *MNRAS*, 507(3):3789–3809, 08 2021. ISSN 0035-8711. doi: 10.1093/mnras/stab2359. URL https://doi.org/10.1093/mnras/stab2359.

F. Castelli, R. G. Gratton, and R. L. Kurucz. Notes on the convection in the ATLAS9 model atmospheres. *A&A*, 318:841–869, Feb 1997.

E. I. Chiang and P. Goldreich. Spectral Energy Distributions of T Tauri Stars with Passive Circumstellar Disks. *ApJ*, 490(1):368–376, November 1997. doi: 10.1086/304869.

Lucas A. Cieza, Dary Ruíz-Rodríguez, Antonio Hales, Simon Casassus, Sebastian Pérez, Camilo Gonzalez-Ruilova, Hector Cánovas, Jonathan P. Williams, Alice Zurlo, Megan Ansdell, Henning Avenhaus, Amelia Bayo, Gesa H. M. Bertrang, Valentin Christiaens, William Dent, Gabriel Ferrero, Roberto Gamen, Johan Olofsson, Santiago Orcajo, Karla Peña Ramírez, David Principe, Matthias R. Schreiber, and Gerrit van der Plas. The Ophiuchus DIsc Survey Employing ALMA (ODISEA) - I: project description and continuum images at 28 au resolution. *MNRAS*, 482(1):698–714, January 2019. doi: 10.1093/mnras/sty2653.

M. Cohen and F. C. Witteborn. Spectrophotometry at 10 microns of T Tauri stars. *ApJ*, 294:345–356, July 1985. doi: 10.1086/163302.

R. M. Cutri and et al. VizieR Online Data Catalog: WISE All-Sky Data Release (Cutri+ 2012). *VizieR Online Data Catalog*, art. II/311, April 2012.

R. M. Cutri, M. F. Skrutskie, S. van Dyk, C. A. Beichman, J. M. Carpenter, T. Chester, L. Cambresy, T. Evans, J. Fowler, J. Gizis, E. Howard, J. Huchra, T. Jarrett, E. L. Kopan, J. D. Kirkpatrick, R. M. Light, K. A. Marsh, H. McCallon, S. Schneider, R. Stiening, M. Sykes, M. Weinberg, W. A. Wheaton, S. Wheelock, and N. Zacarias. VizieR Online Data Catalog: 2MASS All-Sky Catalog of Point Sources (Cutri+ 2003). *VizieR Online Data Catalog*, art. II/246, June 2003.

Paola D'Alessio, Nuria Calvet, Lee Hartmann, Susana Lizano, and Jorge Canto. Accretion disks around young objects. II. tests of well-mixed models with ISM dust. *The Astrophysical Journal*, 527(2):893–909, dec 1999. doi: 10.1086/308103. URL https://doi.org/10.1086/308103.

J.-F. Donati, S. G. Gregory, T. Montmerle, A. Maggio, C. Argiroffi, G. Sacco, G. Hussain, J. Kastner, S. H. P. Alencar, M. Audard, J. Bouvier, F. Damiani, M. Güdel, D. Huenemoerder, and G. A. Wade. The close classical T Tauri binary V4046 Sgr: complex magnetic fields and distributed mass accretion. *Monthly Notices of the Royal Astronomical Society*, 417(3):1747–1759, 10 2011. ISSN 0035-8711. doi: 10.1111/j.1365-2966.2011.19366.x. URL https://doi.org/10.1111/j.1365-2966.2011.19366.x.

V. D'Orazi, R. Gratton, S. Desidera, H. Avenhaus, D. Mesa, T. Stolker, E. Giro, S. Benatti, H. Jang-Condell, E. Rigliaco, E. Sissa, T. Scatolin, M. Benisty, T. Bhowmik, A. Boccaletti, M. Bonnefoy, W. Brandner, E. Buenzli, G. Chauvin, S. Daemgen, M. Damasso, M. Feldt, R. Galicher, J. Girard, M. Janson, J. Hagelberg, D. Mouillet, Q. Kral, J. Lannier, A. M. Lagrange, M. Langlois, A. L. Maire, F. Menard, O. Moeller-Nilsson, C. Perrot, S. Peretti, P. Rabou, J. Ramos, L. Rodet, R. Roelfsema, A. Roux, G. Salter, J. E. Schlieder, T. Schmidt, J. Szulagyi, C. Thalmann, P. Thebault, G. van der Plas, A. Vigan, and A. Zurlo. Mapping of shadows cast on a protoplanetary disk by a close binary system. *Nature Astronomy*, 3:167–172, November 2019. doi: 10.1038/s41550-018-0626-6.

B. T. Draine. Scattering by Interstellar Dust Grains. II. X-Rays. *ApJ*, 598(2):1026–1037, December 2003. doi: 10.1086/379123.

B. T. Draine. Interstellar Dust Models and Evolutionary Implications. In T. Henning, E. Grün, and J. Steinacker, editors, *Cosmic Dust - Near and Far*, volume 414 of *Astronomical Society of the Pacific Conference Series*, page 453, December 2009.

Joanna Drazkowska, Shengtai Li, Til Birnstiel, Sebastian M. Stammler, and Hui Li. Including Dust Coagulation in Hydrodynamic Models of Protoplanetary Disks: Dust Evolution in the Vicinity of a Jupiter-mass Planet. *ApJ*, 885(1):91, November 2019. doi: 10.3847/1538-4357/ab46b7.

B. Dubrulle, G. Morfill, and M. Sterzik. The dust subdisk in the protoplanetary nebula. *Icarus*, 114(2):237–246, April 1995. doi: 10.1006/icar.1995.1058.

C. P. Dullemond and C. Dominik. The effect of dust settling on the appearance of protoplanetary disks. *A&A*, 421:1075–1086, July 2004. doi: 10.1051/0004-6361:20040284.

C. P. Dullemond, D. Hollenbach, I. Kamp, and P. D'Alessio. Models of the Structure and Evolution of Protoplanetary Disks. In Bo Reipurth, David Jewitt, and Klaus Keil, editors, *Protostars and Planets V*, page 555, January 2007.

C. P. Dullemond, A. Juhasz, A. Pohl, F. Sereshti, R. Shetty, T. Peters, B. Commercon, and M. Flock. RADMC-3D: A multi-purpose radiative transfer tool, February 2012.

Cornelis P. Dullemond, Tilman Birnstiel, Jane Huang, Nicolás T. Kurtovic, Sean M. Andrews, Viviana V. Guzmán, Laura M. Pérez, Andrea Isella, Zhaohuan Zhu, Myriam Benisty, David J. Wilner, Xue-Ning Bai, John M. Carpenter, Shangjia Zhang, and Luca Ricci. The Disk Substructures at High Angular Resolution Project (DSHARP). VI. Dust Trapping in Thin-ringed Protoplanetary Disks. *ApJ*, 869(2):L46, December 2018. doi: 10.3847/2041-8213/aaf742.

A. Dutrey, S. Guilloteau, and M. Guelin. Chemistry of protosolar-like nebulae: The molecular content of the DM Tau and GG Tau disks. *A&A*, 317:L55–L58, January 1997.

D. Fedele, M. E. van den Ancker, Th. Henning, R. Jayawardhana, and J. M. Oliveira. Timescale of mass accretion in pre-main-sequence stars. *A&A*, 510:A72, February 2010. doi: 10.1051/0004-6361/200912810.

Kevin Flaherty, A. Meredith Hughes, Jacob B. Simon, Chunhua Qi, Xue-Ning Bai, Alyssa Bulatek, Sean M. Andrews, David J. Wilner, and Ágnes Kóspál. Measuring turbulent motion in planet-forming disks with ALMA: A detection around DM tau and nondetections around MWC 480 and v4046 sgr. *The Astrophysical Journal*, 895(2):109, jun 2020. doi: 10.3847/1538-4357/ab8cc5. URL https://doi.org/10.3847%2F1538-4357%2Fab8cc5.

Kevin France, Gregory J. Herczeg, Matthew McJunkin, and Steven V. Penton. Co/h2 abundance ratio 104 in a protoplanetary disk*. *The Astrophysical Journal*, 794(2):160, oct 2014. doi: 10.1088/0004-637X/794/2/160. URL https://dx.doi.org/10.1088/0004-637X/794/2/160.

Logan Francis and Nienke van der Marel. Dust-depleted inner disks in a large sample of transition disks through long-baseline ALMA observations. *The Astrophysical Journal*, 892(2):111, apr 2020. doi: 10.3847/1538-4357/ab7b63. URL https://doi.org/10.3847/1538-4357/ab7b63.

Gaia Collaboration, Brown, A. G. A., Vallenari, A., Prusti, T., de Bruijne, J. H. J., Babusiaux, C., Biermann, M., Creevey, O. L., Evans, D. W., Eyer, L., Hutton, A., Jansen, F., Jordi, C., Klioner, S. A., Lammers, U., Lindegren, L., Luri, X., Mignard, F., Panem, C., Pourbaix, D., Randich, S., Sartoretti, P., Soubiran, C., Walton, N. A., Arenou, F., Bailer-Jones, C. A. L., Bastian, U., Cropper, M., Drimmel, R., Katz, D., Lattanzi, M. G., van Leeuwen, F., Bakker, J., Cacciari, C., Castañeda, J., De Angeli, F., Ducourant, C., Fabricius, C., Fouesneau, M., Frémat, Y., Guerra, R., Guerrier, A., Guiraud, J., Jean-Antoine Piccolo, A., Masana, E., Messineo, R., Mowlavi, N., Nicolas, C., Nienartowicz, K., Pailler, F., Panuzzo, P., Riclet, F., Roux, W., Seabroke, G. M., Sordo, R., Tanga, P., Thévenin, F., Gracia-Abril, G., Portell, J., Teyssier, D., Altmann, M., Andrae, R., Bellas-Velidis, I., Benson, K., Berthier, J., Blomme, R., Brugaletta, E., Burgess, P. W., Busso, G., Carry, B., Cellino, A., Cheek, N., Clementini, G., Damerdji, Y., Davidson, M., Delchambre, L., Dell´Oro, A., Fernández-Hernández, J., Galluccio, L., García-Lario, P., Garcia-Reinaldos, M., González-Núñez, J., Gosset, E., Haigron, R., Halbwachs, J.-L., Hambly, N. C., Harrison, D. L., Hatzidimitriou, D., Heiter, U., Hernández, J., Hestroffer, D., Hodgkin, S. T., Holl, B., Janßen, K., Jevardat de Fombelle, G., Jordan, S., Krone-Martins, A., Lanzafame, A. C., Löffler, W., Lorca, A., Manteiga, M., Marchal, O., Marrese, P. M., Moitinho, A., Mora, A., Muinonen, K., Osborne, P., Pancino, E., Pauwels, T., Petit, J.-M., Recio-Blanco, A., Richards, P. J., Riello, M., Rimoldini, L., Robin, A. C., Roegiers, T., Rybizki, J., Sarro, L. M., Siopis, C., Smith, M., Sozzetti, A., Ulla, A., Utrilla, E., van Leeuwen, M., van Reeven, W., Abbas, U., Abreu Aramburu, A., Accart, S., Aerts, C., Aguado, J. J., Ajaj, M., Altavilla, G., Álvarez, M. A., Álvarez Cid-Fuentes, J., Alves, J., Anderson, R. I., Anglada Varela, E., Antoja, T., Audard, M., Baines, D., Baker, S. G., Balaguer-Núñez, L., Balbinot, E., Balog, Z., Barache, C., Barbato, D., Barros, M., Barstow, M. A., Bartolomé, S., Bassilana, J.-L., Bauchet, N., Baudesson-Stella, A., Becciani, U., Bellazzini, M., Bernet, M., Bertone, S., Bianchi, L., Blanco-Cuaresma, S., Boch, T., Bombrun, A., Bossini, D., Bouquillon, S., Bragaglia, A., Bramante, L., Breedt, E., Bressan, A., Brouillet, N., Bucciarelli, B., Burlacu, A., Busonero, D., Butkevich, A. G., Buzzi, R., Caffau, E., Cancelliere, R., Cánovas, H., Cantat-Gaudin, T., Carballo, R., Carlucci, T., Carnerero, M. I, Carrasco, J. M., Casamiquela, L., Castellani,

M., Castro-Ginard, A., Castro Sampol, P., Chaoul, L., Charlot, P., Chemin, L., Chiavassa, A., Cioni, M.-R. L., Comoretto, G., Cooper, W. J., Cornez, T., Cowell, S., Crifo, F., Crosta, M., Crowley, C., Dafonte, C., Dapergolas, A., David, M., David, P., de Laverny, P., De Luise, F., De March, R., De Ridder, J., de Souza, R., de Teodoro, P., de Torres, A., del Peloso, E. F., del Pozo, E., Delbo, M., Delgado, A., Delgado, H. E., Delisle, J.-B., Di Matteo, P., Diakite, S., Diener, C., Distefano, E., Dolding, C., Eappachen, D., Edvardsson, B., Enke, H., Esquej, P., Fabre, C., Fabrizio, M., Faigler, S., Fedorets, G., Fernique, P., Fienga, A., Figueras, F., Fouron, C., Fragkoudi, F., Fraile, E., Franke, F., Gai, M., Garabato, D., Garcia-Gutierrez, A., García-Torres, M., Garofalo, A., Gavras, P., Gerlach, E., Geyer, R., Giacobbe, P., Gilmore, G., Girona, S., Giuffrida, G., Gomel, R., Gomez, A., Gonzalez-Santamaria, I., González-Vidal, J. J., Granvik, M., Gutiérrez-Sánchez, R., Guy, L. P., Hauser, M., Haywood, M., Helmi, A., Hidalgo, S. L., Hilger, T., Hladczuk, N., Hobbs, D., Holland, G., Huckle, H. E., Jasniewicz, G., Jonker, P. G., Juaristi Campillo, J., Julbe, F., Karbevska, L., Kervella, P., Khanna, S., Kochoska, A., Kontizas, M., Kordopatis, G., Korn, A. J., Kostrzewa-Rutkowska, Z., Kruszy´nska, K., Lambert, S., Lanza, A. F., Lasne, Y., Le Campion, J.-F., Le Fustec, Y., Lebreton, Y., Lebzelter, T., Leccia, S., Leclerc, N., Lecoeur-Taibi, I., Liao, S., Licata, E., Lindstrøm, E. P., Lister, T. A., Livanou, E., Lobel, A., Madrero Pardo, P., Managau, S., Mann, R. G., Marchant, J. M., Marconi, M., Marcos Santos, M. M. S., Marinoni, S., Marocco, F., Marshall, D. J., Martin Polo, L., Martín-Fleitas, J. M., Masip, A., Massari, D., Mastrobuono-Battisti, A., Mazeh, T., McMillan, P. J., Messina, S., Michalik, D., Millar, N. R., Mints, A., Molina, D., Molinaro, R., Molnár, L., Montegriffo, P., Mor, R., Morbidelli, R., Morel, T., Morris, D., Mulone, A. F., Munoz, D., Muraveva, T., Murphy, C. P., Musella, I., Noval, L., Ordénovic, C., Orrù, G., Osinde, J., Pagani, C., Pagano, I., Palaversa, L., Palicio, P. A., Panahi, A., Pawlak, M., Peñalosa Esteller, X., Penttilä, A., Piersimoni, A. M., Pineau, F.-X., Plachy, E., Plum, G., Poggio, E., Poretti, E., Poujoulet, E., Prsa, A., Pulone, L., Racero, E., Ragaini, S., Rainer, M., Raiteri, C. M., Rambaux, N., Ramos, P., Ramos-Lerate, M., Re Fiorentin, P., Regibo, S., Reylé, C., Ripepi, V., Riva, A., Rixon, G., Robichon, N., Robin, C., Roelens, M., Rohrbasser, L., Romero-Gómez, M., Rowell, N., Royer, F., Rybicki, K. A., Sadowski, G., Sagristà Sellés, A., Sahlmann, J., Salgado, J., Salguero, E., Samaras, N., Sanchez Gimenez, V., Sanna, N., Santoveña, R., Sarasso, M., Schultheis, M., Sciacca, E., Segol, M., Segovia, J. C., Ségransan, D., Semeux, D., Shahaf, S., Siddiqui, H. I., Siebert, A., Siltala, L., Slezak, E., Smart, R. L., Solano, E., Solitro, F., Souami, D., Souchay, J., Spagna, A., Spoto, F., Steele, I. A., Steidelmüller, H., Stephenson, C. A., Süveges, M., Szabados, L., Szegedi-Elek, E., Taris, F., Tauran, G., Taylor, M. B., Teixeira, R., Thuillot, W., Tonello, N., Torra, F., Torra, J., Turon, C., Unger, N., Vaillant, M., van Dillen, E., Vanel, O., Vecchiato, A., Viala, Y., Vicente, D., Voutsinas, S., Weiler, M., Wevers, T., Wyrzykowski, L., Yoldas, A., Yvard, P., Zhao, H., Zorec, J., Zucker, S., Zurbach, C., and Zwitter, T. Gaia early data release 3 - summary of the contents and survey properties. *A&A*, 649:A1, 2021. doi: 10.1051/0004-6361/202039657. URL https://doi.org/10.1051/0004-6361/202039657.

A. Garufi, G. Meeus, M. Benisty, S. P. Quanz, A. Banzatti, M. Kama, H. Canovas, C. Eiroa, H. M. Schmid, T. Stolker, A. Pohl, E. Rigliaco, F. Menard, M. R. Meyer, R. van Boekel, and C. Dominik. Evolution of protoplanetary disks from their taxonomy in scattered light: Group I vs. Group II. *A&A*, 603:A21, July 2017. doi: 10.1051/0004-6361/201630320.

A. Garufi, H. Avenhaus, S. Pérez, S. P. Quanz, R. G. van Holstein, G. H. M. Bertrang, S. Casassus, L. Cieza, D. A. Principe, G. van der Plas, and A. Zurlo. Disks Around T

Tauri Stars with SPHERE (DARTTS-S). II. Twenty-one new polarimetric images of young stellar disks. *A&A*, 633:A82, January 2020. doi: 10.1051/0004-6361/201936946.

T. Gatti, L. Testi, A. Natta, S. Randich, and J. Muzerolle. Accretion in $\rho$ Ophiuchus brown dwarfs: infrared hydrogen line ratios. *A&A*, 460(2):547–553, December 2006. doi: 10.1051/0004-6361:20066095.

Camilo González-Ruilova, Lucas A. Cieza, Antonio S. Hales, Sebastián Pérez, Alice Zurlo, Carla Arce-Tord, Simón Casassus, Hector Cánovas, Mario Flock, Gregory J. Herczeg, Paola Pinilla, Daniel J. Price, David A. Principe, Dary Ruíz-Rodríguez, and Jonathan P. Williams. A Tale of Two Transition Disks: ALMA Long-baseline Observations of ISO-Oph 2 Reveal Two Closely Packed Nonaxisymmetric Rings and a ∼2 au Cavity. *ApJ*, 902(2): L33, October 2020. doi: 10.3847/2041-8213/abbcce.

U. Gorti and D. Hollenbach. Photoevaporation of Circumstellar Disks By Far-Ultraviolet, Extreme-Ultraviolet and X-Ray Radiation from the Central Star. *ApJ*, 690(2):1539–1552, January 2009. doi: 10.1088/0004-637X/690/2/1539.

S. Guilloteau, E. Di Folco, A. Dutrey, M. Simon, N. Grosso, and V. Piétu. A sensitive survey for $^{13}$CO, CN, H$_2$CO, and SO in the disks of T Tauri and Herbig Ae stars. *A&A*, 549:A92, January 2013. doi: 10.1051/0004-6361/201220298.

S. Guilloteau, L. Reboussin, A. Dutrey, E. Chapillon, V. Wakelam, V. Piétu, E. Di Folco, D. Semenov, and Th. Henning. Chemistry in disks. X. The molecular content of protoplanetary disks in Taurus. *A&A*, 592:A124, August 2016. doi: 10.1051/0004-6361/201527088.

V. V. Guzmán, K. I. Öberg, J. Huang, R. Loomis, and C. Qi. Nitrogen fractionation in protoplanetary disks from the h13cn/HC15n ratio. *The Astrophysical Journal*, 836(1):30, feb 2017. doi: 10.3847/1538-4357/836/1/30. URL https://doi.org/10.3847/1538-4357/836/1/30.

Thomas J Haworth. Warm millimetre dust in protoplanetary discs near massive stars. *Monthly Notices of the Royal Astronomical Society*, 503(3):4172–4182, 03 2021. ISSN 0035-8711. doi: 10.1093/mnras/stab728. URL https://doi.org/10.1093/mnras/stab728.

Thomas J. Haworth, Stefano Facchini, Cathie J. Clarke, and L. Ilsedore Cleeves. First evidence of external disc photoevaporation in a low mass star forming region: the case of IM Lup. *MNRAS*, 468(1):L108–L112, June 2017. doi: 10.1093/mnrasl/slx037.

George Helou and D. W Walker. Infrared Astronomical Satellite (IRAS) Catalogs and Atlases.Volume 7: The Small Scale Structure Catalog. *Infrared astronomical satellite (IRAS) catalogs and atlases. Volume 7*, 7, January 1988.

E. Hog, C. Fabricius, V. V. Makarov, S. Urban, T. Corbin, G. Wycoff, U. Bastian, P. Schwekendiek, and A. Wicenec. The Tycho-2 catalogue of the 2.5 million brightest stars. *A&A*, 355:L27–L30, March 2000.

Michiel R. Hogerheijde. *Protoplanetary Disk*, pages 1357–1366. Springer Berlin Heidelberg, Berlin, Heidelberg, 2011. ISBN 978-3-642-11274-4. doi: 10.1007/978-3-642-11274-4_1299. URL https://doi.org/10.1007/978-3-642-11274-4_1299.

Michiel R. Hogerheijde, Edwin A. Bergin, Christian Brinch, L. Ilsedore Cleeves, Jeffrey K. J. Fogel, Geoffrey A. Blake, Carsten Dominik, Dariusz C. Lis, Gary Melnick, David Neufeld,

Olja Panić, John C. Pearson, Lars Kristensen, Umut A. Yıldız, and Ewine F. van Dishoeck. Detection of the Water Reservoir in a Forming Planetary System. *Science*, 334(6054):338, October 2011. doi: 10.1126/science.1208931.

N. Houk and M. Smith-Moore. *Michigan Catalogue of Two-dimensional Spectral Types for the HD Stars. Volume 4, Declinations -26°.0 to -12°.0.*, volume 4. NASA, 1988.

Jane Huang, Karin I. Öberg, Chunhua Qi, Yuri Aikawa, Sean M. Andrews, Kenji Furuya, Viviana V. Guzmán, Ryan A. Loomis, Ewine F. van Dishoeck, and David J. Wilner. An ALMA survey of DCN/h13cn and dco+h13co+in protoplanetary disks. *The Astrophysical Journal*, 835(2):231, jan 2017. doi: 10.3847/1538-4357/835/2/231. URL https://doi.org/10.3847/1538-4357/835/2/231.

M. G. Hutchinson, A. Evans, H. Winkler, and J. Spencer Jones. Optical-infrared photometry of the "isolated" T Tauri star V4046 Sgr. *A&A*, 234:230, August 1990.

D. Ishihara, T. Onaka, H. Kataza, A. Salama, C. Alfageme, A. Cassatella, N. Cox, P. García-Lario, C. Stephenson, M. Cohen, N. Fujishiro, H. Fujiwara, S. Hasegawa, Y. Ita, W. Kim, H. Matsuhara, H. Murakami, T. G. Müller, T. Nakagawa, Y. Ohyama, S. Oyabu, J. Pyo, I. Sakon, H. Shibai, S. Takita, T. Tanabé, K. Uemizu, M. Ueno, F. Usui, T. Wada, H. Watarai, I. Yamamura, and C. Yamauchi. The AKARI/IRC mid-infrared all-sky survey. *A&A*, 514:A1, May 2010. doi: 10.1051/0004-6361/200913811.

Eric L. N. Jensen and Robert D. Mathieu. Evidence for Cleared Regions in the Disks Around Pre-Main-Sequence Spectroscopic Binaries. *AJ*, 114:301–316, Jul 1997. doi: 10.1086/118475.

Joel H. Kastner, C. Qi, D. A. Dickson-Vandervelde, P. Hily-Blant, T. Forveille, S. Andrews, U. Gorti, K. Öberg, and D. Wilner. A subarcsecond ALMA molecular line imaging survey of the circumbinary, protoplanetary disk orbiting v4046 sgr. *The Astrophysical Journal*, 863(1):106, aug 2018. doi: 10.3847/1538-4357/aacff7. URL https://doi.org/10.3847%2F1538-4357%2Faacff7.

S. J. Kenyon and L. Hartmann. Spectral Energy Distributions of T Tauri Stars: Disk Flaring and Limits on Accretion. *ApJ*, 323:714, December 1987. doi: 10.1086/165866.

N. V. Kharchenko. All-sky compiled catalogue of 2.5 million stars. *Kinematika i Fizika Nebesnykh Tel*, 17(5):409–423, October 2001.

D. W. Koerner, A. I. Sargent, and S. V. W. Beckwith. A Rotating Gaseous Disk around the T Tauri Star GM Aurigae. *Icarus*, 106(1):2–10, November 1993. doi: 10.1006/icar.1993.1154.

Mark R. Krumholz, Christopher F. McKee, and Joss Bland-Hawthorn. Star clusters across cosmic time. *Annual Review of Astronomy and Astrophysics*, 57(1):227–303, 2019. doi: 10.1146/annurev-astro-091918-104430. URL https://doi.org/10.1146/annurev-astro-091918-104430.

R. L. Kurucz. Model atmospheres for G, F, A, B, and O stars. *ApJS*, 40:1–340, May 1979. doi: 10.1086/190589.

Charles J. Lada. Star formation: from OB associations to protostars. In Manuel Peimbert and Jun Jugaku, editors, *Star Forming Regions*, volume 115, page 1, January 1987.

Charles J. Lada and Elizabeth A. Lada. Embedded clusters in molecular clouds. *Annual Review of Astronomy and Astrophysics*, 41(1):57–115, 2003. doi: 10.1146/annurev.astro.41. 011802.094844. URL https://doi.org/10.1146/annurev.astro.41.011802.094844.

V. Lebouteiller, D. J. Barry, C. Goes, G. C. Sloan, H. W. W. Spoon, D. W. Weedman, J. Bernard-Salas, and J. R. Houck. CASSIS: THE CORNELL ATLAS OF SPITZER /IN-FRARED SPECTROGRAPH SOURCES. II. HIGH-RESOLUTION OBSERVATIONS. *The Astrophysical Journal Supplement Series*, 218(2):21, jun 2015. doi: 10.1088/0067-0049/ 218/2/21. URL https://doi.org/10.1088/0067-0049/218/2/21.

A. Li and J. M. Greenberg. A unified model of interstellar dust. *A&A*, 323:566–584, July 1997.

L. B. Lucy. Computing radiative equilibria with Monte Carlo techniques. *A&A*, 344:282–288, April 1999.

S. Marino, S. Perez, and S. Casassus. Shadows Cast by a Warp in the HD 142527 Protoplanetary Disk. *ApJ*, 798(2):L44, January 2015. doi: 10.1088/2041-8205/798/2/L44.

Rafael Martinez-Brunner, Simon Casassus, Sebastián Pérez, Antonio Hales, Philipp Weber, Miguel Cárcamo, Carla Arce-Tord, Lucas Cieza, Antonio Garufi, Sebastián Marino, and Alice Zurlo. High-resolution ALMA observations of V4046 Sgr: a circumbinary disc with a thin ring. *MNRAS*, 510(1):1248–1257, February 2022. doi: 10.1093/mnras/stab3440.

F. Marzari and G. Picogna. Circumstellar disks do erase the effects of stellar flybys on planetary systems. *A&A*, 550:A64, February 2013. doi: 10.1051/0004-6361/201220436.

J. S. Mathis, W. Rumpl, and K. H. Nordsieck. The size distribution of interstellar grains. *ApJ*, 217:425–433, October 1977. doi: 10.1086/155591.

Matthew McJunkin, Kevin France, Eric Schindhelm, Gregory Herczeg, P. Christian Schneider, and Alex Brown. Empirically Estimated Far-UV Extinction Curves for Classical T Tauri Stars. *ApJ*, 828(2):69, September 2016. doi: 10.3847/0004-637X/828/2/69.

G. Meeus, L. B. F. M. Waters, J. Bouwman, M. E. van den Ancker, C. Waelkens, and K. Malfait. ISO spectroscopy of circumstellar dust in 14 Herbig Ae/Be systems: Towards an understanding of dust processing. *A&A*, 365:476–490, January 2001. doi: 10.1051/ 0004-6361:20000144.

Gustav Mie. Beiträge zur Optik trüber Medien, speziell kolloidaler Metallösungen. *Annalen der Physik*, 330(3):377–445, January 1908. doi: 10.1002/andp.19083300302.

N. Miret-Roig, P. A. B. Galli, W. Brandner, H. Bouy, D. Barrado, J. Olivares, T. Antoja, M. Romero-Gómez, F. Figueras, and J. Lillo-Box. Dynamical traceback age of the $\beta$ Pictoris moving group. *A&A*, 642:A179, October 2020. doi: 10.1051/0004-6361/202038765.

Hiroshi Murakami, Hajime Baba, Peter Barthel, David L. Clements, Martin Cohen, Yasuo Doi, Keigo Enya, Elysandra Figueredo, Naofumi Fujishiro, Hideaki Fujiwara, Mikio Fujiwara, Pedro Garcia-Lario, Tomotsugu Goto, Sunao Hasegawa, Yasunori Hibi, Takanori Hirao, Norihisa Hiromoto, Seung Soo Hong, Koji Imai, Miho Ishigaki, Masateru Ishiguro, Daisuke Ishihara, Yoshifusa Ita, Woong-Seob Jeong, Kyung Sook Jeong, Hidehiro Kaneda, Hirokazu Kataza, Mitsunobu Kawada, Toshihide Kawai, Akiko Kawamura, Martin F. Kessler, Do Kester, Tsuneo Kii, Dong Chan Kim, Woojung Kim, Hisato Kobayashi, Bon Chul Koo,

Suk Minn Kwon, Hyung Mok Lee, Rosario Lorente, Sin'itirou Makiuti, Hideo Matsuhara, Toshio Matsumoto, Hiroshi Matsuo, Shuji Matsuura, Thomas G. MÜller, Noriko Murakami, Hirohisa Nagata, Takao Nakagawa, Takahiro Naoi, Masanao Narita, Manabu Noda, Sang Hoon Oh, Akira Ohnishi, Youichi Ohyama, Yoko Okada, Haruyuki Okuda, Sebastian Oliver, Takashi Onaka, Takafumi Ootsubo, Shinki Oyabu, Soojong Pak, Yong-Sun Park, Chris P. Pearson, Michael Rowan-Robinson, Toshinobu Saito, Itsuki Sakon, Alberto Salama, Shinji Sato, Richard S. Savage, Stephen Serjeant, Hiroshi Shibai, Mai Shirahata, Jungjoo Sohn, Toyoaki Suzuki, Toshinobu Takagi, Hidenori Takahashi, Toshihiko TanabÉ, Tsutomu T. Takeuchi, Satoshi Takita, Matthew Thomson, Kazunori Uemizu, Munetaka Ueno, Fumihiko Usui, Eva Verdugo, Takehiko Wada, Lingyu Wang, Toyoki Watabe, Hidenori Watarai, Glenn J. White, Issei Yamamura, Chisato Yamauchi, and Akiko Yasuda. The Infrared Astronomical Mission AKARI*. *PASJ*, 59:S369–S376, October 2007. doi: 10.1093/pasj/59.sp2.S369.

Joan R. Najita and Edwin A. Bergin. Protoplanetary Disk Sizes and Angular Momentum Transport. *ApJ*, 864(2):168, September 2018. doi: 10.3847/1538-4357/aad80c.

F. Ochsenbein, P. Bauer, and J. Marcout. The VizieR database of astronomical catalogues. *A&AS*, 143:23–32, April 2000. doi: 10.1051/aas:2000169.

Eran O. Ofek. Calibrated griz Magnitudes of Tycho Stars: All-Sky Photometric Calibration Using Bright Stars. *PASP*, 120(872):1128, October 2008. doi: 10.1086/592456.

E. Pantin, C. Waelkens, and P. O. Lagage. ADONIS observations of the HD 100546 circumstellar dust disk. *A&A*, 361:L9–L12, September 2000.

Sebastián Pérez, Simon Casassus, Clément Baruteau, Ruobing Dong, Antonio Hales, and Lucas Cieza. Dust Unveils the Formation of a Mini-Neptune Planet in a Protoplanetary Ring. *AJ*, 158(1):15, July 2019. doi: 10.3847/1538-3881/ab1f88.

Sebastián Pérez, Simon Casassus, Antonio Hales, Sebastián Marino, Anthony Cheetham, Alice Zurlo, Lucas Cieza, Ruobing Dong, Felipe Alarcón, Pablo Benítez-Llambay, Ed Fomalont, and Henning Avenhaus. Long Baseline Observations of the HD 100546 Protoplanetary Disk with ALMA. *ApJ*, 889(1):L24, January 2020. doi: 10.3847/2041-8213/ab6b2b.

Chunhua Qi, Karin I. Öberg, Catherine C. Espaillat, Connor E. Robinson, Sean M. Andrews, David J. Wilner, Geoffrey A. Blake, Edwin A. Bergin, and L. Ilsedore Cleeves. Probing CO and $N_2$ Snow Surfaces in Protoplanetary Disks with $N_2H^+$ Emission. *ApJ*, 882(2):160, Sep 2019. doi: 10.3847/1538-4357/ab35d3.

Germano R. Quast, Carlos A. O. Torres, Ramiro de La Reza, Licio da Silva, and Michel Mayor. V4046 Sgr, a key young binary system. *IAU Symposium*, 200:28, January 2000.

Valerie A. Rapson, Joel H. Kastner, Sean M. Andrews, Dean C. Hines, Bruce Macintosh, Max Millar-Blanchaer, and Motohide Tamura. SCATTERED LIGHT FROM DUST IN THE CAVITY OF THE v4046 sgr TRANSITION DISK. *The Astrophysical Journal*, 803 (1):L10, apr 2015. doi: 10.1088/2041-8205/803/1/l10. URL https://doi.org/10.1088%2F 2041-8205%2F803%2F1%2Fl10.

T. Ratzka, R. Köhler, and Ch. Leinert. A multiplicity survey of the $\rho$ Ophiuchi molecular clouds. *A&A*, 437(2):611–626, July 2005. doi: 10.1051/0004-6361:20042107.

W. K. M. Rice, Philip J. Armitage, Kenneth Wood, and G. Lodato. Dust filtration at gap edges: implications for the spectral energy distributions of discs with embedded planets. *MNRAS*, 373(4):1619–1626, December 2006. doi: 10.1111/j.1365-2966.2006.11113.x.

David R. Rodriguez, Joel H. Kastner, David Wilner, and Chunhua Qi. IMAGING THE MOLECULAR DISK ORBITING THE TWIN YOUNG SUNS OF v4046 sgr. *The Astrophysical Journal*, 720(2):1684–1690, aug 2010. doi: 10.1088/0004-637x/720/2/1684. URL https://doi.org/10.1088%2F0004-637x%2F720%2F2%2F1684.

María Paula Ronco, Octavio M. Guilera, Jorge Cuadra, Marcelo M. Miller Bertolami, Nicolás Cuello, Camilo Fontecilla, Pedro Poblete, and Amelia Bayo. Long Live the Disk: Lifetimes of Protoplanetary Disks in Hierarchical Triple-star Systems and a Possible Explanation for HD 98800 B. *ApJ*, 916(2):113, August 2021. doi: 10.3847/1538-4357/ac0438.

Katherine A. Rosenfeld, Sean M. Andrews, David J. Wilner, and H. C. Stempels. A DISK-BASED DYNAMICAL MASS ESTIMATE FOR THE YOUNG BINARY v4046 sgr. *The Astrophysical Journal*, 759(2):119, oct 2012. doi: 10.1088/0004-637x/759/2/119. URL https://doi.org/10.1088%2F0004-637x%2F759%2F2%2F119.

Katherine A. Rosenfeld, Sean M. Andrews, David J. Wilner, J. H. Kastner, and M. K. McClure. THE STRUCTURE OF THE EVOLVED CIRCUMBINARY DISK AROUND v4046 sgr. *The Astrophysical Journal*, 775(2):136, sep 2013. doi: 10.1088/0004-637x/775/2/136. URL https://doi.org/10.1088%2F0004-637x%2F775%2F2%2F136.

Giovanni P. Rosotti, Richard Teague, Cornelis Dullemond, Richard A. Booth, and Cathie J. Clarke. The efficiency of dust trapping in ringed protoplanetary discs. *MNRAS*, 495(1): 173–181, June 2020. doi: 10.1093/mnras/staa1170.

Dary Ruíz-Rodríguez, Joel H. Kastner, Ruobing Dong, David A. Principe, Sean M. Andrews, and David J. Wilner. Constraints on a putative planet sculpting the v4046 sagittarii circumbinary disk. *The Astronomical Journal*, 157(6):237, may 2019. doi: 10.3847/1538-3881/ab1c58. URL https://doi.org/10.3847%2F1538-3881%2Fab1c58.

George B. Rybicki and Alan P. Lightman. *Radiative processes in astrophysics*. John Wiley And Sons Ltd, 1979.

Stolker, T., Dominik, C., Min, M., Garufi, A., Mulders, G. D., and Avenhaus, H. Scattered light mapping of protoplanetary disks. *A&A*, 596:A70, 2016. doi: 10.1051/0004-6361/201629098. URL https://doi.org/10.1051/0004-6361/201629098.

Richard Teague, Jaehan Bae, and Edwin A. Bergin. Meridional flows in the disk around a young star. *Nature*, 574(7778):378–381, October 2019. doi: 10.1038/s41586-019-1642-0.

W. F. Thi, E. F. van Dishoeck, G. A. Blake, G. J. van Zadelhoff, J. Horn, E. E. Becklin, V. Mannings, A. I. Sargent, M. E. van den Ancker, A. Natta, and J. Kessler. $H_2$ and CO Emission from Disks around T Tauri and Herbig Ae Pre-Main-Sequence Stars and from Debris Disks around Young Stars: Warm and Cold Circumstellar Gas. *ApJ*, 561(2): 1074–1094, November 2001. doi: 10.1086/323361.

Harold C. Urey and Harmon Craig. The composition of the stone meteorites and the origin of the meteorites. *Geochimica et Cosmochimica Acta*, 4(1):36–82, 1953. ISSN 0016-7037. doi: https://doi.org/10.1016/0016-7037(53)90064-7. URL https://www.sciencedirect.com/science/article/pii/0016703753900647.

R. van Boekel, M. Min, L. B. F. M. Waters, A. de Koter, C. Dominik, M. E. van den Ancker, and J. Bouwman. A 10 $\mu$m spectroscopic survey of Herbig Ae star disks: Grain growth and crystallization. *A&A*, 437(1):189–208, July 2005. doi: 10.1051/0004-6361:20042339.

van Boekel, R., Waters, L. B. F. M., Dominik, C., Bouwman, J., de Koter, A., Dullemond, C. P., and Paresce, F. Grain growth in the inner regions of herbig ae/be star disks*. *A&A*, 400(3):L21–L24, 2003. doi: 10.1051/0004-6361:20030141. URL https://doi.org/10.1051/0004-6361:20030141.

R. G. van Holstein, J. H. Girard, J. de Boer, F. Snik, J. Milli, D. M. Stam, C. Ginski, D. Mouillet, Z. Wahhaj, H. M. Schmid, C. U. Keller, M. Langlois, K. Dohlen, A. Vigan, A. Pohl, M. Carbillet, D. Fantinel, D. Maurel, A. Origné, C. Petit, J. Ramos, F. Rigal, A. Sevin, A. Boccaletti, H. Le Coroller, C. Dominik, T. Henning, E. Lagadec, F. Ménard, M. Turatto, S. Udry, G. Chauvin, M. Feldt, and J. L. Beuzit. Polarimetric imaging mode of VLT/SPHERE/IRDIS. II. Characterization and correction of instrumental polarization effects. *A&A*, 633:A64, January 2020. doi: 10.1051/0004-6361/201834996.

C. Waelkens, L. B. F. M. Waters, M. S. de Graauw, E. Huygen, K. Malfait, H. Plets, B. Vandenbussche, D. A. Beintema, D. R. Boxhoorn, H. J. Habing, A. M. Heras, D. J. M. Kester, F. Lahuis, P. W. Morris, P. R. Roelfsema, A. Salama, R. Siebenmorgen, N. R. Trams, N. R. van der Bliek, E. A. Valentijn, and P. R. Wesselius. SWS observations of young main-sequence stars with dusty circumstellar disks. *A&A*, 315:L245–L248, November 1996.

Philipp Weber, Pablo Benítez-Llambay, Oliver Gressel, Leonardo Krapp, and Martin E. Pessah. Characterizing the Variable Dust Permeability of Planet-induced Gaps. *ApJ*, 854 (2):153, February 2018. doi: 10.3847/1538-4357/aaab63.

Philipp Weber, Simon Casassus, and Sebastián Pérez. The steady-state hydrodynamics of a long-lived disc: planetary system architecture and prospects of observing a circumplanetary disc shadow in V4046 Sgr. *MNRAS*, 510(2):1612–1626, February 2022. doi: 10.1093/mnras/stab3438.

S. J. Weidenschilling. Aerodynamics of solid bodies in the solar nebula. *Monthly Notices of the Royal Astronomical Society*, 180(2):57–70, 09 1977. ISSN 0035-8711. doi: 10.1093/mnras/180.2.57. URL https://doi.org/10.1093/mnras/180.2.57.

S.J. Weidenschilling. Dust to planetesimals: Settling and coagulation in the solar nebula. *Icarus*, 44(1):172–189, 1980. ISSN 0019-1035. doi: https://doi.org/10.1016/0019-1035(80)90064-0. URL https://www.sciencedirect.com/science/article/pii/0019103580900640.

Jonathan P. Williams and Lucas A. Cieza. Protoplanetary Disks and Their Evolution. *ARA&A*, 49(1):67–117, September 2011. doi: 10.1146/annurev-astro-081710-102548.

Andrew N. Youdin and Yoram Lithwick. Particle stirring in turbulent gas disks: Including orbital oscillations. *Icarus*, 192(2):588–604, December 2007. doi: 10.1016/j.icarus.2007.07.012.

Zhaohuan Zhu, Richard P. Nelson, Ruobing Dong, Catherine Espaillat, and Lee Hartmann. Dust Filtration by Planet-induced Gap Edges: Implications for Transitional Disks. *ApJ*, 755(1):6, August 2012. doi: 10.1088/0004-637X/755/1/6.

B. Zuckerman and Inseok Song. Young stars near the sun. *Annual Review of Astronomy and Astrophysics*, 42(1):685–721, 2004. doi: 10.1146/annurev.astro.42.053102.134111. URL https://doi.org/10.1146/annurev.astro.42.053102.134111.

# Annex A

# V4046 Sgr Annex

## A.1.  Parameter–space exploitation

### A.1.1.  Parameter space partial exploration

As a way to compute a measure of goodness of fit and to try to quantify the model uncertainties, we performed a partial exploration of the parameter space.

We explore $\chi^2$ space in the vicinity of the model values (obtained by trial and error, see Sec. 2.4) for the scale height at $r_\circ$ ($H_\circ$), the width of the gas component of Ring13 $w_{\mathrm{g}13}$, and around the lower limit of the grain sizes in the central blob. The parameter space exploration is shown in Fig. A.1. Our model fits the SED and two images, so the total $\chi^2$ value for a given model is composed of the sum of the $\chi^2$ values for each of the three fits.

$$\chi^2_{\mathrm{total}} = \chi^2_{\mathrm{SED}} + \chi^2_{\mathrm{ALMA}} + \chi^2_{\mathrm{SPHERE}}. \tag{A.1}$$

For $H_\circ$ and $w_{\mathrm{g}13}$, we find that the values of the parameters in our model are at a minimum in each one dimensional $\chi^2$ space, the uncertainties (up and down) will be those that correspond to $\chi^2 = \chi^2_{\mathrm{m}} + 1$, where $\chi^2_{\mathrm{m}}$ is the local minimum value. We approximated the vicinity of the local minimum in these 1D cuts with a quadratic fit.

For the lower grain size limit, we found that despite that our chosen value seems to minimise $\chi^2$, the shape that follows the curve is more suggestive of a border condition. So there is a threshold around $300\,\mu\mathrm{m}$ where the SED starts to deviate strongly from the typical value. That point represents where the NIR excess becomes significantly larger that the observed.
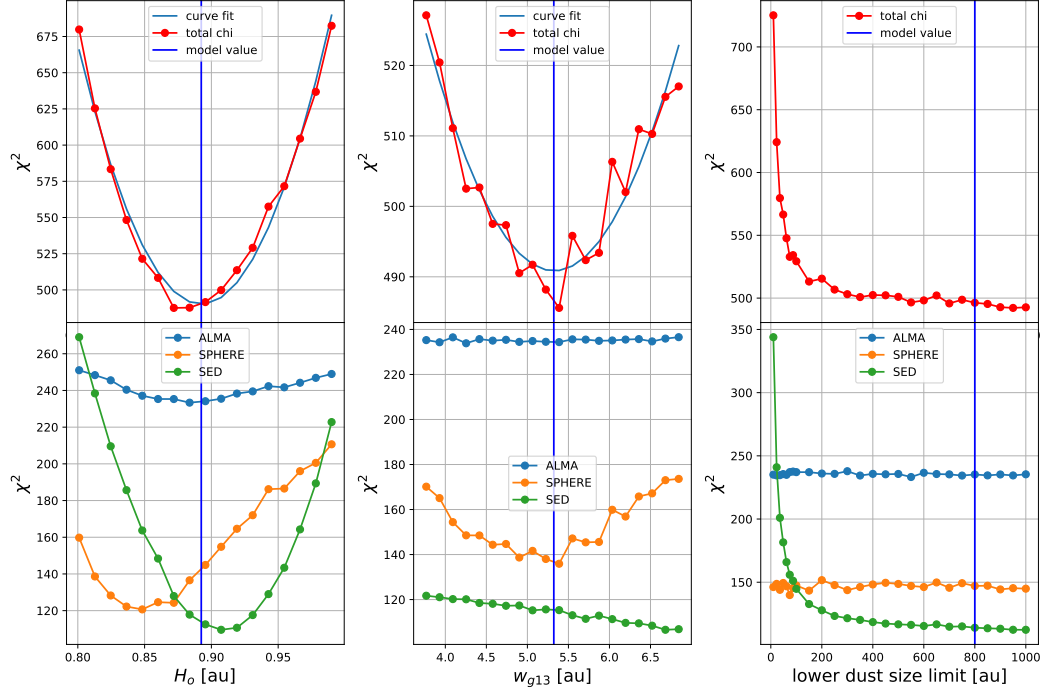
Figure A.1: One dimensional explorations of the chi squared space of our parametric model. The first panel shows the variation of $\chi^2$ in terms of the scale height $H_\circ$ at $r_\circ$=18 au, the second one for the width of the gas component of Ring13 ($w_{\mathrm{g}13}$), and the third one around the lower limit of the grain size in the close inner ring. Each panel displays at the bottom the $\chi^2$ values for the SED and for the two images separately, and on top the total $\chi^2$ value in terms of the parameter value.

## A.1.2. Comparison between different models

A compact inner hole in the dust distribution around a binary can typically be produced by sublimation of solids or dynamical clearing of the central stars. The sublimation radius of the system is expected to be at ~0.05 au ($R_{\mathrm{sub}} = 0.07\sqrt{L_*(L_\odot)}$ au, Francis and van der Marel, 2020), and the edge of the zone cleared by dynamical interactions between the near-circular binary and the circumbinary disc is estimated to be at 0.085 au ($r = 2.08a$, Artymowicz and Lubow, 1994). On the other hand, for V4046 Sgr, Jensen and Mathieu (1997) required to implement a cavity to 0.2 au to fit the SED flux around the silicate feature at 10 μm. We find that the latter value significantly improves the SED fit when compared to a disc extending to the inner radius predicted by dynamical clearing in the SED fit (see Fig. A.2), therefore, the inner radius of the disc in our best-fitting model lies at 0.2 au.

The final structure of our proposed disc also includes additional features that are necessary to fit both the SED and the images. These features are a cut-off of the inner density accumulation of large dust grains outside of 1.1 au (to fit the central emission in the ALMA image), and the thin Gaussian ring made mainly of small dust grains at 5.2 au (Ring5, demanded by

mid-infrared excess in the SED). The first one is visible in the ALMA image so we are forced to include it, but Ring5 is not detected in the ALMA continuum and was included because of its contribution to the 10μm flux is required by the SED. Fig. A.2 works as a summary as it shows a comparison between our best-fitting model and five models with changes on their structures: one without Ring5, one without the inner large-dust disc, one without both of those structures, another with an inner edge of the disc at 0.085 au, and a last one with an inner edge of the disc at 0.05 au. All these models diverge from the SED data somewhere in the 6-300 μm range.
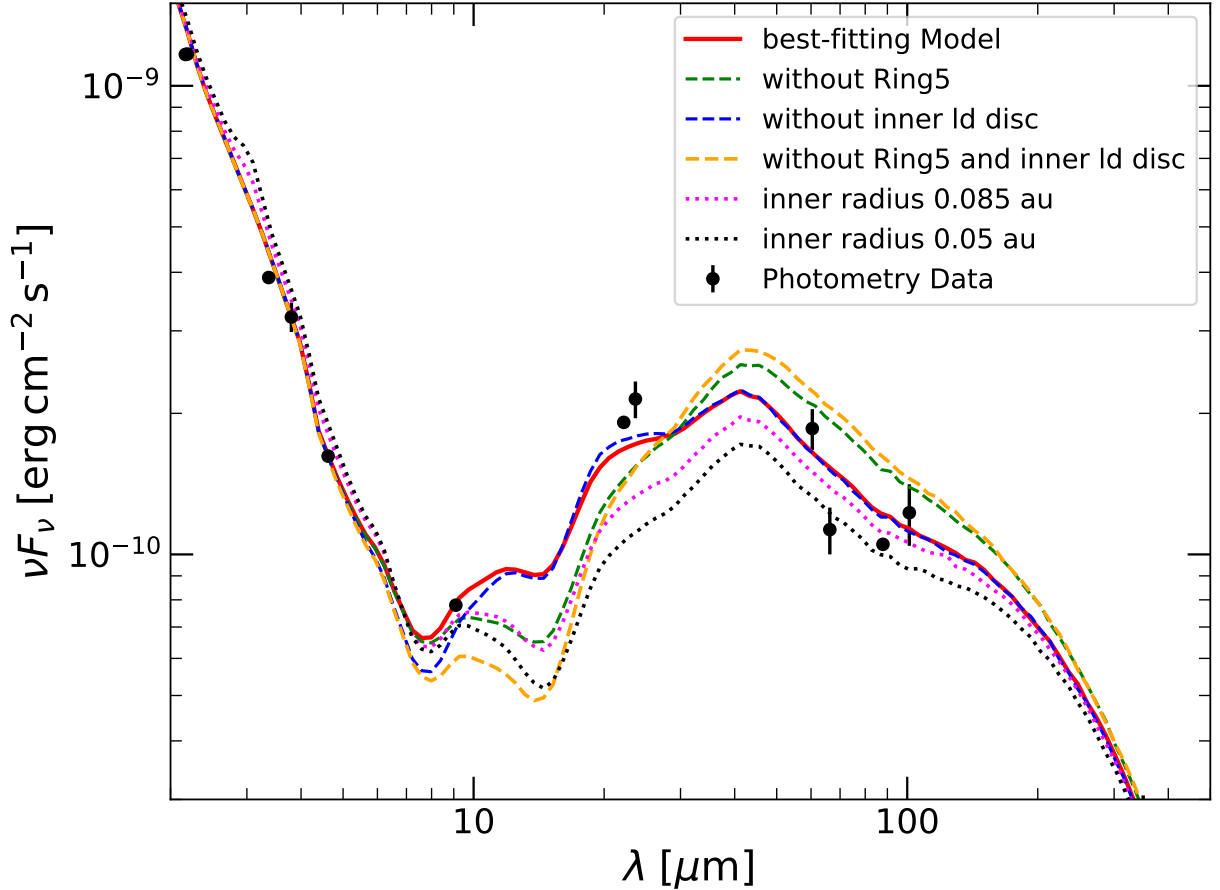


Figure A.2: Comparison between the SEDs of best-fitting model versus five other models with differences in the dust structure. The dotted lines represent the models with different inner radius while the dashed lines represent the models without Ring5 or the inner large-dust disc.